PHASE TRANSITIONS AND VORTEX DYNAMICS IN SUPERCONDUCTING ISLAND ARRAYS

BY

MALCOLM DURKIN

DISSERTATION

Submitted in partial fulfillment of the requirements
for the degree of Doctor of Philosophy in Physics
in the Graduate College of the
University of Illinois at Urbana-Champaign, 2017

Urbana, Illinois

Doctoral Committee:

Professor Alexey Bezryadin, Chair
Professor Nadya Mason, Director of Research
Associate Professor Taylor Hughes
Professor Brian DeMarco

Abstract

In this thesis, we use superconducting island arrays as a platform for studying vortex motion and quantum phase transitions. We investigate superconducting vortex dynamics and lattice structures in superconducting arrays by performing electrical transport measurements on Nb island arrays on Au at milli-kelvin temperatures and finite fields. At low fillings, we observe anomalous vortex dynamics that we attribute to a history dependent dissipative force as the vortex moves through the lattice. At higher fillings, vortex-vortex interaction becomes significant and is dominated by collective vortex motion. We find that the transition from pinned to vortex lattice flow is split into two transitions as the filling is shifted from the commensurate filling regime, where the vortex lattice has strong crystalline order, to an incommensurate filling, where the vortex lattice no longer matches potential wells of the SNS array. We find that this behavior is consistent with domain wall motion in a polycrystalline vortex lattice at commensurate fillings.

Superconducting island arrays can also be used to study phase transitions. Previous work in our group found that the onset of superconductivity in Nb islands was strongly dependent on the island spacing in the array. Performing follow up measurements, we find that the critical island temperature increases as the underlying Au is made thicker, indicating that this effect is dependent on the strength of electrical interactions between islands and is not due to normal metal suppression. Performing measurements on individual islands, we find that the vast majority of 260nm islands undergo a transition at temperatures far lower than those in island arrays, to the extent that they cannot be observed in a Helium 4 cryostat, and that there is a broad distribution of

island critical temperatures observed. This suggests that the onset of superconductivity in rare ordered regions plays a significant role the onset of superconductivity in both the arrays samples and single islands. Lastly, we present work studying the superconductor to insulator transition in Sn island arrays on graphene as well as the technical difficulties involved.

Acknowledgements

Writing the acknowledgement section gives me a chance to reflect on my time at University of Illinois and thank everyone who has helped make my graduate work possible.

First, I would like to thank my advisor, Nadya Mason, for supporting me, giving guidance, project management, and career development opportunities. I would also like to thank her for drastically improving my ability to communicate and present scientific data by having me do so often. I would also like to thank Ian Mondragon-Shem, Professor Taylor Hughes, and Sarang Gopalakrishnan for greatly contributing to this project in theory work. Additionally, I would like to thank our collaborators Tyler Naibert, Greg Polshyn, and Prof. Raffi Budakian for performing atomic force microscopy measurements on niobium island arrays on gold.

Within the Mason Lab group, I would like to give special thanks to Serena Eley for teaching me nanofabrication and cryogenic measurement techniques as well as giving advice on the early work in this project. I would also like to thank her for teaching me how to emotionally deal with the destruction of a chip that I spent 10-15 hours making. I would also like to thank Sungjae Cho for spending hours walking me through my first Helium-3 and Dilution refrigerator runs. Special thanks Stephen Gill for spending long hours helping me repair the Quantum Cluster Evaporator, which much of our research depends on, and for all the coffee. Additionally, thank you to Rita Garrido-Menacho and Vincent Humbert for help with the project and for taking over from me in the future. Also, general thanks within the group to Jeff Damasco, Angela Chen, Yingjie Zhang and Henry Hinnefeld.

I would like to thank my parents and my sister for their support and patience. It has meant a lot to me.

This work would not have been possible without facilities at University of Illinois Frederick Seitz Materials Research Laboratory or funding from the DOE Basic Energy Sciences under DE-SC0012649.

Finally, I would like to thank Professors Alexey Bezryadin, Taylor Hughes, Brian DeMarco, and Nadya Mason for taking the time to read this document and evaluate my defense.

Table of Contents

Chapter 1. Introduction

1.1 Motivation

Superconducting island arrays can serve as highly tunable model 2D systems for studying both classical and quantum phase transitions. In this thesis, we present work on two different island array systems: Nb islands on Au and Sn islands on graphene. The Nb island arrays provide a way of studying superconducting vortex dynamics and the superconductor to metal transition. The Sn arrays on graphene provide a platform for studying the superconductor to insulator transition. Throughout this work, we will examine the effects of disorder on these systems.

The study of vortex matter is motivated by both technical goals and scientific interest. An important technical goal of vortex matter research is the creation of commercially viable superconducting powerlines. Since vortex motion results in dissipation of energy and a non-zero resistance across a sample, reducing vortex creep is important for increasing the critical currents in superconducting powerlines[1]. From a more fundamental perspective, superconducting vortex systems offer a way of studying classical states matter and phase transitions, exhibiting exotic glassy states[2] and offering novel modes of motion[3].

In this thesis, we perform transport measurements on Nb island arrays to study vortex structure and dynamics, controlling array filling with an applied magnetic (*B)* field. The triangular island arrays provide vortices with a periodic potential, resulting in an experimental realization of the 2D Frenkel-Kontorova model [4], which can also be applied to phenomena ranging from charge density waves[5] and to understanding friction [6] in addition to superconducting vortex matter. In chapter 3, we study anomalous vortex motion in the dilute vortex filling limit, providing

evidence for a history dependent dissipative force. In Chapter 4-5, we study vortex structure and motion in a more densely filled array where vortex interactions play a larger role. While the vortex lattice is crystalline when it is commensurate with island array pinning sites, disorder can be introduced by shifting the filling to an incommensurate value. We observe transport behavior consistent with domain wall motion and a polycrystalline rather than glassy state. Lastly, in chapter 6, we investigate whether smoothly varying island density results in a strongly pinned vortex lattice.

Another topic in this thesis is the pursuit of novel phase transitions and states of matter in 2D systems. A key question in both the study of superconductor to metal transitions and superconductor to insulator transitions is whether a zero temperature 2D metallic state is possible. Standard theories indicate that it is not. Due to Anderson localization, the presence of any finite amount of disorder should prevent the quantum diffusion of electrons in 2D system, preventing a $T=0$ 2D metallic state in a non-superconducting system[7]. Moreover, theory suggests a single quantum phase transition between a superconducting and an insulating state in thin disordered superconducting films[8], suggesting the absence of an intermediate state. Nevertheless, a number of works have found evidence for an intermediate metallic state[9], raising questions about the effects disorder and competing states of matter have on a quantum phase transition. In chapter 6, we present work tuning the superconductor to metal transition in Nb islands on Au as well as the onset of superconductivity in granular Nb islands. Chapter 7 presents work performed on superconducting island arrays on graphene with the goal of studying the superconductor to insulator transition.

1.2 Vortex Matter and similar Dynamic Systems

In this section, we provide background information for our study of vortices in SNS arrays, which is covered in chapters 3-6. While the first two subsections provide a summary of previous work in vortex matter and work in SNS, subsection 1.2.3 relates the motion of vortices in SNS to the 2D Frenkel-Kontorova model. At low driving forces, the dynamics of these arrays are determined by the motion of solitons, which can take the form of density wave, domain walls, and even individual defects depending on the state of the system. Examples of several different soliton motion regimes are shown in subsection 1.2.4 and more closely related colloids systems in subsection 1.2.5, which show a transition from what appears to be domain wall motion to quasiperiodic density wave motion. This is relevant to chapter 5, where we characterize the state of an incommensurately filled SNS array and the modes of motion observed, finding that it is polycrystalline and exhibits domain wall motion.

1.2.1 Superconducting Vortices and Vortex Matter

The concept of superconducting vortices formed over several decades. In 1935 Shubnikov discovered type II superconductivity[10], observing that magnetic field penetrated a superconductor above a critical field (H_{c1}), but that the zero resistance superconducting state persisted until a second critical field (H_{c2}). This coexistence of superconductivity and magnetic field penetration (type II superconductor behavior) was surprising, because previously observed type I superconductors expelled all magnetic flux until superconductivity was lost at a critical field (H_c). In 1950, the Ginzburg-Landau equations provided a theoretical framework for interpreting this phenomenon [11]. Under the assumption Shubnikov's regime had both normal and superconducting domains, the energy of the superconductor-normal interface near the critical field

was calculated. The interface energy was found to be determined by a Ginzburg-Landau parameter, $\kappa=\lambda/\xi$, with λ being the London penetration depth and ξ the Ginzburg Landau coherence length[i]. $\kappa<<1$ leads to positive interface energy[ii] and type I superconducting behavior, as the interfaces are energetically unfavorable. $\kappa>>1$ leads to negative interface energy and type II superconducting behavior, as the energetically favorable interface would lead to coexisting superconducting and normal domains. Ginzberg and Landau, however, wrongly assumed that there would be a lamellar ordering of normal and superconducting domains. Abrikosov introduced the concept of a vortex in 1957, finding that normal domains would break apart to maximize the interface size until each contain a quantum of flux[12], $\Phi_0 = h/2e$. This results in the flux passing through the superconductors in tubes consisting of a normal core surrounded by a supercurrent, called vortices. These vortices are mutually repulsive and, due to topology, must enter from the side of the film or be created via vortex-antivortex pair creation.

[i] The length scales that magnetic field and superconducting order change over respectively.

[ii] Near critical field, the presence of magnetic field and the presence of superconducting order are both favorable conditions. Compared to the normal and superconducting regions, the superconductor-normal interface for $\kappa<<1$ has an energetically unfavorable region of size ξ- λ, where B~0 and superconducting order is suppressed. In contrast, the interface for $\kappa>>1$ has an energetically favorable region of size λ - ξ where superconducting order approaches bulk value and a significant field penetrates the array.

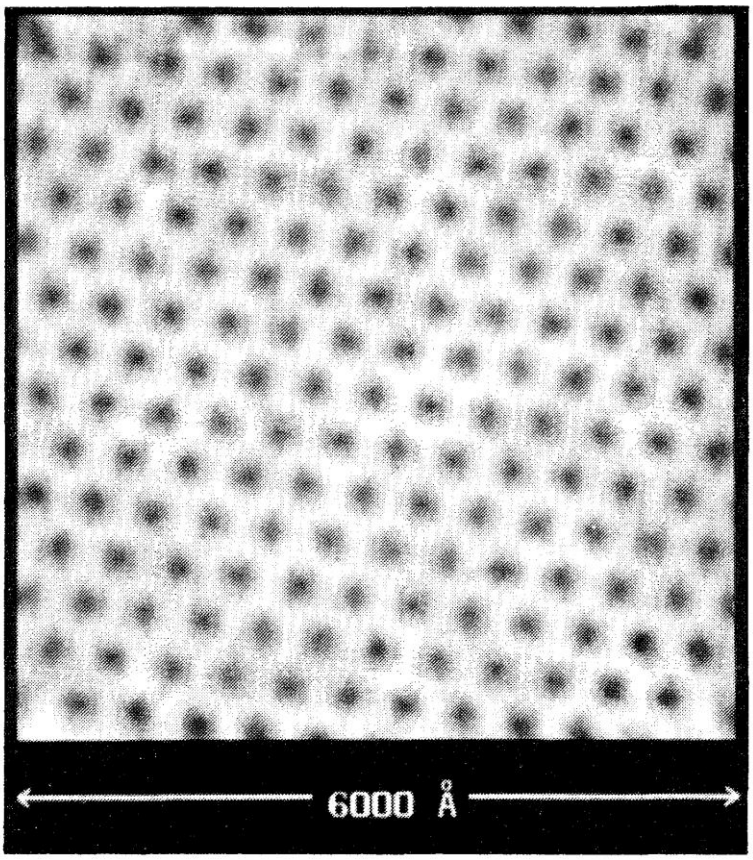

Figure 1.1. Triangular Vortex Lattice imaged by Scanning Tunneling Microscopy (STM). STM measurements on NbSe2 film in a 1T magnetic field. The black dots correspond to vortex normal cores. Taken from [14]

The structures formed by vortices and how these change vortex dynamics is a central topic in chapter 4. In the absence of disorder, mutual repulsion between vortices causes the formation of a crystalline vortex lattices[12,13] as shown in Figure 1.1[14]. The introduction of disorder (e.g. inhomogeneities in the film, which act as energetically favorable resting points) can alter this structure considerably. Generally, disorder manifests itself in the vortex lattice in two ways: interface structures, where disorder takes the form of boundaries separating ordered domains (e.g. polycrystalline structures), and bulk structures, where disorder results in a bulk disordered or quasiperiodic state. These two types of disorder can be seen in studies of disordered superconducting films, where an unexpected peak in vortex de-pinning current was observed as

the temperature approached the critical temperature of the superconductor[15,16,17]. Additionally, the application of currents in these films resulted in enhanced pinning, with a more strongly pinned structure entering the array from the edges[18]. Small angle neutron diffraction experiments have found a quasiperiodic Bragg glass at temperatures below the peak[2] and polycrystalline order at the peak[19], indicating that the weakly pinned structures are Bragg glasses and the strongly pinned structures are polycrystalline. This means that the peak in de-pinning current is due to a transition from a glassy state into a polycrystalline state.

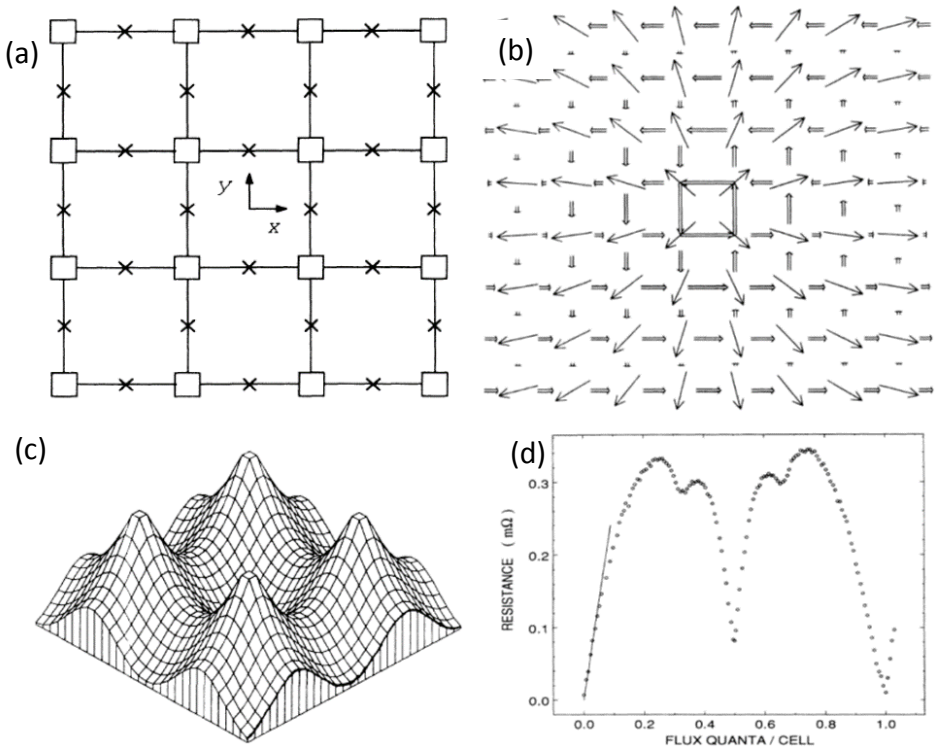

Figure 1.2. Superconductor Normal Superconductor Array. (a) A square SNS array depicted as an array of Josephson Junctions with junctions marked as Xs and nodes marked as squares. (b) Each superconducting node has an order parameter phase shown as a single line arrow. A vortex has all order parameter phase arrows pointing away from the center and is a supercurrent (marked by double line arrows) moves around it. (c) A simulated vortex's energy is plotted as a function of position, showing a periodic potential with energy minimums at the center of the cells and an energy barrier between each well. (d) Resistance vs Field taken in an SNS array. Dips correspond to when the vortex lattice is commensurate with the Energy wells of the array. Taken from [24]

1.2.2 Vortices in SNS arrays

We use a periodic superconductor-normal superconductor (SNS) array to study vortex matter. These SNS arrays take the form of superconducting island arrays on the normal metal. Superconducting islands interact via the superconducting proximity effect, discovered experimentally by Meissner[20,21,22], where superconducting order exists in a normal metal due to proximity with the superconductor-normal interface[23]. Due to the proximity effect, superconducting order can spread across the island arrays and the film, allowing it to be treated as a model superconducting film.

Early work with SNS arrays focused primarily on the static properties of the arrays. The SNS arrays were modeled as Josephson junction arrays with equation

$$E = E_J \sum_{i,j} \left(1 - \cos\left(\phi_i - \phi_j - \frac{2\pi}{\Phi_0} \int_i^j A \cdot dl \right) \right), \quad (1.1)$$

where ϕ_i is the phase of the superconducting order parameter at junction intersection i, E_J is the single junction energy, $\Phi_0 = h/2e$ is the quantum of flux, and A is the vector potential from an externally applied magnetic field. While a resistively and capacitively shunted junction (RCSJ model), elaborated on in chapter 3, would be necessary to simulate the dynamics, this simple Josephson model is valid when the simulating static behavior of a vortex or the arrangement of vortices in an applied field (B). Treating a vortex as a circular arrangement of rotors around a point as shown in Figure1.2(b) with Kirchhoff's circuit laws enforced, Rzchowski, Benz, Tinkham and Lobb were able to calculate the potential of a vortex as a function of position[24]. As shown in Figure 1.2(c), the potential of a non-interacting vortex is periodic in an SNS array with local minima in the center of a square of islands and a barrier in between each island. In the case of a

more densely populated lattice, solving the 2D *XY* model at a finite field using either mean field theory or montecarlo method found that the filling fraction of each plaquette was given by $f=\Phi/\Phi_0$, where Φ is the flux through a unit cell, and that the vortex lattice had crystalline order when the vortex lattice was commensurate with the array pinning sites[25]. Since vortices were strongly pinned, this was visible experimentally in both de-pinning current peaks[26] and in dips in magneto-resistance[25,27], a focus in multiple papers. In contrast to these works, we focus on the dynamic motion of vortices in this thesis.

1.2.3 Frenkel-Kontorova Model

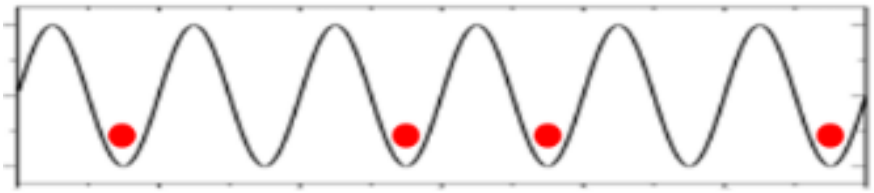

Figure 1.3. 1D Frenkel-Kontorova Model at slightly greater than ½ filling. Particles are shown in red. The periodic potential is shown as a black line. A kink in the lattice is visible in the center as a pair of particles in adjacent wells.

In order to understand the dynamics of a many vortex system, a different treatment is necessary than the ones presented in the previous section. Due to the periodic potential experienced by vortices, the Nb island arrays on Au studied in this thesis are experimental realizations of the 2D overdamped Frenkel-Kontorova model. The Frenkel-Kontorova model[4] is a damped system of mutually repulsive particles in a periodic potential with equations of motion given by

$$m\ddot{x}_i(t) = F_{applied} - F_p \sin\left(\frac{2\pi x_i(t)}{a}\right) - \eta\dot{x}_i(\tau) + \varepsilon_i(t) + \sum_{j=1}^{N} U\left(\frac{x_i(t) - x_j(t)}{L_{int}}\right), \quad (1.2)$$

Where m is mass, $F_{applied}$ is the driving force, F_p is the force from the potential, a is the period of the potential, ε is a stochastic force, and $U(x_i\text{-}x_j)$ is the repulsion between vortices i and j. Vortex

motion can occur by several mechanisms in this system, the most important being uniform lattice motion and soliton motion. Uniform lattice motion occurs when the driving force is sufficient to move the entire lattice. At lower driving forces, vortex motion can still occur via soliton motion[28]. Solitons can take the form of kinks in a soft lattice (shown in figure 1.3) or quasiperiodic density fluctuations in a stiff lattice, where lattice stiffness is determined by the ratio of the force from particle repulsion to that of the periodic potential well. While this type of transport is relevant to a number of systems, the closest studies to ours involve type II superconducting films decorated with artificial pinning center (APC) and colloids trapped in periodic potential wells discussed in sections 1.2.4 and 1.2.5 respectively.

The role of damping, η, on vortex transport should also be mentioned. When discussing particles in a periodic potential, there are two limits that appear frequently: the overdamped case and the underdamped case. The overdamped case, which this thesis uses, has a strong dissipative force and mass that can be treated as zero. This means that a particle's velocity is determined by the net forces on it at any time and momentum does not carry the particle over the periodic potential barrier. The underdamped system has a weak dissipative force and significant mass, meaning that momentum will carry the particle across the periodic array. Underdamped systems have the added complication of being hysteretic and exhibiting

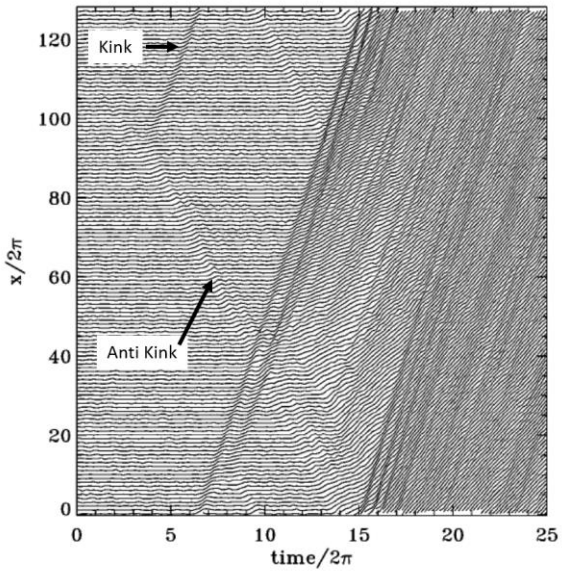

Figure 1.4. Simulated Kink density growth in underdamped 1D Frenkel-Kontorov Model. Each line represents a particle's position as a function of time. Early in the simulation, there is a kink and antikink pair. Due to the bistable behavior of the particles, kink density rapidly grows as time progresses. Taken from [29]

bistable behavior, with a stable pinned state and a stable moving state for a given driving force. This leads to avalanche behavior where moving solitons create other moving solitons, leading to a rapid growth of solitons in the system as shown in the simulation in figure 1.4[29]. While this underdamped case offers an interesting study of nonlinear dynamics, the avalanche behavior washes out most transport signatures of kink motion and appears as a transition from pinned to vortex lattice flow. An experimental study would require rapid imaging of an underdamped particle system. In contrast, the overdamped system lacks this avalanche behavior and will have transport signatures for each particle motion regime.

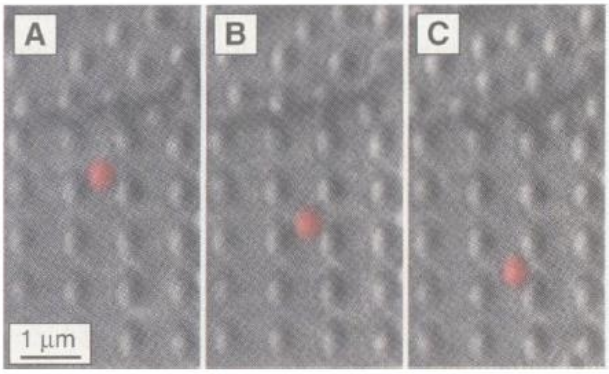

Figure 1.5. Vortex imaging in an APC array on a superconducting film. Magnetic particles are placed on the film and become bunched around vortices, allowing vortices to be imaged. The square vortices are at pinning sites. The vortex marked in red is an interstitial vortex. Taken from [3]

1.2.4 Artificial Pinning Centers on Type II Superconducting films

Experimental research on APC decorated type II superconducting films has demonstrated a rich phase diagram with a variety of vortex transport modes, providing examples of soliton motion including domain wall motion (related to chapter 4). Usually constructed by introducing an ordered array of pinning sites, usually in the form of nanoscale holes in the superconducting film, these arrays are studied in a magnetic field by applying a current and measuring vortex motion as a voltage across the sample. The magnetic field introduces two types of vortices: pinned vortices that are trapped on artificial pinning sites and interstitial vortices that are in the superconducting film as shown in Figure 1.5[3]. Experimental measurements have consistently found a number of vortex transport regimes in this system as shown in Figure 1.6[30,31]. Molecular vortex simulations can explain this as 5 different transport regimes: pinned vortices in region I, 1D interstitial vortex motion in region II, disordered motion in region III, 1D kink motion in region IV, and vortex flow in region V[32]. This is shown in Figure 1.7. In addition to these phases of motion, there may be an additional phase in between Region I and Region II featuring domain wall motion. Simulation at a slight offset from large commensurate values (such as *f=4*) show domain wall motion before the system transitions into interstitial flow [33], as shown in Figure 1.8(a) and (b). This, however, does not have an obvious feature associated with it in the experimental measurements shown in Figure 1.8. Moreover, the system involved is different enough from our periodic 2D potential to discourage direct comparison with our SNS arrays.

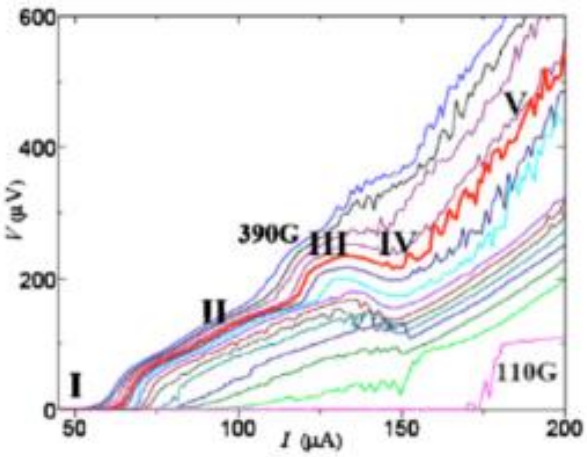

Figure 1.6. I-V Measurements on an APC array taken at incremental B fields. The field ranges from from 110G (*f=1.34*) to 390G (*f=4.75*). The red line was taken at 310G (*f=3.8*), showing several distinct modes of vortex transport [30]

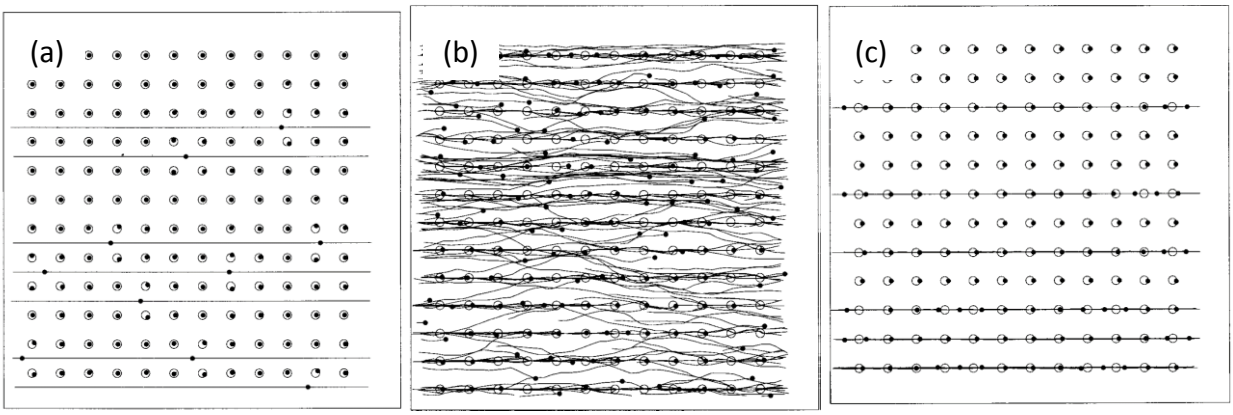

Figure 1.7. Simulated Vortex Motion regimes of APC array. (a) 1D interstitial motion in region II. Interstitial vortices move in a straight line. Pinned vortices remain stationary. (b) Disordered vortex motion in region III. Interstitial vortices push pinned vortices out of pinning sites, resulting in more moving vortices. (c) Linear soliton motion in region IV. Vortices rearrange into lines, with interstitial vortices behaving as kinks facilitating vortex motion. Taken from [32]

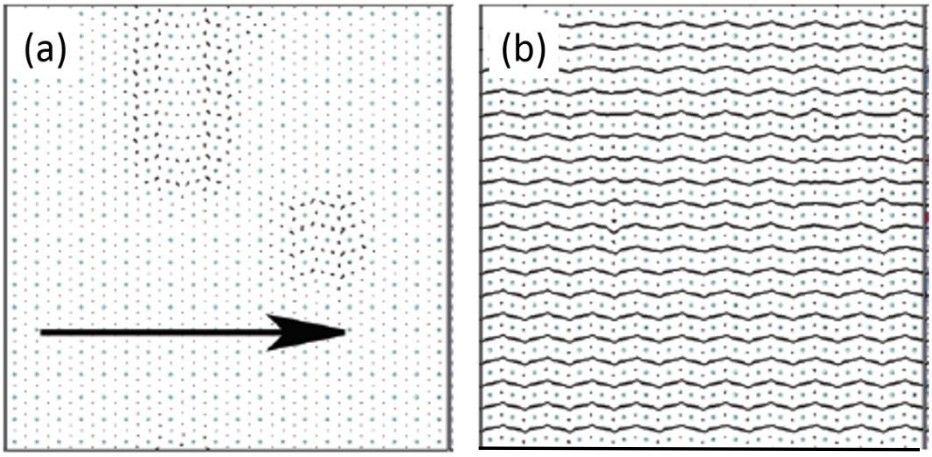

Figure 1.8. Simulated Vortex Motion in artificial pinning center array at f=4.035. (a) Domain Wall Motion at small driving currents. (b) Partial interstitial vortex flow at large driving currents. Taken from [33]

1.2.5 Colloids Trapped in Periodic Potentials

Monolayer colloids in periodic[34] and quasiperiodic[35] potential wells present a system that is theoretically very similar to our SNS arrays, both in equations of motion and the type of potential well. In these studies, negatively charged particles are suspended on water and held in a periodic potential formed by an optical interference pattern. A driving force is then applied by flowing the underlying water layer, driving the particles with a Stokes drag force that is linear with

water layer velocity. Due to mutual repulsion and the presence of a periodic 2D potential, particles in this overdamped system should behave similarly to vortices in our SNS array.

Related to this thesis, the periodic potential study observes the formation of domain walls when the filling is shifted below the commensurate value, as shown in Figure 1.8(c). Above a critical driving force, the domain wall structure breaks down and is replaced by moving compression zones in Figure 1.9(d). Very coarse transport measurements, shown in Figure 1.9(b), show a difference between commensurate and incommensurate states. The commensurate state lacks domain walls and undergoes a visible transition from pinned to compression zone motion (which has a very similar transport signature to uniform flux flow) at $F=70fN$, while the incommensurate filling shows a much broader transition (possibly two) between $F=12fN$ and $F=30fN$. While this type of imaging study demonstrates a transition from domain to quasiperiodic compression zones, the measurements are coarse in both driving force and filling. This makes it difficult experimentally characterize the transport properties or the manner in which domain walls are introduced as the filling is shifted away from commensurate values.

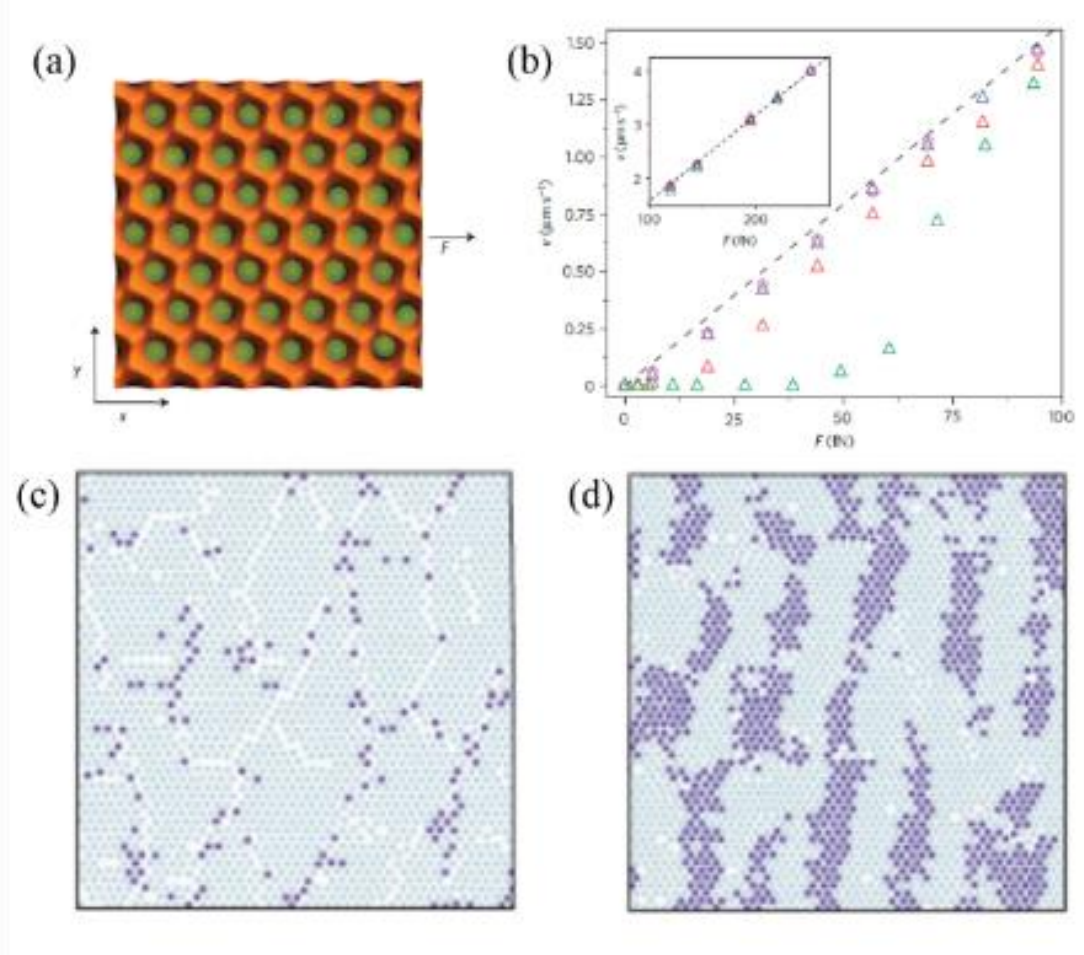

Figure 1.9. Colloid System Structure and dynamics. (a) Colloids shown in green are trapped in a 2D periodic well. (b) Transport measurements showing mean velocity as a function of driving force. The green triangles represent a commensurately filled array with f=1. The red triangles represent an incommensurate filled array with f=0.91. The incommensurate array with f=0.91 at a driving force of (c) 19 fN and (d) 82fN. While (c) retains a polycrystalline structure, (d) breaks into quasiperiodic compression zones. Taken from [34]

1.3 Superconducting Phase Transitions

In this section, we provide background for our study of the superconductor to metal transition in chapter 7 and our work studying the superconductor to insulator transition using superconducting islands on graphene in chapter 8. Much of the work in this section is motivated by the fundamental question of whether a zero temperature 2D metallic state, which is predicted

to be excluded in conventional systems due to Anderson localization[7], is possible. Section 1.3.1 provides an overview of the superconductor to insulator transition. A major issue is that theory predicts that 2D films should transition directly from a superconductor to an insulator as T=0 is approached, despite experimental measurements on inhomogeneous films that are consistent with an intermediate metallic state. Section 1.3.2 discusses the effect on disorder on superconducting films and whether disorder could result in an intermediate metallic state.

1.3.1 Superconductor to insulator transition

The superconductor to insulator transition (SIT) was originally observed in thin superconducting films by altering either thickness[36] or applied magnetic fields[37,38,39], undergoing a transition from a superconducting to an insulating state as shown in Figure 1.10 (a) and Figure 1.10(b), which often occurs when the square film resistance approaches the quantum of resistance, $R_Q=h/4e^2$. This behavior was explained by Fisher as a transition from a superconducting state into a Bose insulator with localized Cooper pairs with a crossover tuned by shunt resistance and capacitance[8]. If the film is viewed as an array of Bose-Hubbard model sites, the commutation relationship between the phase of the order parameter, ϕ, and site filling, N, is equivalent to that between position and momentum. This means large quantum fluctuations in ϕ will result in well defined N and yield an insulating state. A well defined ϕ results in large quantum fluctuations in N and yield a superconducting state. While homogenous films undergo a direct quantum phase transition from a superconducting state into an insulating state, disordered granular systems appear to exhibit an intermediate metallic state[40].

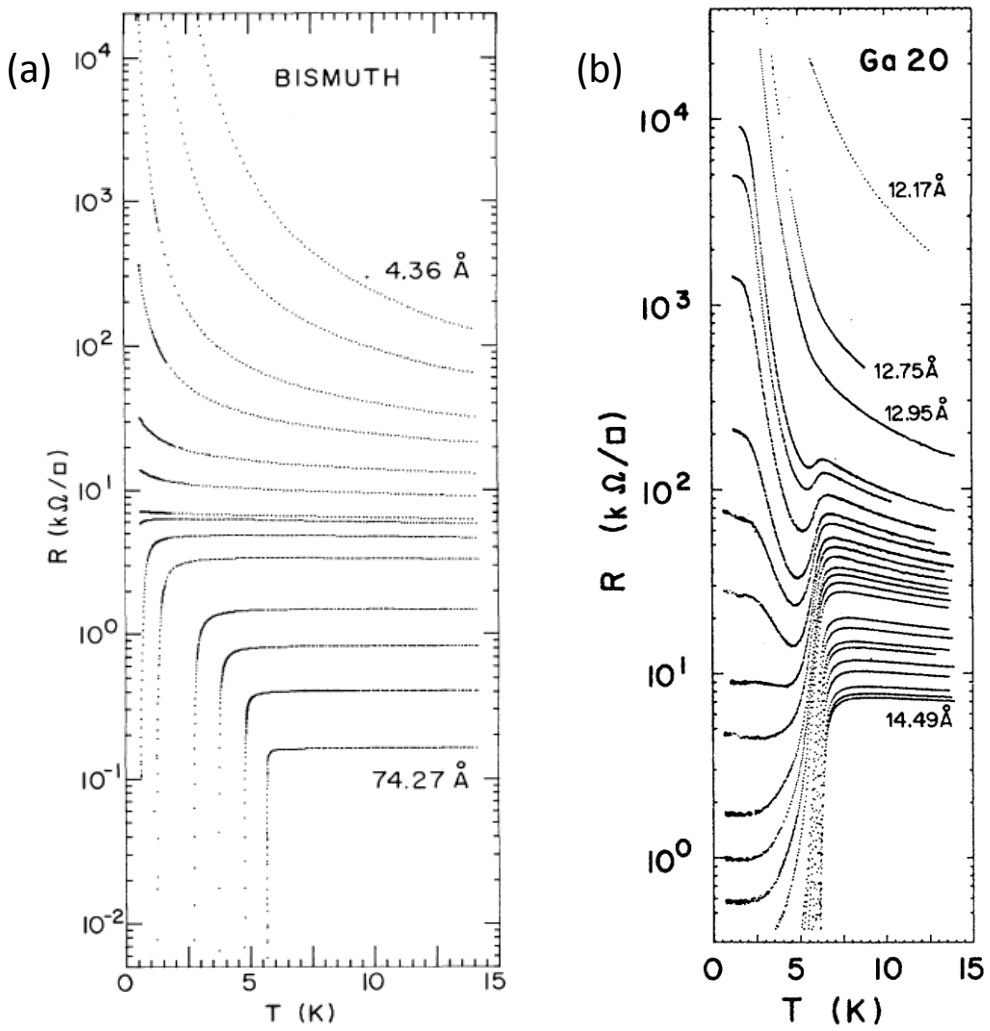

Figure 1.10. Superconductor to insulator transition in thin films (a) Superconductor to insulator transition in Bi shows a direct transition from a superconducting to an insulating state. Taken from [36] (b) Superconductor to insulator transition in Ga appears to have intermediate metallic behavior. Taken from [40]

1.3.2 Effects of Disorder on Quantum Phase Transitions

How disorder alters a quantum phase transition is a key question. Depending on the type of disorder and the type of transition, disorder could dramatically alter a quantum phase transition

or have no effect. In the case of weak disorder, the Harris criterion determines the stability of a critical point against weak disorder[41]. Harris considered a system with a spatial correlation length given by $\xi \sim R^{-\nu}$, where R is the difference in temperature from the critical value ($R=|T-T_c|$). Assuming some spatial variation in T_c, $\delta R(x)$, the variation in the mean R of a correlated region of volume $V_\xi = \xi^d$ (where d is the dimensionality of the system) goes as $\Delta R \sim \xi^{-d/2} \sim R^{-d\nu/2}$ due to mean value theorem. For the clean variation to be preserved, $\Delta R \sim R^{-d\nu/2} < R$ as the system approaches the clean transition point and $R \rightarrow 0$. This Harris criterion is satisfied when $d\nu > 2$, resulting in a transition that is robust against weak disorder. For $d\nu < 2$, Harris criterion is not satisfied and the transition is altered by weak disorder.

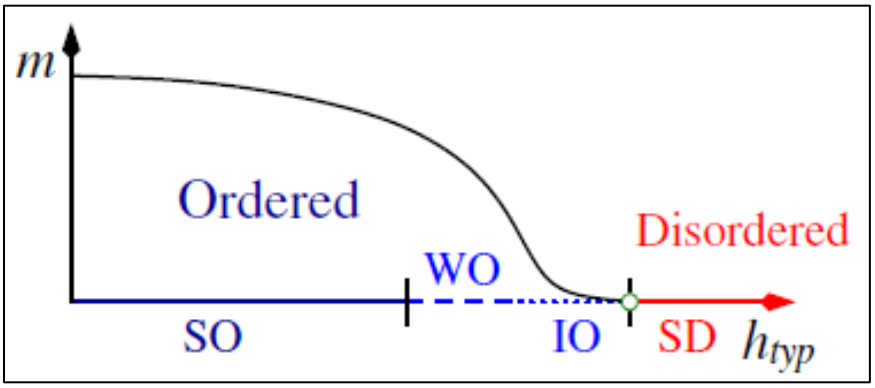

Figure 1.11. Phase diagram of dissipative transverse-field Ising spin Chain. Dissipation stabilizes rare regions so that they can order independently. The result is a transition from strongly ordered (SO) to strongly disordered SD with an intermediate smeared region. [43]

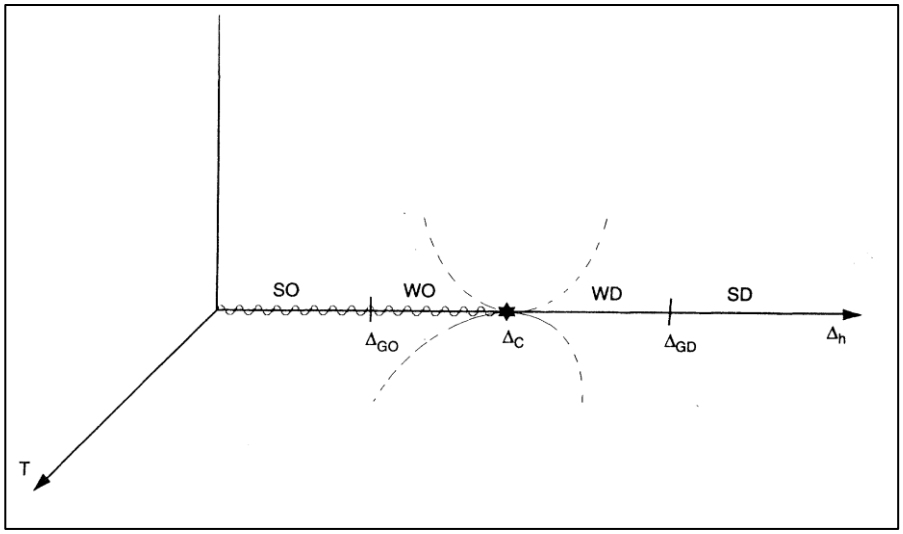

Figure 1.12. Phase diagram of random transverse-field Ising spin Chain. Left to right shows a quantum phase transition from a ferromagnetic ordered phase to a paramagnetic disordered phase at Δ_c. Griffiths points separate strong ordered(SO) and weak ordered (WO) as well as weak disordered (WD) from strong disordered (SD). Taken from [46]

If the system is not robust against disorder, rare region effects can alter the phase transition considerably. The idea for rare region effects came from the randomly diluted 2D Ising model, where each Ising spin site had a probability, *p*, of being removed. While the melting temperature of the Ising lattice decreased as *p* increased due to the vacancies, Griffiths noted that there was a second, higher temperature, melting transition in rare regions that did not have missing Ising spins sites[42]. The effects of rare unusually well-ordered regions on a transition are determined by the dimensions of the rare regions, d_{RR}, and the lower critical dimension of the transition, d_c. If $d_{RR}<d_c$, the rare regions lack the dimensions to be in a different phase than the rest of the system and rare regions effects are weak. For $d_{RR}>d_c$, the rare regions transition independently from the rest of the system and each have their own critical point, smearing the phase transition as shown in Figure 1.11 [43]. In the $d_{RR}=d_c$ case, the rare regions lack static order and undergo quantum fluctuations, resulting in an infinite randomness phase transition with exponential scaling. This behavior was first observed in classical Ising chains[44], but also later in the transverse-field Ising spin chains

[45,46]. Experimentally, rare region effects have been demonstrated in 2D superconducting films in magnetic field, tuning a superconductor to normal metal transition [47].

Rare region effects are of interest in this thesis. In chapter 7, we show that the onset of superconductivity in Nb islands, both individually and in an array, is greatly influenced by unusually well ordered grains that become superconducting at much higher than average temperatures.

Chapter 2. Measurement Setup

This section initially discusses experimental measurement techniques used as well as modifications to cryogenic measurement systems that I have helped to make (with Stephen Gill). The modifications were necessary because electronic noise and improper thermalization can wash out physical phenomenon on samples or result in an impractical signal to noise ratio, preventing usable data. Section 2.3 shows chip mountings and socket holders used in our dilution refrigerator.

2.1 Room Temperature Electronics

Our two basic measurement setups are shown in Figure 2.1. AC and DC signals are produced by an SR830 and a DAQ respectively. These are then processed using analog electronics in a summing amplifier to yield either a current or a voltage. The measured signal is then amplified by a current preamplifier and then read out using the SR830 and DAQ. A good summing amplifier and a good preamp are essential for this, as they provide some common mode rejection and are capable of handling signals far smaller than the SR830 or DAQ. We typically us a model 1211 for a current preamp. Princeton 184 and model 1201 voltage preamps are typically used interchangeably for measurements.

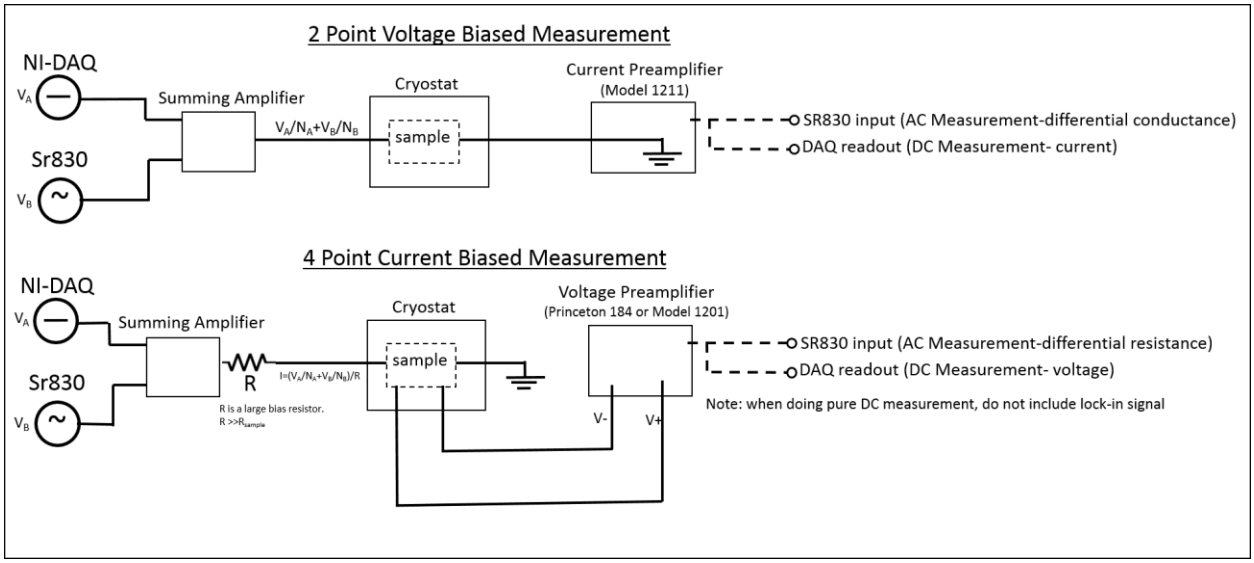

Figure 2.1. Diagram showing basic 2 point and 4 point measurements setups. A summing amplifier and a commercially available preamplifier provide common mode rejection as well as summing, dividing, and amplifying electrical signals.

We use battery powered summing amplifiers sum to sum the two voltage signals, which can also be configured to divide the voltages by as much as 1000. When properly constructed, the summing amplifiers can output stable voltages of around 5μV with a noise of approximately10nA. As shown in Figure 1a, the outside of the input BNC connectors is not sunk to the outside of the sum box like that of the output connectors. Instead, a buffer integrated chip (IC) (AD622 in Figure 2.2) takes the difference between the inner pin and the outer shield of the input BNC and sends this voltage into an inverted summing amplifier, whose diagram and basic properties are detailed in Figure 1b. The buffer chip is used for common mode rejection, eliminating many grounding issues. For a summing amplifier, the OP177 was chosen because it is a stable low noise op amp and the capacitor (which is optional) serves as a low pass filter. It is very important not to use carbon resistors, notorious for generating large amount of thermal noise, for measurement related electronics. Instead, use metal film or foil resistor with low noise specifications.

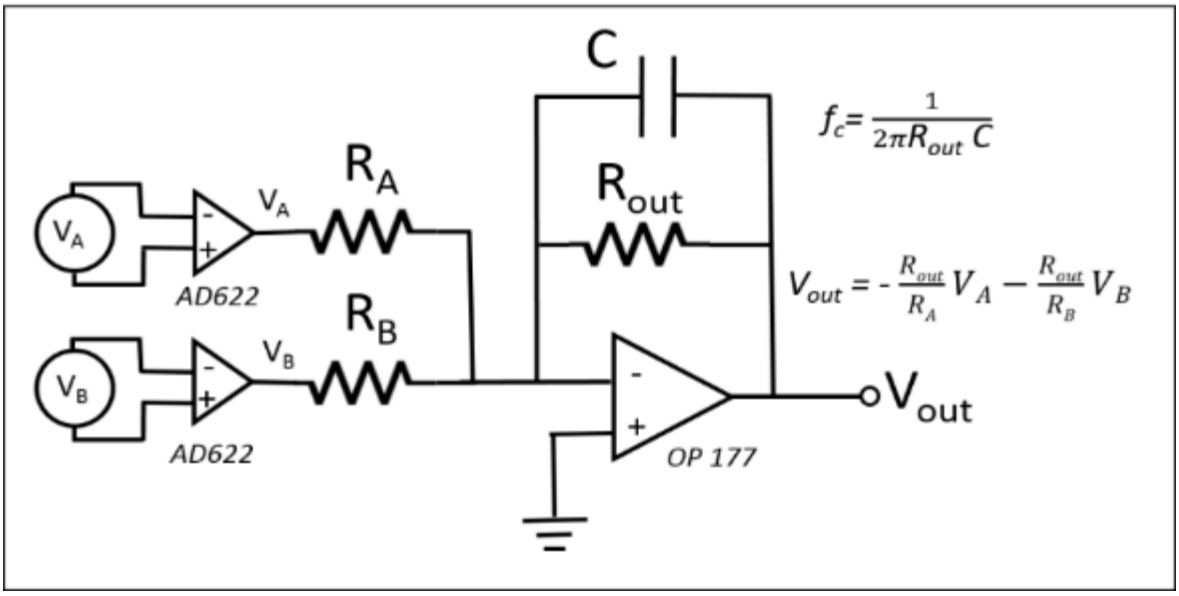

Figure 2.2. Circuit diagram of the summing amplifier. Relevant parameters shown. f_c between *2 KHz* and *15KHz* is desirable if capacitor is included. The ground is linked to the outside of the box and the exterior of the output BNC.

Applying a stable gate voltage has been a consistent problem in our group. This is partly due to the limitations of our silicon oxide gates, but also due to the use of a Keithley 2400 at voltages greater than 30V, often without filtering. The Keithley 2400 requires a sizeable RC low pass filter (~10Hz) in order to be viable as a gate controller, which filters out most of this noise. An alternative might to be to make a 10 times amplifier for the DAQ, but this has not been tested.

2.2 Cryostat Electronics

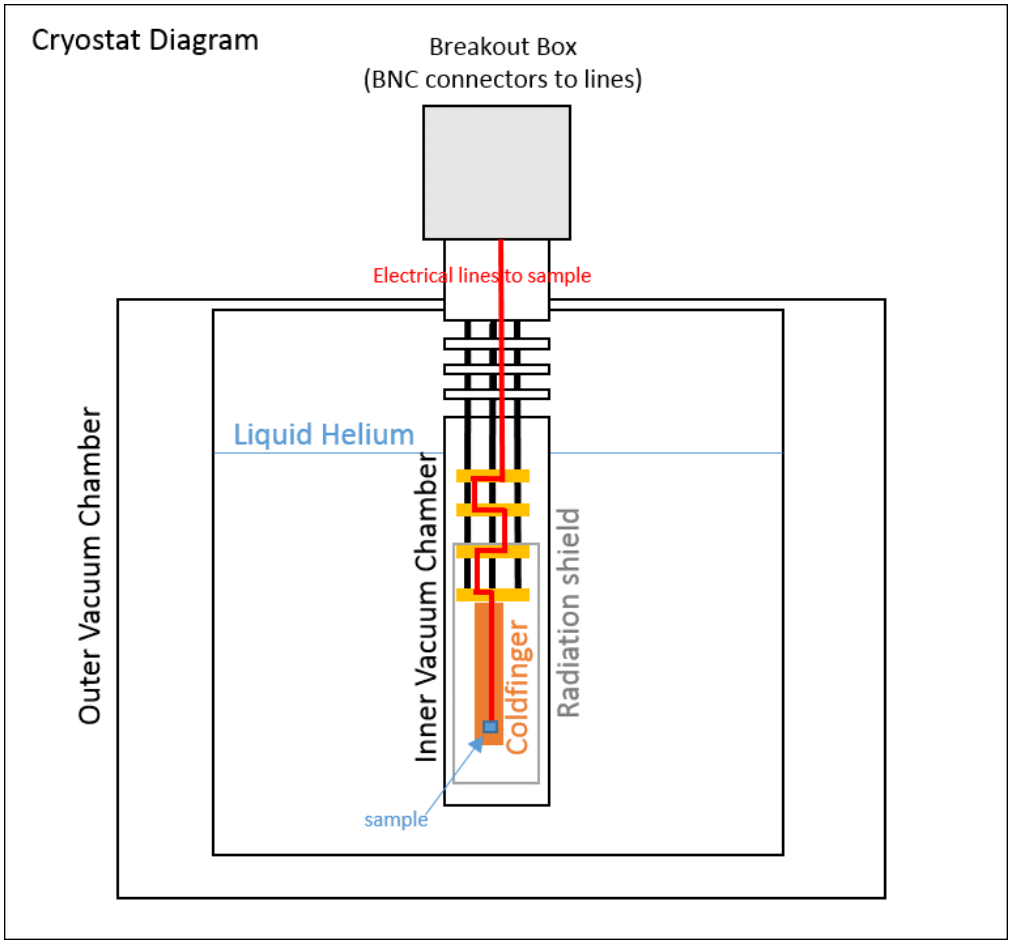

Figure 2.3. Diagram Showing the layout of a dilution refrigerator. We connect to BNC connectors on the breakout box at the top, which are linked to electrical lines that go all the way down to the sample at the bottom. The yellow boxes represent plates of different temperatures (lower plates have lower temperatures) , with the lowest being the base plate at around 20mK. While some attempt has been made to thermalize these lines on each plate, this becomes difficult with the colder plates and the wiring that comes with these fridges is notorious for not being properly thermalized. Some groups replace this wiring and thermalize on each stage, but we rely on extensive filtering and thermalization on our coldfinger. The only other section modified is the breakout box at the top.

While commercially made cryogenics systems are commonly used among research groups, these often require the addition of extensive filtering and line thermalization to perform optimally. On our Oxford systems, we use room temperature pi filters to filter high frequency (>10MHz) noise from our lines prior to entering the cryostat. The rest of the filtering is performed on the cold finger on the mixing plate of the cryostat.

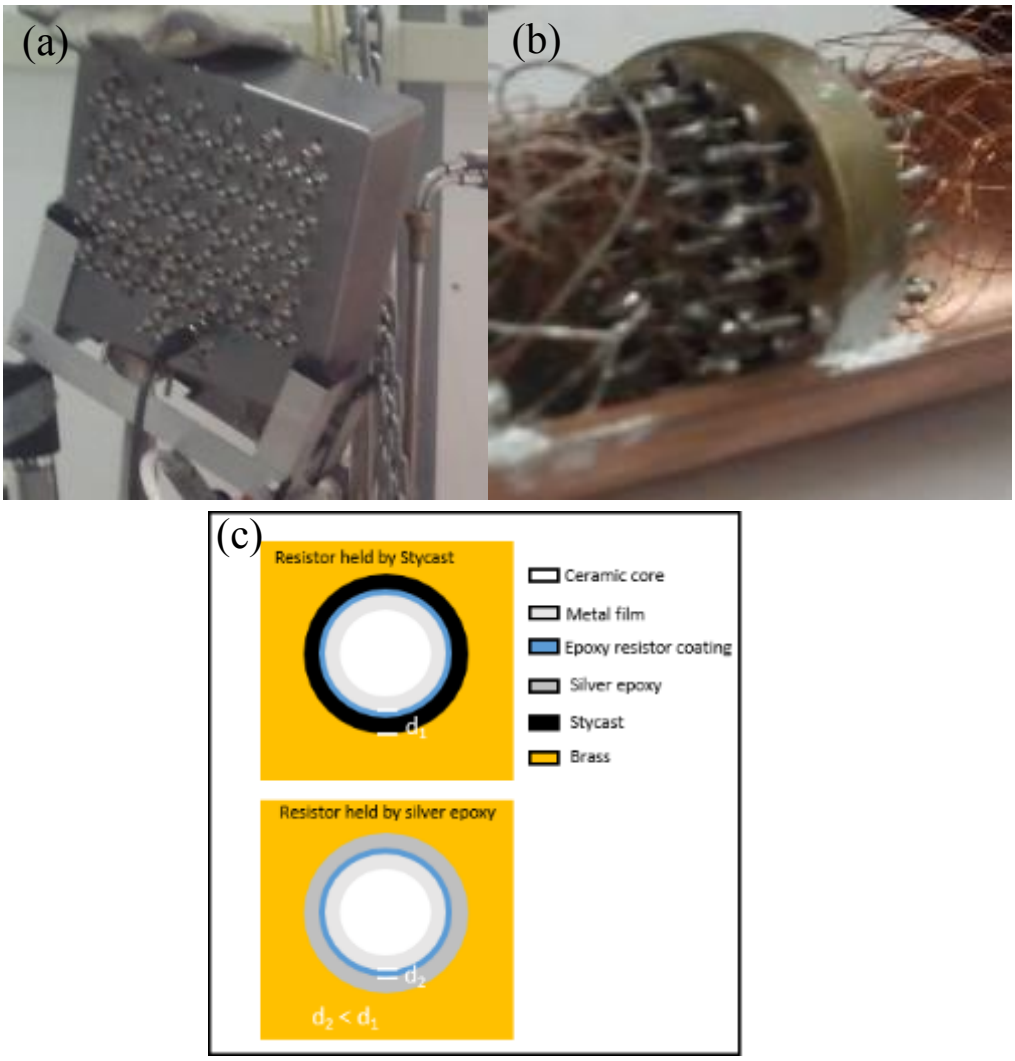

Figure 2.4. (a) **Breakout box at the top of cryostat.** Contains room temperature pi filters for filtering high frequencies. Box also serves as a common ground for instruments directly connected with BNC cables. (b) **Cold resistors on the cold finger** While initial versions used stycast, later versions like the one pictured use silver epoxy to hold the resistor in place. (c) Cross section of mounted cold resistors. Resistors held in place with silver epoxy have greater capacitance and are better thermally coupled to the brass plate than those using stycast.

The first generation of cold finger that I made used thermally sunk metal film resistors (1kΩ-3kΩ), which were held in close fitting brass blocks using stycast as shown in Figure 2.4 (b). This type of filtering adds line resistance to avoid grounding issues and provides surface area for thermalization. Additionally, as shown in Figure 2.4 (c), the metal film resistor consists of a metal film around a ceramic core and forms a parallel plate capacitor. This creates a compact low pass

RC filter. While this is suitable for some cryogenic applications, the frequency cutoff of these filters was greater than 50kHz and the sample's electron temperatures were 150-200mK. This was because Stycast is a poor thermal conductor and an electrical insulator, resulting in poor thermal and capacitive coupling between the resistor film and the metal block.

The second generation cold finger used silver epoxy in place of stycast. This is both thermally and electrically conductive, meaning that the resistor's thin layer of epoxy is the primary thermal barrier to the resistor and serves as a dielectric between a capacitor formed by the metal film and the silver epoxy (much closer parallel plates than with stycast separation). Using a 1 kΩ resistor, we were able to make a well thermalized RC low pass filter with a 5kHz cutoff. Since RC filters become less effective at high frequencies, we layered the line with Eccosorb, a commercially available epoxy that absorbs frequencies above 800MHz. A comparison between the previous filter setup and this configuration in a He3 fridge resulted in a factor of 2 improvement in signal to noise ratios on superconducting island samples.

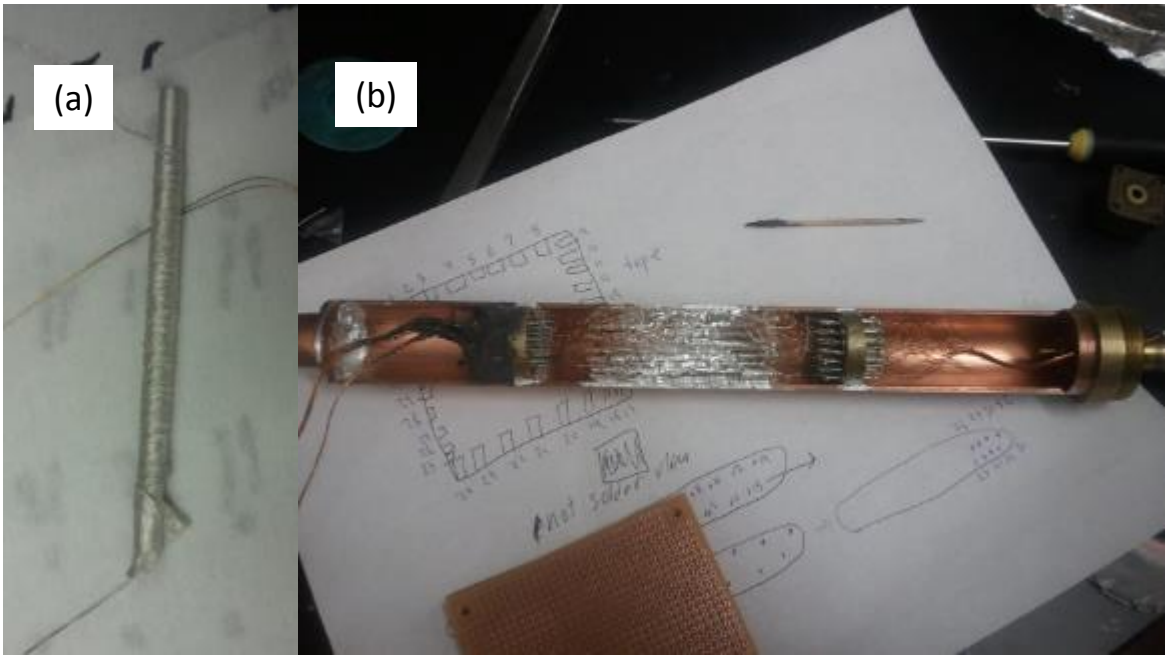

Figure 2.5. (a) A silver epoxy filter made by wrapping a twisted pair wire covered in silver epoxy around a copper rod. Only half of the silver epoxy filters made were could be used, the rest had at least one short to the epoxy. (b) The full filtering layout of a cold finger using silver epoxy filters. From left to right: eccosorb filtering, 1KΩ resistor block, silver epoxy filter, and a 100Ω resistor block.

The third generation of cold finger we made included a silver epoxy filter in between 1 kΩ and 100Ω metal film resistors silver epoxied into a brass block. These filters consist of 1.5 meter long twisted pair wires covered in silver epoxy and wrapped around a copper rod. This provides additional thermalization for the lines, inductance to attenuate high frequency signals, and a skin effect similar to that found in copper powder filters. Similar filters have been benchmarked and have been found to have a cutoff frequency in the 100MHz range[48] and have been able to reduce sample temperature to around 20 mK. This is consistent with measurements of quantized conductance steps and a supercurrent in InSb nanowires by Stephen Gill, which indicate an electron temperature of under 50 mK.

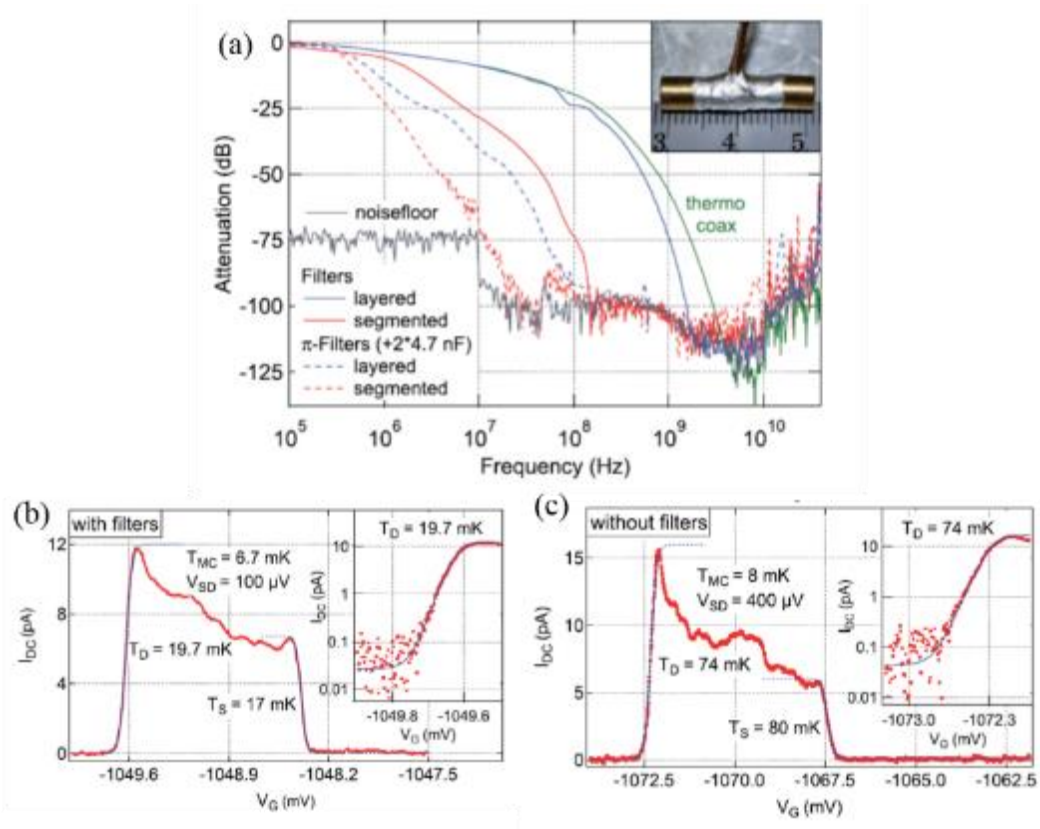

Figure 2.6. Silver epoxy filter benchmarks. (a) Attenuation vs frequency. Layered wires are wrapped together. Segmented are wrapped individually. Our silver epoxy filters are similar to the segmented filters (solid red line). (b) Temperature measurement made by measuring thermally excited tunneling through a quantum dot. With filters, the sample is approximately 20mK.(c) Without filters, the sample is at 80mK. Figure taken from [48]

Lastly, we painted the interiors of our radiation shields and cold finger cans with black paint. This is common serves to absorb stray infrared radiation. It is uncertain if this has any effect on any devices in our group, but it is low cost and can be implemented quickly.

2.3 Chip Holder

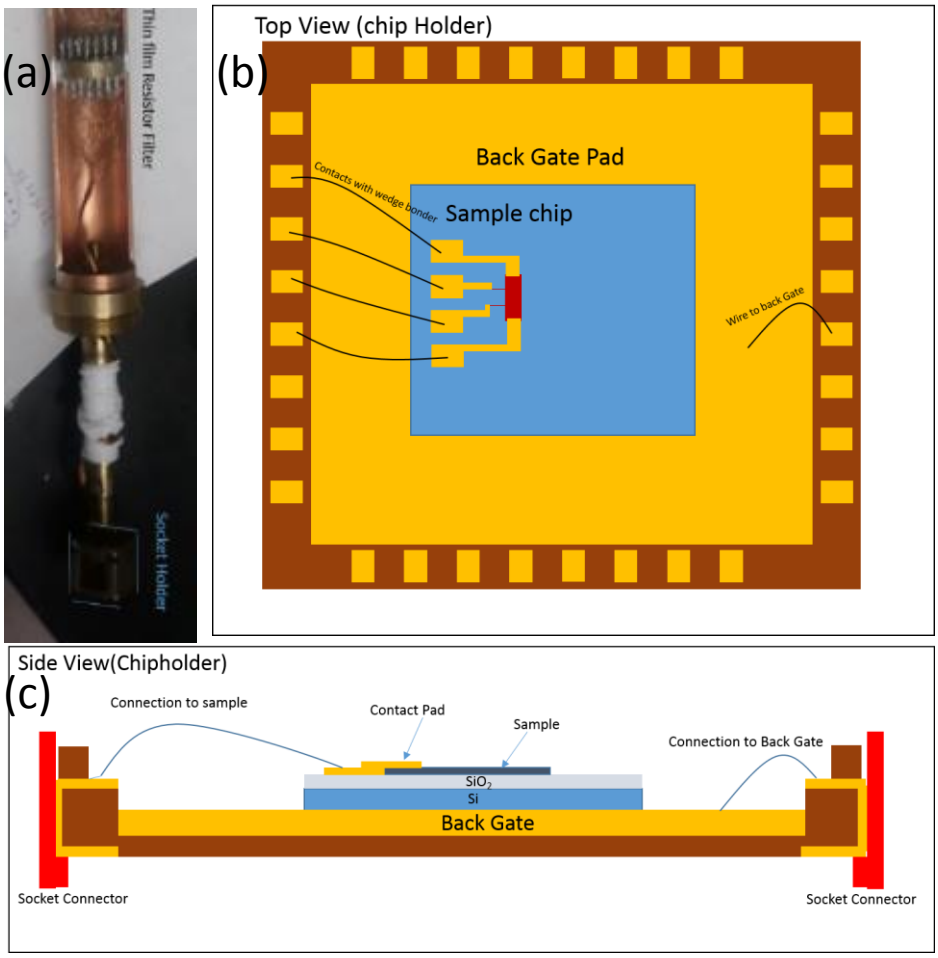

Figure 2.7. Coldfinger and Socket (a) Lower Segment of Coldfinger, including socket holder. When fully prepared, this should be surrounded by another shielding can. (b) Top view of the chip holder. There are 32 pins that connect to the cold finger, corresponding to the 32 BNC connectors at the top. These are connected to the sample via a wedge bonder. A 4 point measurement with a back gate is shown wired. (c) Side view of the chipholder with connections to the socket shown.

A sample is connected to the cold finger wiring via a sample holder socket shown in Figure 2.7 (a). The sample is silver painted to the sample holder and then the contact pads are wedge bonded to the sample holder pins as shown in Figure 2.7 (b) and (c). If a back gate is needed, a bond is placed on the Au back pad in order to use the 300nm SiO_2 layer as a dielectric. This method allows for very fast sample turn around in the measurement system.

Chapter 3. Vortex Dynamics Dilute Non-Interacting Regime

In this chapter, we focus on vortex motion in the dilute vortex filling regime where interactions are negligible. Performing current(I)-voltage(V) measurements on low resistance superconductor-normal-superconductor(SNS) arrays in finite fields, We observe significant deviations from predicted behavior, notably the absence of a differential resistance peak near the vortex de-pinning current and a broad linear *I-V* region with an extrapolated *I* intercept equal to the de-pinning current. Comparing these results to an overdamped molecular vortex model, we find that this behavior can be explained by the presence of a history dependent dissipative force. This points to more a more complicated non-equilibrium effect that is altering our dissipative term. This section is adapted from a previously published work[49].

3.1 Predicted Vortex Dynamics

SNS arrays can be modeled using either a resistor-capacitor-superconductor junction (RCSJ) array model[50,51] or a molecular vortex model[52,53], which exhibit surprisingly similar behavior. While a static treatment of an SNS array is discussed in section 1.2.2, the dynamic treatment of the system is given here. The equations of motion for a superconducting island in an RCSJ array are given by

$$I_i = \sum_j \left(\left(\frac{\Phi_0 C}{2\pi} \right) \ddot{\gamma}_{ij} + \left(\frac{\Phi_0}{2\pi R_N} \right) \dot{\gamma}_{ij} + I_c \sin(\gamma_{ij}) \right), \quad (3.1)$$

where C is the capacitance, R_N is the normal resistance of the junction, I_i is the externally applied current ($I_i = 0$ for most islands. $I_i = I$ and $I_i = -I$ on islands touching the source and drain current leads respectively, where I is the applied current), $\Phi_0 = h/2e$ is the quantum of flux, i and j are the

indices of adjacent islands, and $\gamma_{ij} = \phi_i - \phi_j - \frac{2\pi}{\Phi_0}\int_i^j A \cdot dl$ where ϕ_i is the order parameter phase of island *i* and. An RCSJ array can exhibit two types of motion at low fields: a vortex motion regime above a vortex depinning current, I_d, where only vortices move and a bulk order parameter phase motion regime above I_c where all phases are driven. As discussed in section 1.2.2, a vortex is a topological defect around which a 2π phase rotation. Vortices populate the arrays at finite magnetic fields, are affected by a periodic potential[54], and experience a driving force from an applied current with a de-pinning current that is much lower than the junction critical current ($I_d << I_c$). Array simulations[50,51] indicate that the vortex motion mode follows similar dynamics to the single junction case described by Ambegoar-Halperin[55]. This similar dynamic behavior is because the vortex moves through a periodic potential and has mass and damping terms determined by the junctions in the array.

Due to this equivalent dynamic behavior, vortex motion in SNS arrays can be modeled using a molecular vortex model. In the dilute, non-interacting regime, this takes the form of`

$$m\ddot{x}_i(t) = -\frac{\partial V(x_i(t))}{\partial x_i} - \eta\dot{x}_i(\tau) + \epsilon_i(t), \quad (3.2)$$

where there is a mass term given by $M = \left(\frac{\hbar C}{4e}\right)$ and a dissipative term given by $\eta = \left(\frac{\hbar}{2e}\right)\frac{1}{2R_N}$. The potential $V(x_i(t))$ takes the form

$$V(x) = V_p \cos\left(2\pi\frac{x}{a}\right) - J\Phi_0 x, \quad (3.3)$$

where *a* is the periodicity of the potential, V_p is the potential barrier height, *J* is the applied current density, and Φ_0 is the quantum of flux. While having similar results to the rotor model, molecular

vortex models are often more easily interpreted as vortex locations do not have to be extracted from rotor positions.

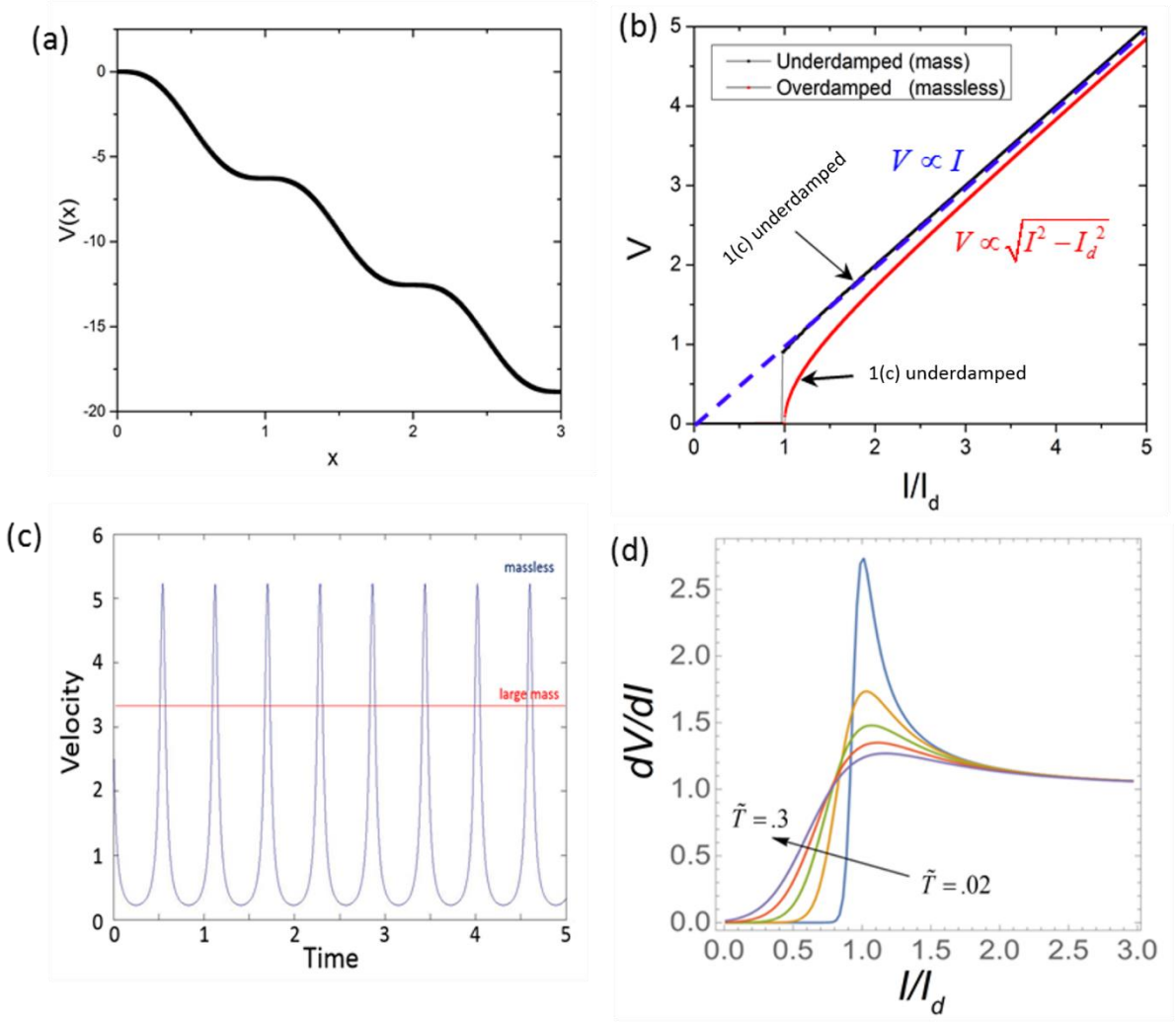

Figure 3.1. Dynamics of a particle in a tilted washboard potential. (a) A periodic potential is tilted by a Lorenz force from an applied current. (b) The predicted *I-V* behavior of overdamped and underdamped vortex systems, shown in red and black respectively. (c) The velocity versus time of an overdamped (dark blue) and underdamped (red line). (d) The expected temperature dependence of *dV/dI* resulting from vortex motion in an overdamped array in the low filling limit. Note that there is a differential resistance peak that persists even at large temperatures.

There are two different dynamic regimes to this model: the overdamped regime (low resistance arrays with $\eta >> m$) and the underdamped regime (high normal resistance arrays with $m >> \eta$). The underdamped case is hysteretic when current is swept up and down, exhibiting a bi-

stable regime where there is a stable vortex motion mode and a stable regime pinned mode. The behavior of an underdamped array when swept upwards is shown in Figure 3.1(b) in black, making a sharp transition from pinned to flux flow where $\dot{x}_i = \eta / \mathrm{J}\Phi_0$. This is because, once vortices start moving, the large mass will keep the velocity roughly constant as shown in Figure 3.1 (c) and the periodic potential is ignored.

Vortices in an overdamped arrays can be treated as massless particles, setting *m=0*. This system undergoes a transition from a pinned state into a vortex flow state at the depinning current, I_d. Unlike the underdamped case, vortex motion does not immediately approach terminal velocity behavior after the de-pinning transition. Instead, vortices get caught on the flat areas of the tilted washboard and undergo significant velocity oscillations over time as shown in Figure 3.1(c), indicating that the periodic potential still plays an important effect in vortex motion. As shown in Figure 3.1(b), the I-V relationship takes the analytic form

$$V \propto N\sqrt{I^2 - {I_d}^2}\,, \quad (3.4)$$

which is nearly identical to that of the overdamped single junction array, only replacing the critical current with the de-pinning current and having a linear relation to the number of vortices, *N*. Both the overdamped and underdamped systems should converge to $V \propto I$ behavior at high currents. The transition from pinned behavior to this linear behavior necessitates a differential resistance peak near I_d that is robust against temperature, as shown for the overdamped case in Figure 3.1(d).

3.2 Measured Vortex Dynamics

For reasons that have not been well understood, the majority of experimental measurements on SNS arrays do not match the above models[24,26]. While experimental measurements do find

predicted features like a constant flux flow resistance at large currents that is proportional to lattice filling (magnetic field), essential features like a differential resistance peak is strikingly absent. To address this, we perform a study of vortex dynamics in the dilute filling regime, where vortex-vortex interactions should be minimal.

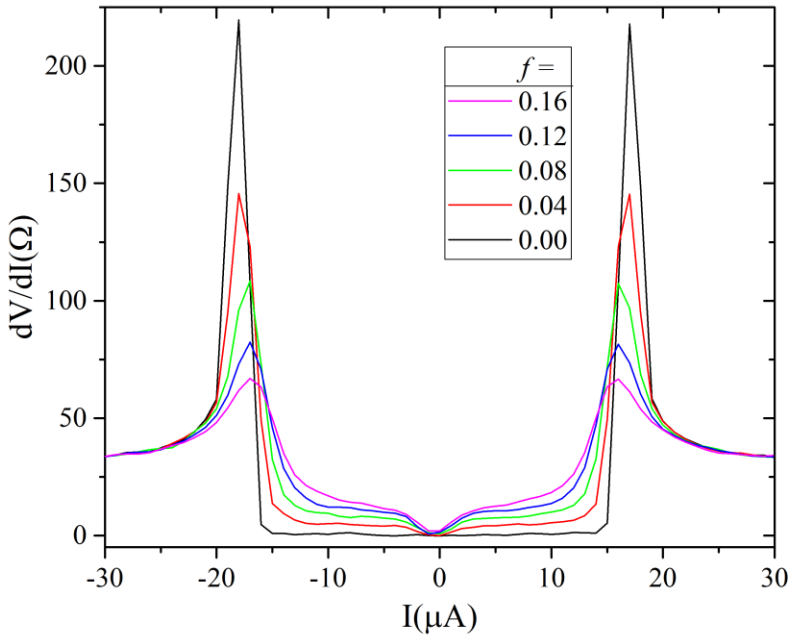

Figure 3.2. *I-V* Measurements of 390nm Spaced Islands with both de-pinning current and junction critical current visible. Measurements were taken at 17mK and 5 millisecond pulsed *I-V* measurements were used to minimize joule heating. Below the array critical current, I_c=16μA, the electrical properties are dominated by vortex motion.

In order to study the dynamic vortex behavior in the arrays, we took DC current-voltage (*I-V*) measurements, focusing on the dilute vortex population regime below *f=1/10* (less than one in ten triangular island plaquettes filled). The applied current provides a Lorentz force and the vortex motion can be measured as a voltage across the arrays. The measurements are performed on triangular island arrays with 390 nm edge-to-edge spacing with Nb island diameter of 260nm unless otherwise stated. The Au film is 10 nm thick and the Nb islands are 70nm thick.

Figure 3.2 shows dV/dI vs I extracted from pulsed I-V measurement, with 5 millisecond current pulses to minimize joule heating. Here, the junction critical current is I_c =15 μA and electrical transport below 15 μA is dominated by vortex motion, with dV/dI proportional to f. Since Joule heating is often an issue in mesoscopic samples, we compared both pulsed I-V measurements and continuous I-V to see if the difference in average power resulted in heating, finding that there was no significant difference at currents below 10μA. Additionally, we performed I-V measurements at varying temperatures, finding a zero B field transition temperature of 410 mK and that there is no significant low field temperature dependence of I_d or I_c below 150 mK as shown in Figure 3.3 (a)-(b). This indicates that Joule heating is not significant when I<10 μA and that our arrays are in the low temperature limit when measured at 17 mK. Another question is whether quantum tunneling plays a significant role in vortex motion in our arrays. Previous studies[56,57] have observed quantum tunneling of vortices, but these had normal resistances on the order of 20kΩ and large amounts of hysteresis consistent with an underdamped array. The Nb islands on Au discussed in this thesis have a resistance of 31Ω, are not hysteretic, and are in the overdamped limit. This leads to classical vortex behavior and quantum tunneling does not make a significant contribution to vortex transport in our arrays.

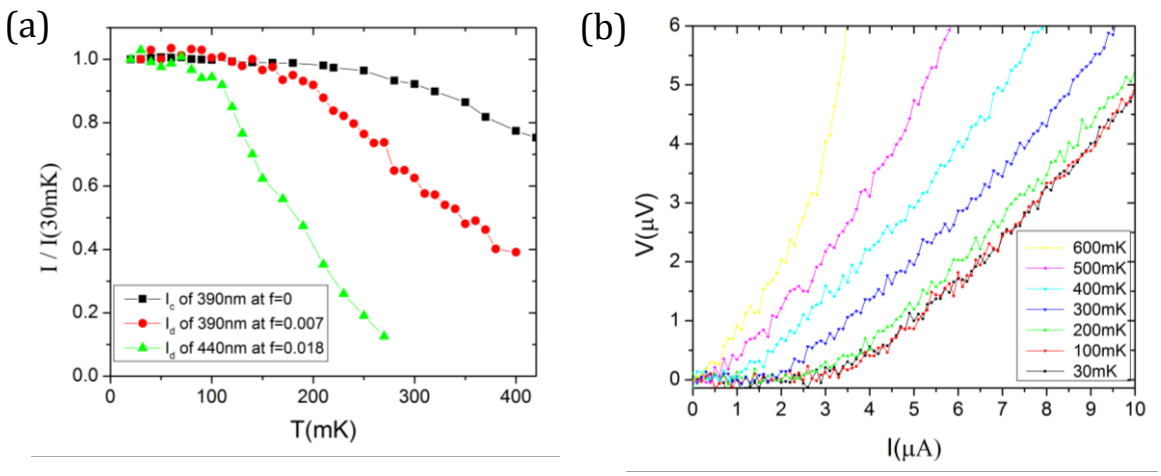

Figure 3.3. Array properties as a function of temperature. (a) I_d and I_c temperature dependence for 390nm spaced (edge to edge) islands arrays at low field values as well as I_c temperature dependence for 440nm islands at f=0.018. (b) *I-V* Measurements performed in 390nm spaced island arrays at f=0.007 at different temperatures.

The measurements shown in Figures 3.4(a) and 3.4(b) were performed at $T = 17\ mK$ and $I<10\mu A$. This places the array in the low temperature limit and the current range prevents significant Joule heating. Figure 3.4(a) shows *I-V* curves and Figure 3.4(b) shows *dV/dI* curves as a function of magnetic field for an array of islands. As shown in Figure 3.4(a), the array transitions from a pinned state ($V=0$) to a flowing vortex state (linear relationship between V and I at a de-pinning current, I_d). Viewed as dV/dI (Figure 3.4(b)), this is a transition is from dV/dI=0 to a constant dV/dI that is referred to as the flux flow resistance. The flatness of dV/dI in the flux flow regime is notable and a highly linear I-V relationship is exhibited, which implies the vortices are moving at a terminal velocity (Lorentz force balanced by dissipative force). The flux flow resistance, R_{ff}, is linear with magnetic field and is consistent with the Bardeen-Stephen model [58], which predicts $R_{ff} \sim 2\, f\, R_n$ for normal state resistivity R_n. Figure 3.4(c) shows that R_{ff} is linearly proportional to f, as expected.

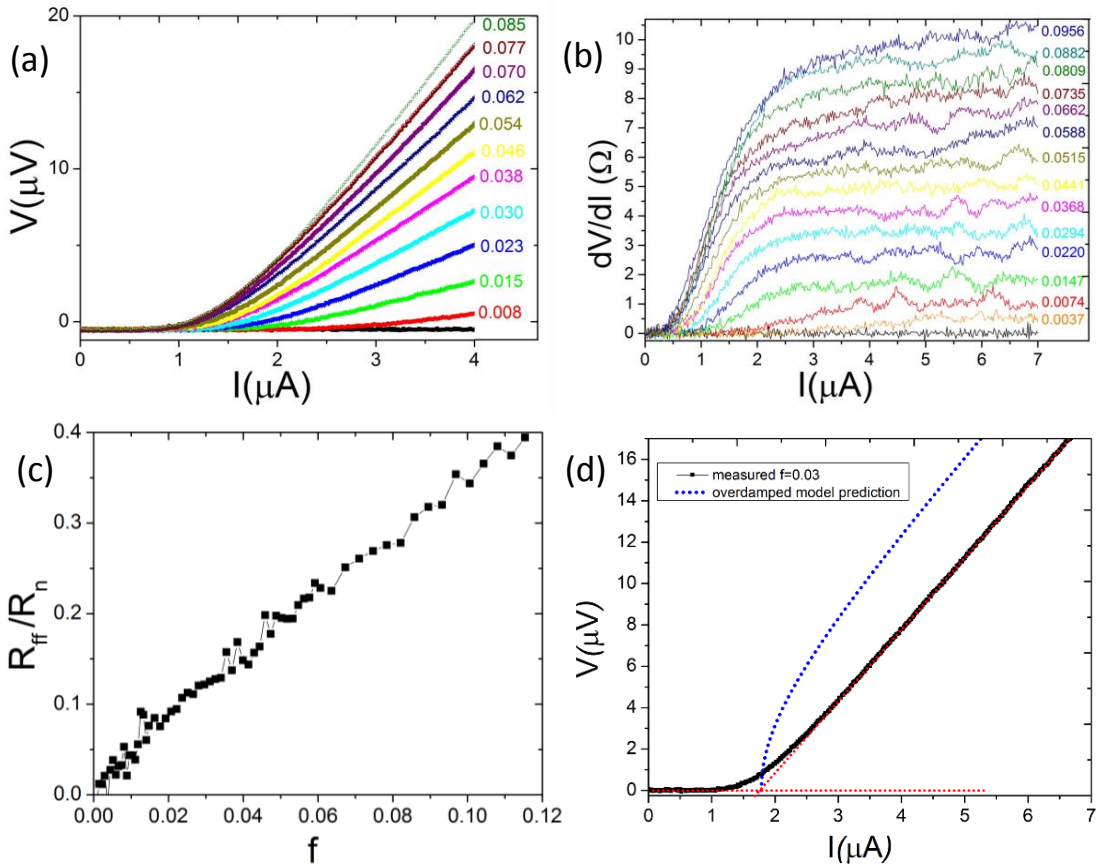

Figure 3.4. Current-induced vortex de-pinning for 390 nm spaced islands at T = 17 mK. (a) *I-V* measurements performed using a swept DC current bias for $I < I_c$ in different magnetic fields. Adjacent numbers indicate the frustration associated with each curve; $f = 1$ corresponds to magnetic field B = 115 gauss. (b) Differential resistance, *dV/dI*, extracted from *I-V* measurements in (a). (c) The flux flow resistance R_{ff} vs f extracted from *I-V* curves. R_{ff} is normalized to the normal state resistance R_n. (d) Measured *I-V* at f = 0.03 (black) compared with the prediction of the overdamped vortex model (dashed blue) in the low filling limit. A linear fit is performed on the superconducting and flux flow regions of the measured curve (red dotted lines). These intersect at a nonzero I intercept.

Contrary to theoretical predictions, we do not observe a differential resistance peak near I_d or any inflection points in the *I-V* measurements on the approach to flux flow. These are essential features of previous models of the transition from pinned behavior. Indeed, any model (such as the tilted washboard model discussed) where the array transitions from pinned behavior ($V \sim 0$) at low currents to flux flow with $V \propto I$ and an I intercept of 0 at large currents requires an inflection point where $d^2V / dI^2 < 0$. The need for a differential resistance peak can be seen in the predicted *I-V* for an overdamped array shown in Figure 3.1(b). The simulated curve initially demonstrates

$V = 0$ pinned behavior at low currents, but then rapidly increases in V at I_d as it transitions to $V \propto I$, necessitating a maximum slope near I_d.

The absence of the peak in differential resistance is not unique to our measurements and is commonly observed in studies of SNS array. It has been previously discussed as a consequence of broadening due to finite temperature[24] and the effect of superposing DC and AC driving currents [59], but these explanations are not convincing for our system. The finite temperature explanation in Rzchowski et al.[24] uses a tilted washboard model similar to the one discussed at the start of this chapter. Simulations of this model are presented in Figure 3.1(d) and show that the peaks persist even when thermal fluctuations are sufficient for significantly nonzero dV/dI around I=0, which indicates a much higher temperature than our experiments. Similarly, since we use DC measurements, the AC driving current argument does not apply. It is also conceivable that vortex-vortex interactions could suppress the peak[60] (via some collective effect), but we have focused on the dilute filling regime and large scale RCSJ array calculations have found behavior described by EQ 2 at comparable fillings (necessitating a peak).

Our data supports another explanation. As shown in Figure 3.4 (d), the measured linear flux flow region has a nonzero intercept in I and is offset from the simulated curve. Since the intercept occurs near I_d, the measured I-V curves can smoothly approach flux flow without an inflection point. The lack of an inflection point can be generally attributed to additional dissipation in the system, suggesting that modifications to the dissipation term are necessary to properly model the system.

3.3 History Dependent Dissipative Force

The dynamics of our system can be explained using a molecular vortex model built around the Langevin equation. Here, *N* vortices are treated as classical objects that are driven by an externally applied force [52, 53]. This classical treatment is valid in low resistance systems such as ours, which are overdamped and do not have significant quantum tunneling of vortices. Since this section is focused on the extremely dilute vortex regime, vortex interactions can be neglected and vortices can be expected to move in roughly a straight line. The dynamics can be described using a one-dimensional Langevin equation with a more general dissipative term [61]

$$m\ddot{x}_i(t) = -\frac{\partial V(x_i(t))}{\partial x_i} - \int_0^t \chi(t-\tau)\dot{x}_i(\tau)d\tau + \epsilon_i(t). \quad (4)$$

where, m controls the inertia of the vortices, $x_i(t)$ is the position of the *i*-th vortex at time t, $V(x)$ is the effective potential felt by each vortex, $\chi(t)$ encodes the dissipative interactions between the vortex and the local environment, and ϵ_i is a stochastic force simulating thermal fluctuations. Due to the low resistance of the system, the vortex lattice is in the overdamped regime and *m* can be set to *0*. The measured voltage is mainly the result of vortices traveling from one edge of the array and is proportional to the average velocity $v = \frac{1}{N}\sum_i^N \dot{x}_i(t)$ of the vortices.

The effective potential V(x) is approximated by the equation

$$V(x) = \frac{F_{barrier}a}{2\pi}\sin\left(\frac{2\pi x}{a}\right) - F_I x \qquad (5)$$

This potential models two properties of the system: a periodic potential of lattice constant, *a*, equal to the distance between islands and a linear potential that produces a Lorentz force, F_I, proportional

to the applied current. $F_{barrier}$ sets the strength of the periodic potential and represents the maximum force from the periodic potential. As discussed in section 3.1, the vortex slows when moving across flat sections of the washboard potential, lowering the average velocity and measured voltage. As a vortex moves through the periodic potential, it slows when crossing potential peaks, lowering the average velocity and measured voltage. The mass term, m, suppresses these $\dot{x}(t)$ oscillations. Increasing mass favors a sharp transition from pinned to $V \propto I$ behavior as well as hysteresis. Since we do not observe a sharp transition or hysteresis, m can be assumed to be negligible and is set to zero. This overdamped treatment is consistent with the low resistance of our system.

Dissipation is commonly given the form $\chi(t) = \eta_1 \delta(t)$, which assumes energy loss is due to instantaneous interactions with the array. As discussed in section 3.1, this leads to a current-voltage relationship of the form $V \propto \sqrt{I^2 - I_d{}^2}$ (massless particles are greatly slowed on level regions of the washboard potential) and a differential resistance peak at $I = I_d$. This current-voltage relationship only converges to $V \propto I$ at high currents, where the driving force is much larger than that of the periodic potential and vortex velocity is given by $v = F_I / \eta_1$. The temperature dependence of V can be solved analytically [55] or simulated by adding a stochastic force, with the results shown in Figure 3.1(d). This model converges to $V \propto I$ at large currents, regardless of temperature; this can be contrasted to the experimental data, which shows a non-zero I intercept.

In order to explain the flux flow behavior, we include a history dependent dissipative force in the function $\chi(t)$. An example of a dissipative force is a force whose response to a motion event drops off exponentially with time after that. Adding this to the dissipative force function leads to $\chi(t) = \eta_1 \delta(t) + \eta_2 \tau_\beta^{-1} e^{-t/\tau_\beta}$, where $\eta_{1,2}$ are free parameters and τ_β is the timescale of the

dissipative force. The effects of a history dependent dissipative force on an overdamped particle are shown in Figure 3.5, where $\eta_2 = 10\eta_1$ and τ_β is given in terms of $\tau_a = \frac{a^2(\eta_2+\eta_1)}{2\pi V_p}$, which corresponds to the time taken by the large mass particle modeled in Figure 3.5 to move across one period of the potential at a current infinitesimally greater than I_d. A τ_β much shorter than the time taken to cross one period of the potential yields the same behavior as the purely instantaneous dissipative response, but longer τ_β enhances $\dot{x}(t)$ oscillations, leading to very different *I*-*V* behavior. When τ_β is much longer than the period crossing time, the dynamic region is highly linear with an *I* intercept of I_d, similar behavior to what we observe in our experiment.

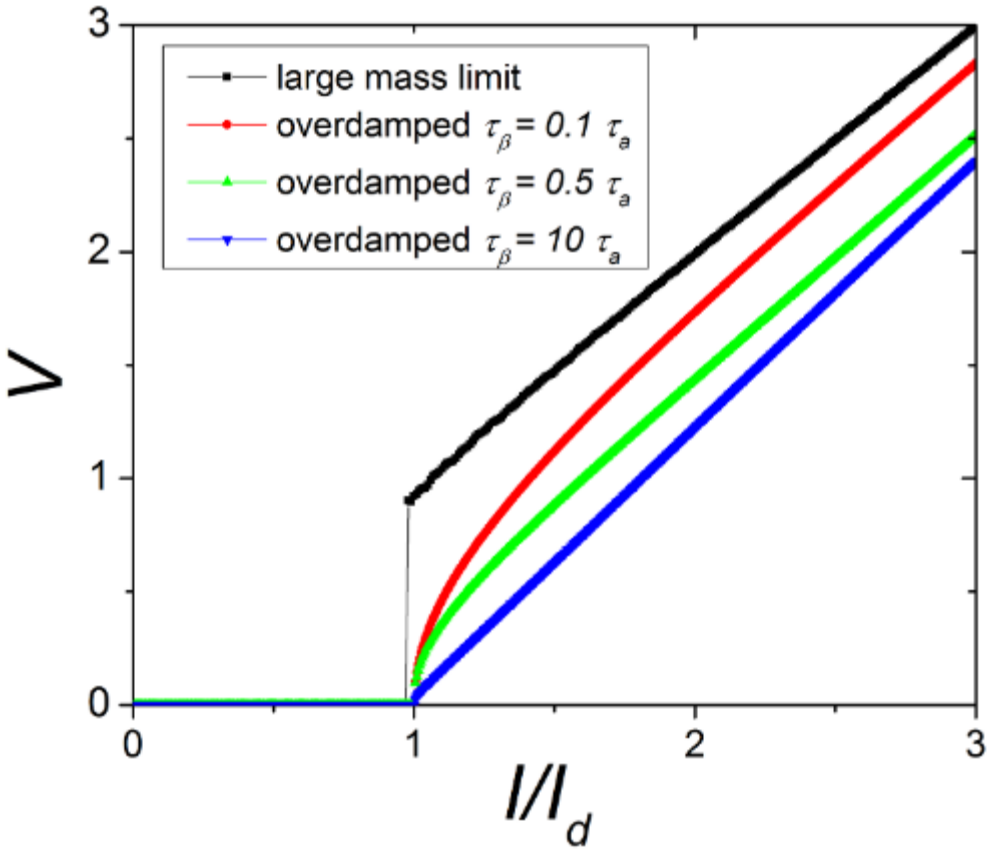

Figure 3.5. Simulated *I-V* behavior with a history dependent dissipative force. Curves showing the effects of the mass term and the timescale of the dissipative force, τ_β, in a periodic potential. Three curves show the predictions for the low mass limit with different dissipative force timescales. $\tau_\beta = 0.1\ \tau_a$ is indistinguishable from the instantaneous dissipative force time constant case, but much longer time scales result in a linear region with an *I* intercept near I_d.

The current-voltage relationship does not strongly depend on the form of the history dependent component of $\chi(t)$. $\chi(t) = \eta_1\delta(t) + \eta_2 t_c^{-1}\theta(t_c - t)$ yields similar behavior in the large t_c limit and is less computationally intensive than the exponential expression. The parameters $\eta_2 = 0.4\eta_1$ and $t_c \sim 14\,\tau_a$ can be used to place the system in the long timescale dissipative force regime, removing the differential resistance peak. Changes in I_d caused by low field Meissner currents and dilute limit vortex-vortex interactions are simulated by adding an edge barrier and a stochastic force, resulting in Figure 3.6(a) and Figure 3.6(b)]. This yields excellent qualitative agreement with between theory and experiment, suggesting that history dependent dissipation

could have a significant contribution to vortex dynamics in overdamped SNS arrays. While a similar mechanism has previously been considered to study a continuum theory of the plastic flow of vortices [60], the connection to the absence of a peak in the differential resistance was not discussed.

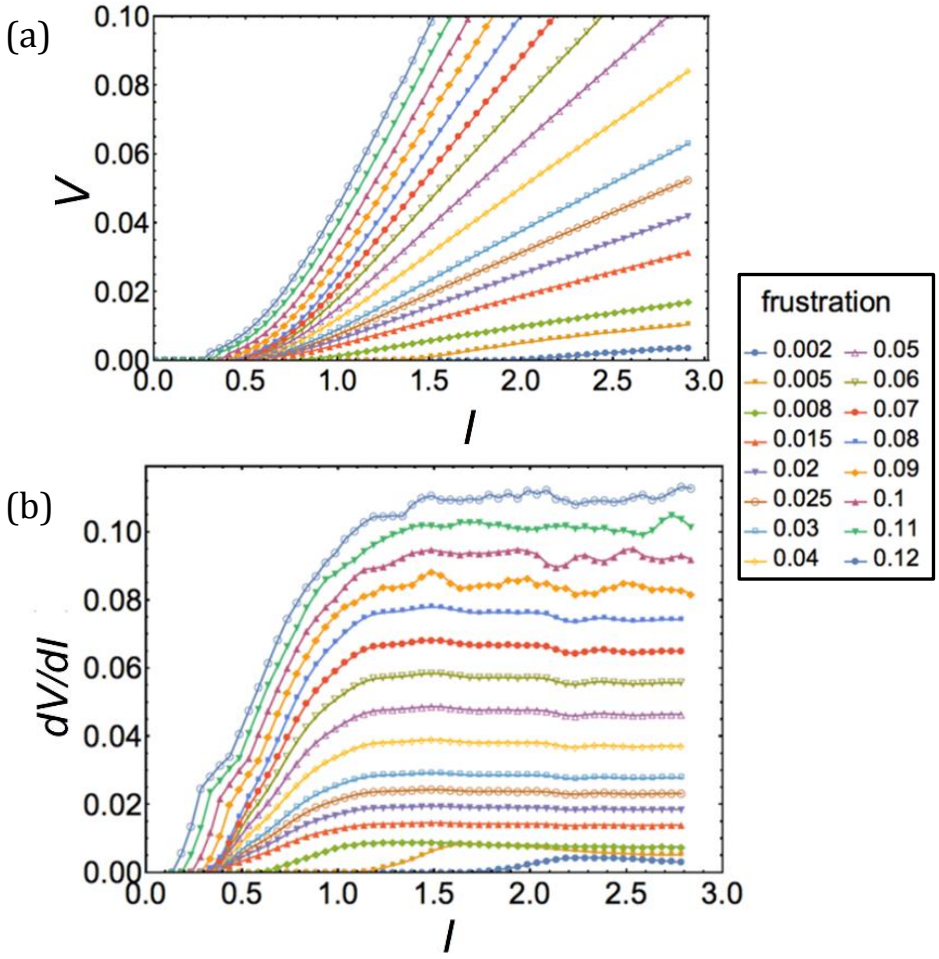

Figure 3.6. Simulated SNS array behavior as a function of frustration. (a) Simulated voltage vs current and (b) differential resistance vs current for a generalized Langevin equation with flat time dependent dissipation where $\tau_\beta \sim 14\ \tau_a$. Model includes an edge potential at low fillings.

Although the microscopic sources of energy loss are not completely understood [62], one can roughly think of energy dissipation as due to quasiparticles interacting with normal electrons inside vortex cores; the quasiparticles may get excited from impurities in the superfluid, or could

leak out of the vortex cores when a current is applied [63]. Memory effects in our system could arise because of a delayed time-scale for the healing of the superfluid density along the path traversed by the vortices as they move through the system. The trail left behind by the vortices would then contribute to the dissipation measured in the experiment.

Chapter 4. Interacting Vortex Regime

4.1 Introduction

How crystalline order is destroyed in the presence of disorder is a fundamental question in condensed matter physics and determines the structure of a wide range of systems, including solids and magnetic materials. Disorder can manifest itself in two ways: interface structures like domain walls in polycrystalline structures[64,65] or in bulk structures like disordered glasses[66]. Vortex systems provide excellent test-beds for studying the introduction of disorder into crystalline structures. A perfectly ordered type II superconducting film has a crystalline Abrikosov lattice[12,67] , but the introduction of disorder in the film can destroy this crystalline structure and result in unusual phases. This has been demonstrated in disordered superconducting films, which have a de-pinning current peak as temperature is increased towards the critical temperature, T_c. A combination of electronic transport measurements and neutron diffraction measurements have found that this peak can be explained as a transition from a weakly pinned quasiperiodic "Bragg glass" [66,68] into a polycrystalline state[17 ,18, 19, 69] as temperature increases and the vortex lattice relaxes.

Superconductor-normal-superconductor (SNS) arrays offer a controlled way of studying disorder, allowing it to be tuned with magnetic field. While disorder in a film is random, SNS arrays provide a periodic potential defined by array geometry and have a potential well filling fraction that can be controlled using a magnetic field (B) [24]. Crystalline vortex structures form when the vortex lattice is commensurate with the array's potential wells and can be identified via electrical transport measurements as dips in magnetoresistance [25] and peaks in de-pinning currents [26]. Disorder can be introduced into these systems by shifting the filling fraction away

from commensurate filling values. Since most studies of SNS arrays have focused on crystalline structures, the structure at incommensurate fillings is not well understood and it is not known if the system is glassy or polycrystalline in this regime. Here, we describe transport measurements of an SNS array, where we observe two-step vortex transitions at incommensurate fillings: first from pinned to lattice defect motion, then from lattice defect to bulk lattice motion. Comparing these measurements with a dynamic vortex model [51,52,53], we show that this two-step transition is indicative of domain wall motion in a polycrystalline vortex lattice and not a vortex glass. This section covers work that will soon be published.

4.2 Measurement

Samples are studied using four-point measurements in a dilution refrigerator at 17 mK, sweeping DC current and measuring voltage, with values such as dV/dI obtained by taking a numerical derivative. Vortices experience a periodic potential from the island array [24], where the local energy minimum is at the center of each island triangle, and an energy barrier exists at the array edges. As discussed in previous sections, the current applies a Lorentz force on the vortices. If sufficient to overcome the energy barrier, the Lorenz force will de-pin vortices and drive their motion, which is measured as a voltage across the sample. The number of vortices per island triangle is determined by the magnetic field and island spacing, and is characterized by the number of flux quantum per plaquette, or $f=\Phi/\Phi_0$, where Φ is the flux through a unit cell and $\Phi_0 = h/2e$ is the quantum of flux. The devices studied are similar to those in sections 3, consisting of triangular arrays of superconducting Nb islands on normal metal films. The normal metal film (1nm Ti, 10nm Au) is patterned in a four-point measurement configuration. A triangular array of Nb islands that are 70 nm thick, 260 nm in diameter, and have 490 nm edge-to-edge spacing is

then patterned on top of the normal metal film using electron beam lithography and electron beam evaporation.

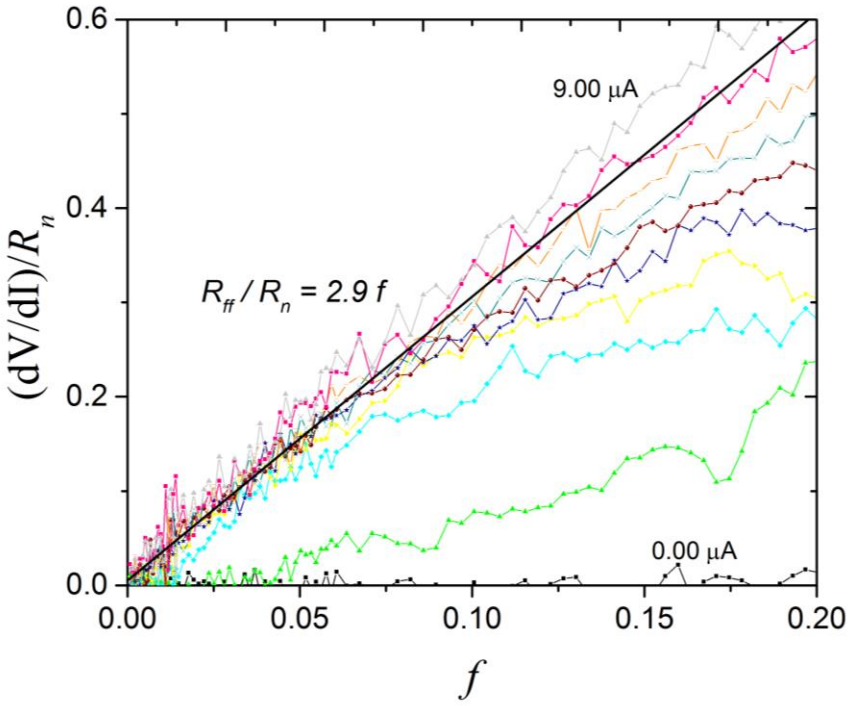

Figure 4.1. *dV/dI* as a function of field at low fillings. Normalized differential resistance at different bias currents as a function magnetic field. As current increases at low fillings, there is a rapid transition from $dV/dI=0$ to a flux flow resistance proportion. As f is increased, the upper *dV/dI* lines branch off from R_{ff}, startng at $f \sim 0.08$, due to the increasing importance of vortex-vortex interactions.

4.3 Measurement of Lattice Flow Regime and Commensurate Fillings

The dilute filling behavior of the arrays (i.e., at small f values) is shown in Figure 4.1, a plot of dV/dI as a function of f for different I (obtained by taking the derivative of an I-V measurement). In this regime, the array undergoes a current driven transition from pinned vortices ($dV/dI=0$) to flux flow (constant dV/dI) at a de-pining current, I_d. The flux flow—or lattice flow—regime occurs when all vortices are moving at a terminal velocity, where the Lorentz force is equal to a dissipative force, resulting in a linear relationship between I and V. This leads to a constant

d*V*/d*I* that we refer to as the flux flow resistance, R_{ff}. R_{ff} scales linearly with filling fraction *f*, as the measured *V* is proportional to the total number of moving vortices. This is shown in Figure 4.1, where, for sufficient currents and low *f* values, the d*V*/d*I* curves fit to a single black line representing R_{ff}. When plotted on a broader range in Figure 4.2, the extrapolated fit to R_{ff} represents an upper limit to the *dV/dI* measured for a given *f* and indicates when all vortices are flowing.

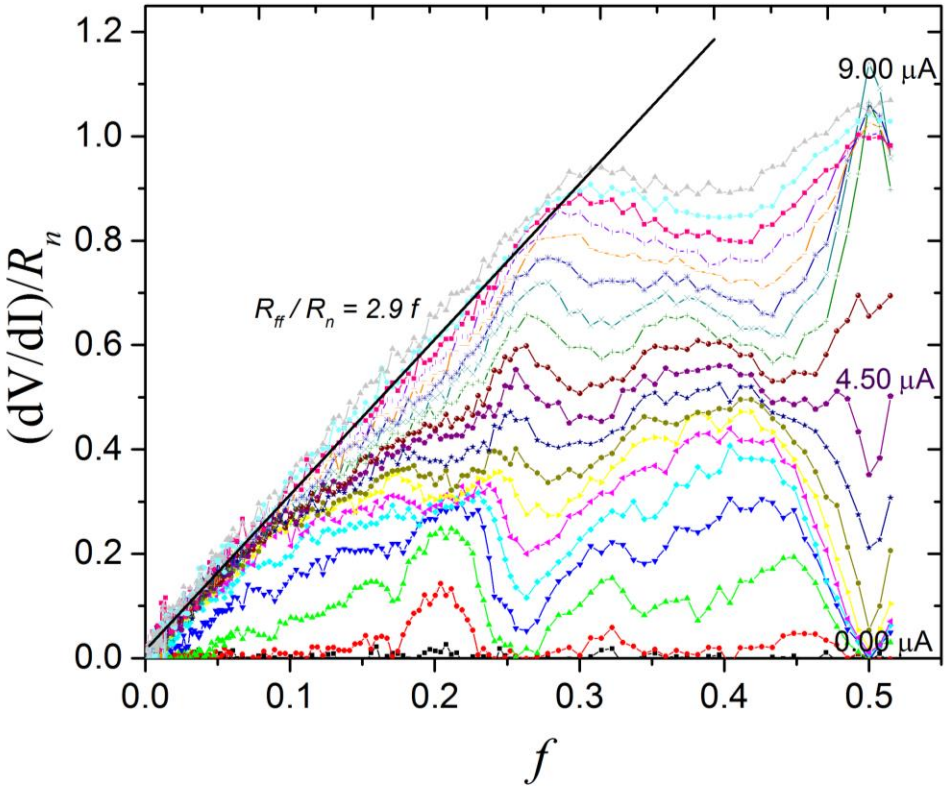

Figure 4.2. *dV/dI* as a function of field. Normallized differential resistance at different bias currents as a function magnetic field. At higher fillings, dips associated with commensurate fillings are visible at *f=0.166*, *0.25*, *0.33*, and *f=0.5*. Intermediate clusterings of lines associated with intermediate flow behavior are visible at *f=0.2* and, to a lesser extent around, *f=0.35*.

At larger *f* values, *dV/dI* no longer has a linear relationship with *f* for most applied currents. This is visible in Figure 4.1, when a number of curves start to diverge from the R_{ff} fit at $f > 0.05$; the effect is even more pronounced in Figure 4.2, where a pattern of peaks and dips emerge when $f > 0.1$. The departure from linear *dV/dI* occurs because greater vortex density results in stronger

vortex-vortex interactions. Vortex-vortex repulsion usually leads to weaker pinning as filling is increased. However, at special fillings—e.g., $f = 1/12, 1/6, 1/4, 1/2$—the vortex lattice is commensurate with the array potential wells, resulting in crystalline vortex orderings and strong pinning, as evidenced by dips in *dV/dI* and a greater de-pinning current at commensurate fillings.

4.4 Two Step Transition at Incommensurate Filling

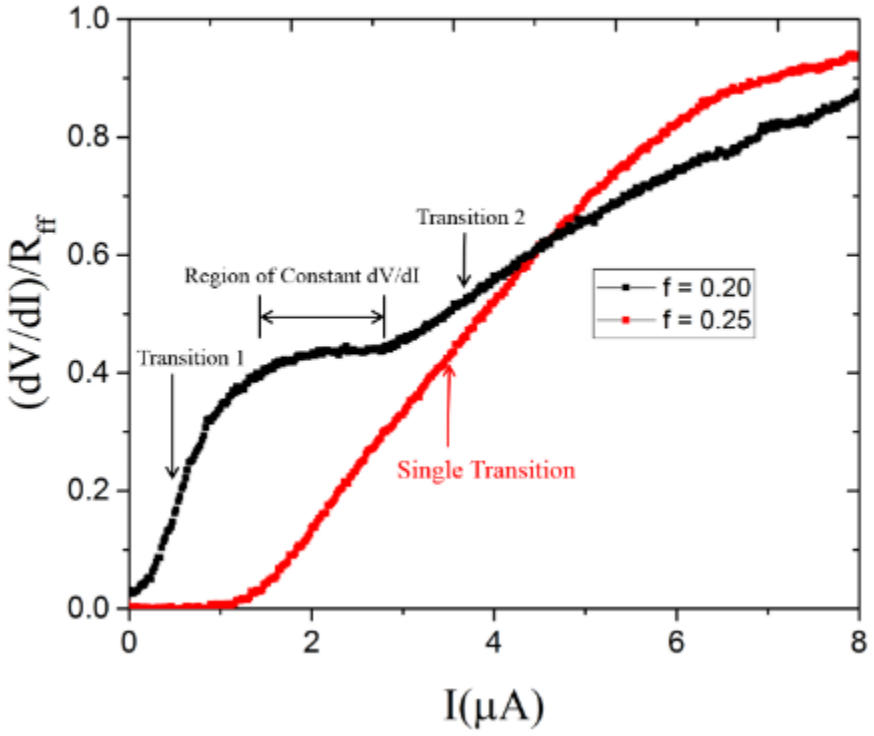

Figure 4.3. dV/dI as a function of current. When dV/dI is plotted as a function of current, the clustering of lines is visible as an intermediate flat region between two steps at *f=0.20* . This is in contrast to the single step transition at *f=0.25*.

Commensurately and incommensurately filled lattices exhibit different dynamic behavior. The dynamics as a function of current can be seen in Figure 4.3, which plots d*V*/d*I* vs *I* for the commensurate filling *f=0.25* alongside the incommensurate pinning *f=0.20*. Driven from pinned to flux flow, the commensurate filling undergoes a single transition, while the incommensurate

filling undergoes two distinct transitions separated by an intermediate region of constant dV/dI. Similar behavior can be seen in Figure 4.2, where incommensurate fillings have intermediate clusterings of lines, as exemplified at $f = 0.20$. In contrast the commensurate fillings transition rapidly into flux flow, resulting in peak reversals where low current dips turn into peaks at higher currents (e.g., as at $f = 0.5$). Similar peak reversals have been observed in previous works[25] and used as evidence for a vortex Mott-insulator to metal transition [27].

In order to characterize incommensurate lattice dynamics, we plot the transition locations as a function of field and current in Figure 4.4. Since the transitions are associated with steps in dV/dI, they can be identified as d^2V/dI^2 peaks, or the bright regions of Figure 4.4. For commensurate fillings, depinning transitions occur at higher currents, as indicated by the arrows in Figure 4.4. While dilute fillings and commensurate fillings only have a single transition (only one visible d^2V/dI^2 peak for a given f), incommensurate fillings often undergo a two-step transition with two visible d^2V/dI^2 peaks. This is evident in Figure 4.4, where the incommensurate fillings indicated by dashed lines have first transitions marked by blue circles and secondary transitions marked by red Xs.

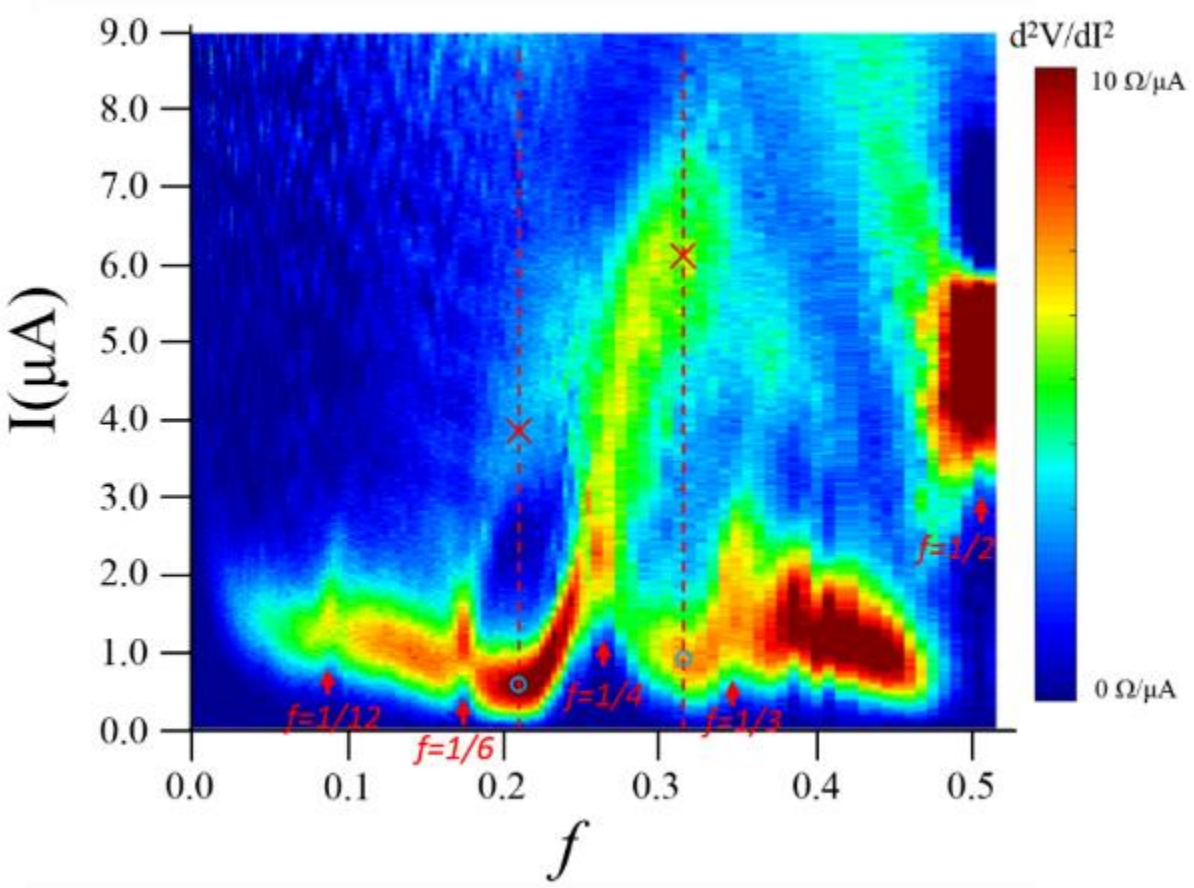

Figure 4.4. d^2V/dI^2 as a function of current and frustration. Transition steps can be mapped using d^2V/dI^2. Higher d^2V/dI^2 values (light blue, green, and red) correspond to a transition step. Commensurate fillings are marked with red arrows and undergo a single transition. Example incommensurate fillings are marked with a red dashed line and undergo two transitions, the first marked with a blue circle and the second marked with a red X. The first and second transition curves split apart as filling is shifted away from a commensurate value.

The single transitions smoothly split into two transitions as filling is shifted away from commensurate values. This can be seen in Figure 4.4, where the single transition at *f=1/6* smoothly splits into two diverging transition curves as the filling is increased, with the upper curve marked with an "X" and the lower curve marked with an "O" at *f~0.21*. Another prominent splitting is also visible as the field is increased from *f=1/4* and a less prominent secondary transition curve splits off as the filling is decreased from *f=1/6*, but only is visible over a short range of fillings. The smooth splitting as a function of filling indicates that this behavior is determined by lattice structure, with the vortex lattice transitioning from pinned regime to an intermediate vortex motion

regime to a lattice flow regime. This splitting has not been previously discussed and presents implications regarding vortex structure and motion.

4.5 Simulation

To better understand the dynamic behavior in the different regimes, including the d^2V/dI^2 peak splitting, we again use a molecular vortex model based on the Langevin equation, but include a vortex-vortex interaction term. This has equations of motion given by

$$m\ddot{x}_i(t) = F_{applied} - \frac{\partial V(x_i(t))}{\partial x_i} - \eta\dot{x}_i(\tau) + \varepsilon_i(t) + \sum_{j=1}^{N} U\left(\frac{x_i(t) - x_j(t)}{L_{int}}\right), \quad (4.1)$$

where m is a mass term related to capacitance, $F_{applied}$ is the Lorentz force (proportional to the applied current), $V(x_i(t))$ is a periodic potential defined by the array, $\varepsilon_i(t)$ is a stochastic force used to simulate finite temperature, and $U(x_i(t)-x_j(t))$ is the mutual repulsion between vortices. We simulate current sweeps at regular magnetic field intervals by varying the number of vortices per potential well and applying a driving force. The implementation and investigation of this molecular vortex model is complicated enough to warrant its own section, chapter 5, and this section is meant to summarize the major findings. It is also worth noting that some features, such as as dV/dI peaks at the de-pinning current, are not described by the model used here (the history dependent dissipation term is absent for the sake of simplicity and computational efficiency). Instead, the effect of this term is shown in chapter 5.

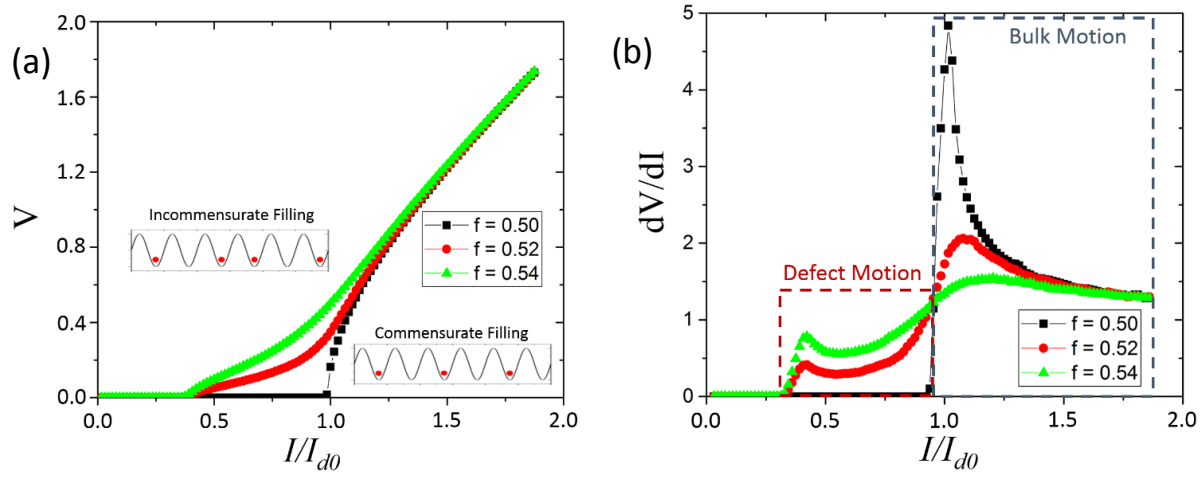

Figure 4.5. One dimensional simulation of array (a) Simulated I-V behavior for commensurate (*f=0.5*) and incommensurate fillings (*f=0.52,0.54*). Right inset shows the half filling arrangement. Left inset shows an incommensurate filling with defects in the form of vortices in adjacent wells. (b) Simulated d*V*/d*I* measurements. At commensurate values, the system rapidly transitions from pinned to bulk vortex motion. As field is increased (*f=0.52,0.54*), defects are added. This results in a transition from pinned to defect motion to bulk vortex motion.

A basic one dimensional (1D) simulation can replicate the two-step transition for incommensurate fillings. Shown in Figure 4.5(a), the lattice undergoes a direct transition from pinned to flux flow at commensurate fillings, such as *f=0.50*. Due to the ordered arrangement of vortices [Figure 4.5(a) lower right inset], the vortex lattice moves in unison and exhibits dynamics similar to that of a single vortex. As additional vortices are added, defects enter the lattice [Figure 4.5(a) upper left inset], separating ordered domains. These defects require a lower depinning force than the rest of the lattice and begin moving prior to the lattice depinning current, resulting in a transition from pinned to defect flow to lattice flow. A direct comparison of predicted d*V*/d*I* is provided in Figure 4.5 (b) for the different transport regimes. Notably, the distinct two-step transition occurs when defects occur on interfaces separating ordered regions, analogous to domain walls. In contrast, higher values of disorder than shown in Figure 4.5 yield an amorphous state, exhibiting only a single transition [for a more detailed description, see chapter 5].

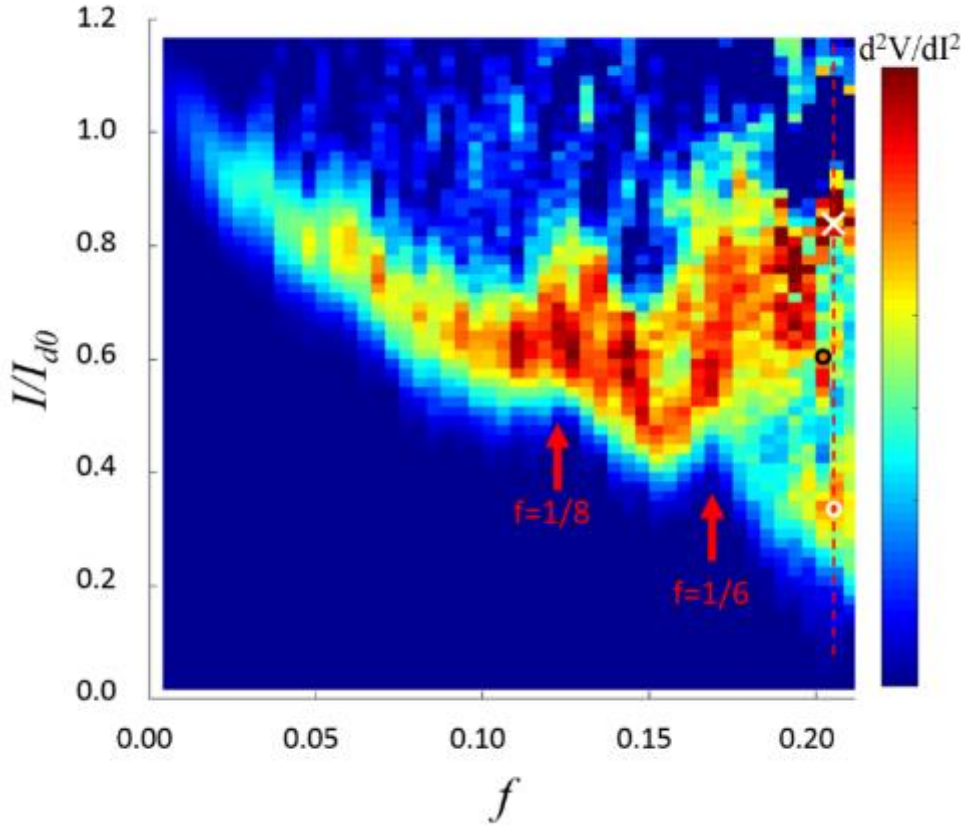

Figure 4.6. 2D simulation of triangular array. Simulated d^2V/dI^2. Depinning current peaks are visible at *f=1/8* and *f=1/6* . At *f=1/6*, a second transition splits off from the de-pinning current when current is increased and the area in between the two transitions is a defect motion regime. An incommensurate filling is shown wit a dashed line. A white circle shows the first transition. A white X shows the second transition.

To simulate a 2D system, we use a periodic potential similar to the one produced by the triangular island array, incrementally sweep current at different vortex populations, and extract the vortex motion. As shown in Figure 4.6, this simulation reproduces the basic features of the data in Figure 4.4: de-pinning current peaks at commensurate fillings and a second d^2V/dI^2 peak that splits as the filling is altered from commensurate values. Similar to our measurements, the lowest commensurate filling with significant splitting is *f=1/6*, which is marked in red in Figure 4.6; the second transition is marked with a white arrow. Correspondence between measured and simulated transport data suggests this model could shed light on vortex lattice structure. Figure 4.7(a) shows

vortex motion in the intermediate transport regime between the split transitions (f=0.20 and I=0.60, marked as a red dot in Figure 4.6), with black circles showing initial location and white circles showing ending location over a short period of time, roughly corresponding to the time taken for a vortex to cross from one well to another [for vortex lattice motion, see Figure 4.7(b)]. Vortex motion occurs primarily in defects, which appear as cracks that form between crystalline structures. This not only indicates that the intermediate transport regime involves defect motion, but shows a polycrystalline structure with defects appearing on the interfaces separating crystalline domains. These results suggest the intermediate transport regime involves domain wall motion.

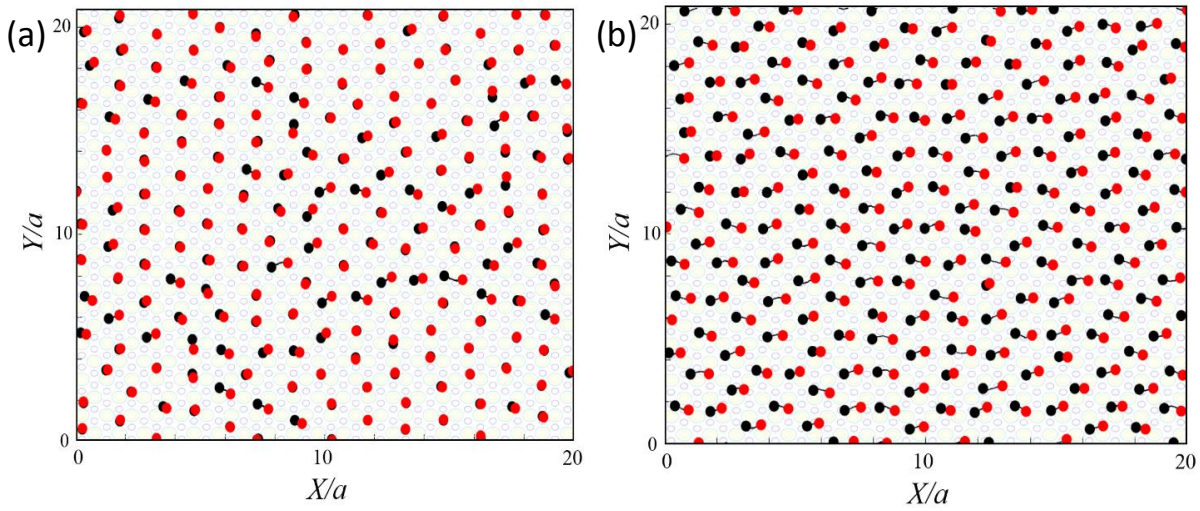

Figure 4.7. 2D simulated motion. The potential supplied by the SNS array is displayed in contours with maxima in yellow and minima in dark blue. Black circles are simulated vortices and red circles show their position a short time afterwards (with a black line showing the path in between). (a) Defect motion is simulated using parameters *I=0.6* and *f=0.20*. Only a small number of vortices move at once, mostly on the interfaces between different crystalline structures. (b)Flux Flow is simulated using a value of *I=2.2* and *f=0.20*. Unlike the defect motion regime, all vortices are in motion at once.

4.6 Conclusion

Thus, the two step transition we observe at incommensurate fillings is consistent with a transition from pinned vortices to lattice defect motion to lattice flow. Molecular vortex model simulations suggest that this motion occurs on the edge of crystalline domains, providing evidence

for domain wall motion and polycrystalline structure in this system. This disordered structure is unique compared to those typically explored in previous vortex matter studies, which dealt with glassy structures.

Chapter 5. Vortex Simulation with Interacting Vortices

This section provides a detailed description of the simulations used in chapter 4, providing enough information so that they can be reproduced and a supplementary analysis of the results of the simulation. The basic equations of motion are given by EQ 4.1, which are then solved numerically via Euler's method. The details such as the form that vortex repulsion takes and how the 2D model is implemented are contained here. Additional information about quasiperiodic vs domain structure is also presented here.

5.1 Simulating Vortex-Vortex Repulsion

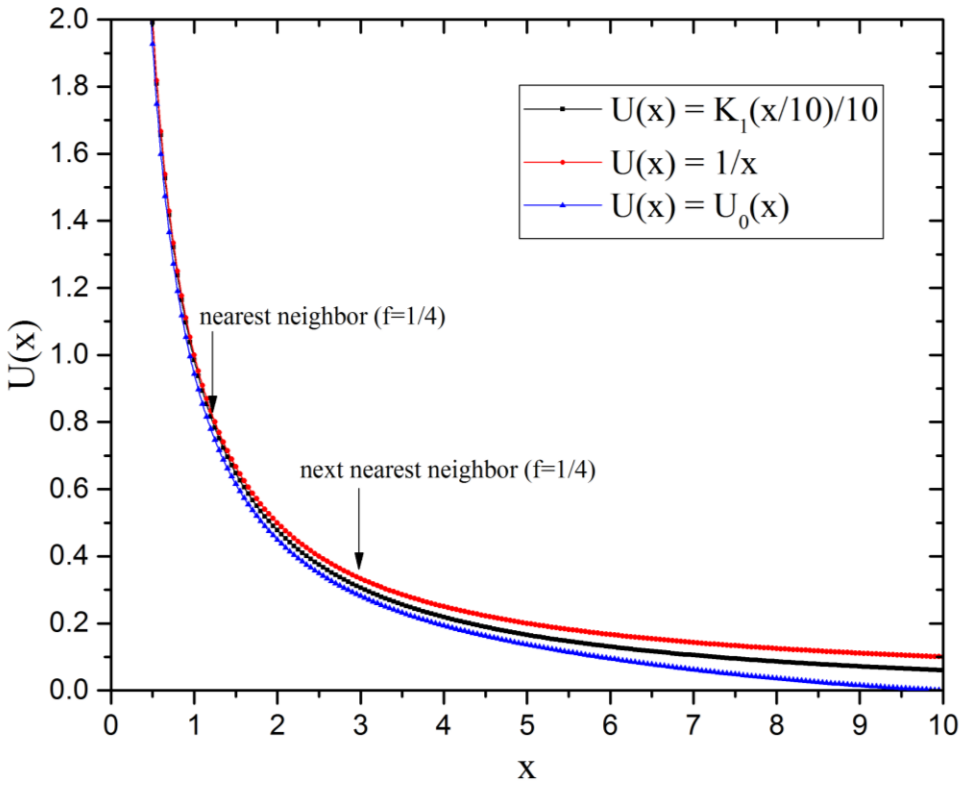

Figure 5.1. Vortex-Vortex Repulsion as a function of distance The different functions discussed as repulsion terms are shown. The function $U_0(x)$ discussed in equation S1 is a decent approximation of the predicted repulsion terms for nearest neighbor and next nearest neighbor interactions.

The magnitude of the vortex-vortex repulsion force is given by $U(X)=K_1(X/L_{int})$, where $K_1(x)$ a modified Bessel function of the second kind. In the long interaction limit ($L_{interaction}>>a$, where a is center to center island spacing), which is applicable for arrays, this approaches $U(X)=C/X$ where C is a constant modifying the magnitude of the repulsion. In order to have the calculations scale in a reasonably efficient way, interactions between vortices over $10a$ away are ignored. To avoid artifacts from vortices entering and leaving interaction ranges of other vortices, we smoothly tapper the interaction range using the following form:

$$U(x) = BU_0(x) = B\left(\frac{a}{x\left[1+\exp\left(\frac{|x|-8a}{2a}\right)\right]} - \frac{1}{10(1+\mathrm{e})}\right) \quad (5.1)$$

As shown in Figure 5.1, this is a reasonable approximation for nearest neighbor and next nearest neighbor interactions in the regime of interest, while effectively ignoring interactions further than that.

5.2 One Dimensional Simulation

The one dimensional system is given by the potential,

$$V(x) = \frac{Aa}{2\pi}\sin\left(\frac{2\pi x}{a}\right) - F_I x \quad (5.2)$$

Where A controls barrier height and F_I is the force resulting from the applied current. The differential equation for an overdamped vortex array is then solved using Euler's method. This is an iterative method that repeats the following calculation over short periods of time, Δt,

$$\dot{x}_i(t) = \frac{1}{\eta}\left(F_I - A\cos\left(\frac{2\pi x_i(t)}{a}\right) + \epsilon_i(t) + B\sum_{j=1}^{N} U_0\left(x_i(t) - x_j(t)\right)\right). \quad (5.3)$$

$$x_i\left(t+\Delta t\right)=x_i\left(t\right)+\dot{x}_i(t)\Delta t. \quad (5.4)$$

The free parameter of in this equation is the ratio between the periodic potential parameter, *A*, and the repulsion parameter *B*, a ratio that determines the stiffness of the lattice. The stochastic force, $\epsilon_i\left(t\right)$, is obtained using a random number generator with an exponential distribution of the form

$$\exp\left(-\frac{|\epsilon_i(t)|}{kT}\right) \quad (5.5)$$

The simulation seeds *N* vortices in 50 wells (*f=N/50*) and then performs a slow anneal from high temperature to low temperature to find a ground state configuration, imposing periodic boundary conditions. We then run the simulation starting with this ground state at varying currents. The results can be seen in Figure 5.2 with two lattice stiffness parameters: *B/A=2* and *B/A=6*. A stiffness of *B/A=2* results in broad two step regions around *f=0.5* and *f=1.0* (dark and light blue). In contrast, a stiffness of *B/A=6* has a distinct two step transition only in relatively narrow range around *f=0.5* and *f=1.0*.

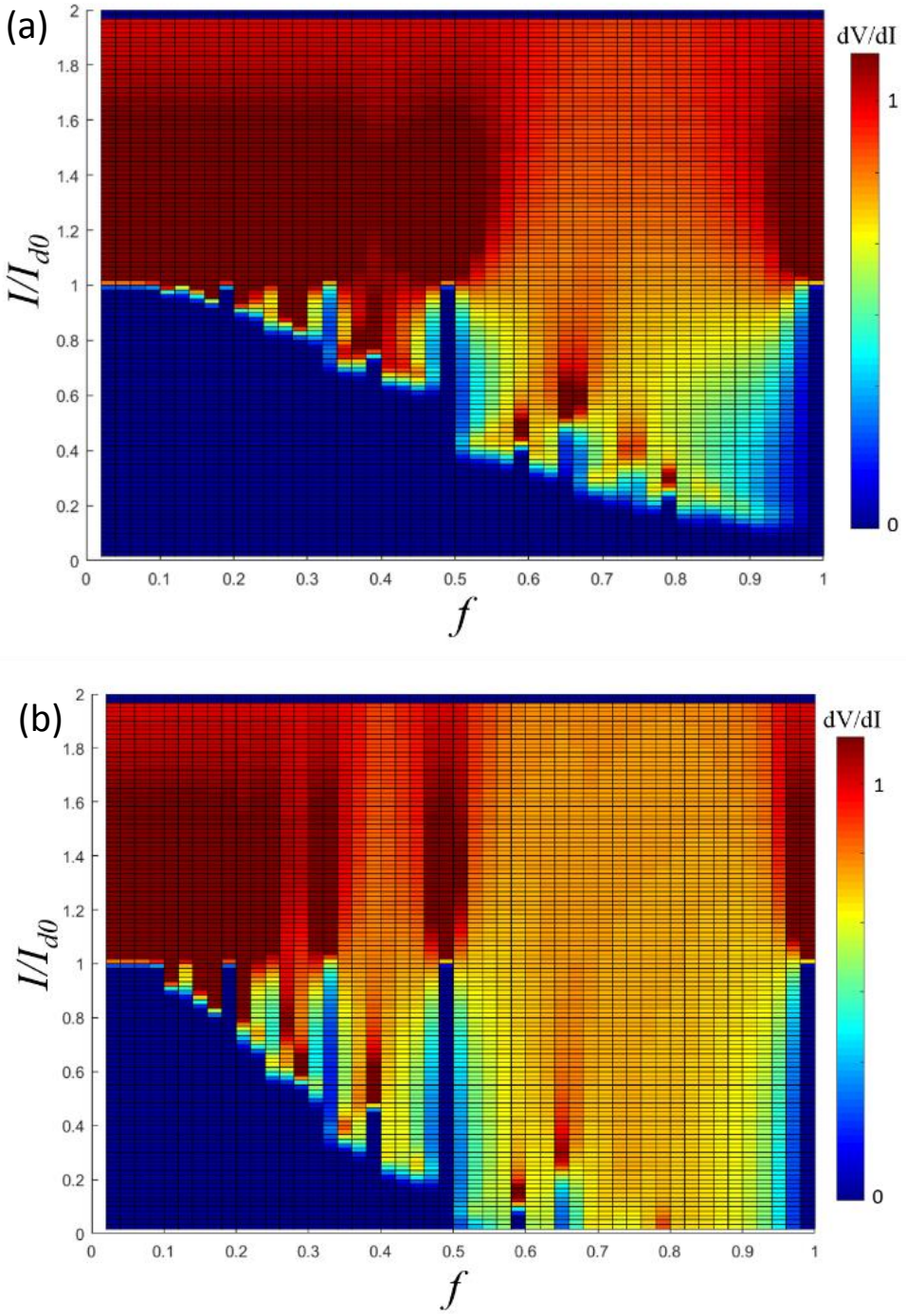

Figure 5.2. Simulated 1D *dV/dI* as a function of current and field. (a) *B/A*=2.0, which is used in Figure 3, has visible intermediate steps associated with defect motion near commensurate fillings, most prominently just above *f=0.5* and just below *f=1.0*. (b) B/A=6.0 has a much stiffer lattice, resulting in narrower regions with two steps. Instead, the stiffer lattice favors lattice motion.

The relationship between vortex lattice structure and the presence (or absence) of a two-step transition is investigated in Figure 5.3, which shows the vortex structure at both *B/A=2* and *B/A=6*. At the *f* values given, *B/A=2* exhibits a prominent two step transition and *B/A=6* either exhibits a less visible two step transition or has only a single step, providing a comparison between the two observed transport phenomena. *B/A=2* [Figure 5.3 (a)(c)] results in well-defined defects that are limited in area to one or two wells: *f=0.54* yields defects in the form of vortices in adjacent wells and *f=0.9* yields defects in the form of empty wells in an otherwise filled lattice. In both cases, the defects can be interpreted as domain walls separating ordered domains, with *f=0.54* defects each separating two half-filled domains and the *f=0.9* defects each separating two entirely filled lattices.

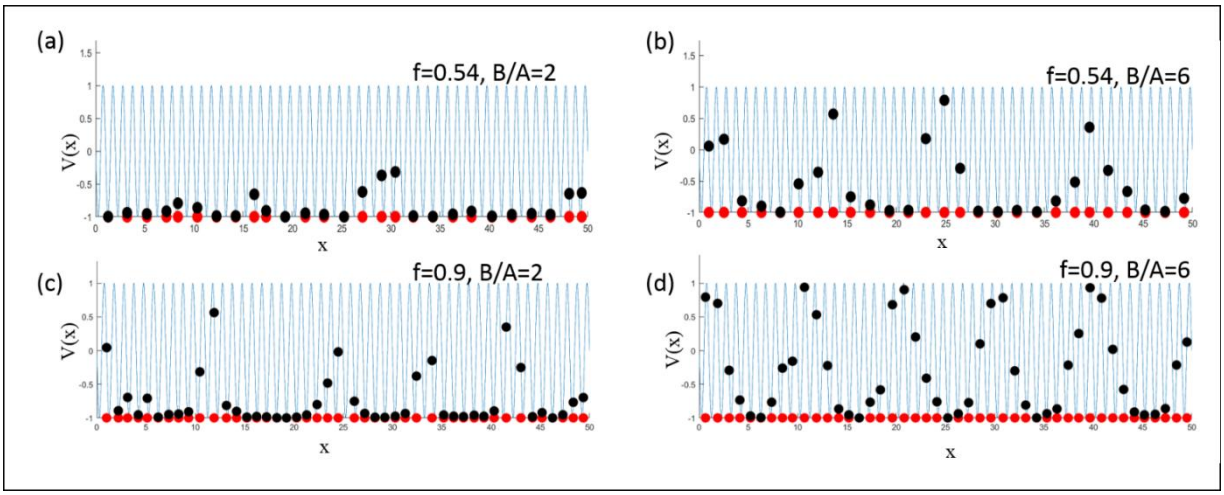

Figure 5.3. Simulated 1D vortex arrangement as a function of stiffness and repulsion. Blue lines represent the periodic potential, the red dots at the bottom of each graph show the x position of vortices, and the black dots show the potential energy of the vortices as well as x position. (a) *f=0.54* and *B/A=2.0* yields defects in the form of a pair of vortices in adjacent wells. These defects separate ordered regions with half the wells occupied. (b) *f=0.54* and *B/A=6.0* vortices do not sit in the wells and are not separated by integer well periods. Disorder appears to manifest in a quasiperiodic structure rather than in the interface between two ordered domains as in (a). (c) has defects appear as empty wells separating domains with every well filled. (d) Greater vortex-vortex repulsion once again yields a quasiperiodic structure. It is notable that (a) and (c) exhibit a two step transition in Figure 5.2 (a), but (b) and (d) undergo a single transition in Figure 5.2(b).

In contrast, *B/A=6* defects are more difficult to identify spatially. Rather than appear as a pair of adjacent vortices or as an empty well, these defects are groupings of perturbed vortices that

no longer rest in the center of the wells. As seen in Figure 5.3 (b)(d), the defects occur over a region 10 wells wide, with vortices either perturbed towards the center of the defect (*f=0.54*) or away from the center of the defect (*f=0.90*). At filling *f=0.54*, there are some segments of vortices that are unperturbed, allowing for a visible intermediate step. At *f=0.9*, the defects are close enough for the lattice to take on a quasiperiodic structure and there is only a single transition. Thus, the two step transition is a signature of distinct defects, which form on the interfaces between ordered domains.

5.3 Absence of Differential Resistance Peak in Experimental Data

While a differential resistance peak is predicted in the simulations, it is absent in experimental simulations. We have previously addressed the and the associated I-V behavior using a history dependent dissipative force. The inclusion of a history dependent dissipative force for a 1D system with *B/A=2* is shown in Figure 5.4. Here, the inclusion of the term removes the peaks on both the defect motion and the lattice motion steps. Since this does not fundamentally alter the types of vortex motion occurring, we do not include this term in any other section of this work for simplicity and to save computational resources.

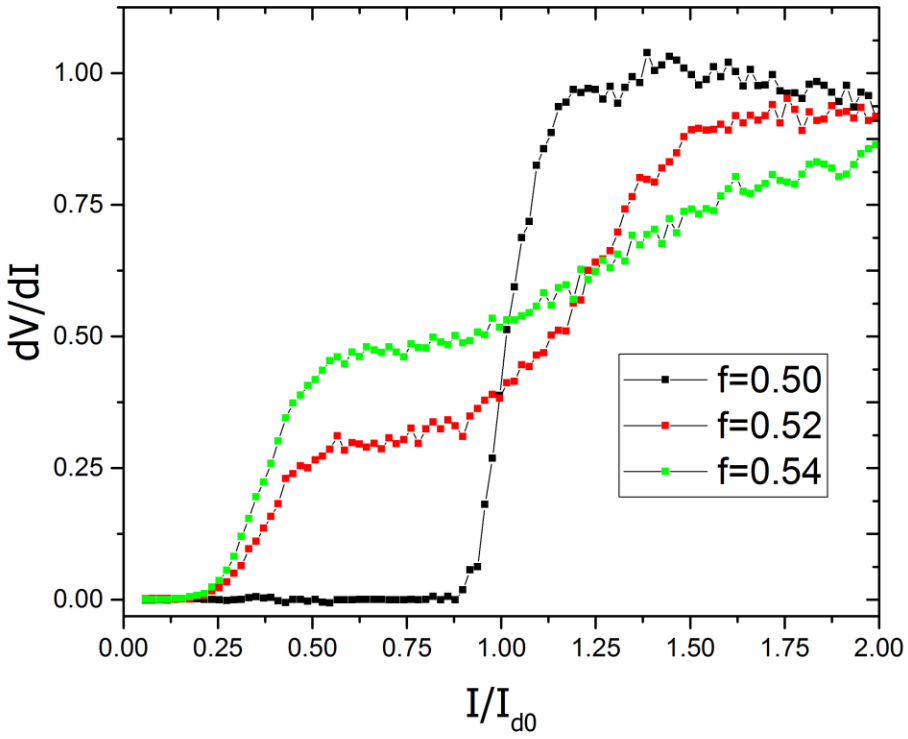

Figure 5.4. Simulated 1D d*V*/d*I* with history dependent dissipative force. The array undergoes a single transition from pinned to lattice flow for commensurate fillings. It undergoes a two step transition from pinned to defect motion to lattice flow for incommensurate fillings. The inclusion of a history dependent dissipative force removes the differential resistance peak at each step. I_{d0} is the de-pinning current for $N=1$.

5.4 Two Dimensional Simulation

We create a potential with triangular barriers as well as exclusion zones where the superconducting islands would be using the form

$$V_1(x,y)=\exp\left(-\frac{\left(\mathrm{mod}\left(\frac{x}{a}-\frac{1}{4},1\right)-\frac{1}{2}\right)^2+\left(\mathrm{mod}\left(\frac{y}{a}+\frac{\sqrt{3}}{4},\sqrt{3}\right)-\frac{\sqrt{3}}{2}\right)^2}{2\sigma^2}\right)+\exp\left(-\frac{\left(\mathrm{mod}\left(\frac{x}{a}+\frac{1}{4},1\right)-\frac{1}{2}\right)^2+\left(\mathrm{mod}\left(\frac{y}{a}-\frac{\sqrt{3}}{4},\sqrt{3}\right)-\frac{\sqrt{3}}{2}\right)^2}{2\sigma^2}\right) \quad (5.6)$$

$$V_2(x,y)=-\left|sin\left(\frac{4\pi y}{a\sqrt{3}}\right)+sin\left(\frac{2\pi}{a}\left(x+\frac{y}{\sqrt{3}}\right)\right)+\sin\left(\frac{2\pi}{a}\left(x-\frac{y}{\sqrt{3}}\right)\right)\right|^{N_{shape}} \quad (5.7)$$

$$V(x) = A\left(C_1 V_1(x,y) + C_2 V_2(x,y)\right) - F_I x \quad (5.8)$$

where $V_1(x,y)$ is an exclusion zone for islands and $V_2(x,y)$ is the vortex barrier in between islands, with C_1 and C_2 setting the relative strengths of the two potentials. The N_{shape} parameter sets the shape of the vortex barrier as shown in Figure S5(a), with $N_{shape}=1$ resulting in a broad potential well. We instead use the parameter $N_{shape}=4$ to get a narrower well. Setting $C_1=150$, $C_2=2/250$, and $\sigma=0.2$; the potential can be seen in Figure 5.5 (b) with the path the vortices move shown in white. The vortices follow a path from the center of an island triangle and cross the barrier through the center of the edge of a triangle, demonstrating that they follow the intended path.

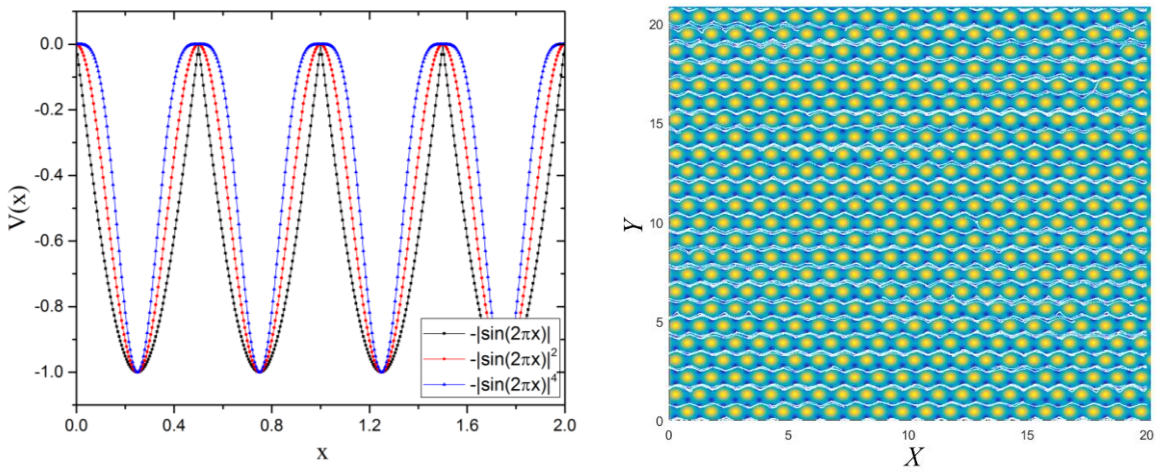

Figure 5.5. 2D Potential Well. (a) The effect of N_{shape} on periodic potential. Higher values of N_{shape} yield narrower wells for vortices to rest in. (b) The resulting periodic potential is shown with wells in blue and islands in yellow. The path of vortices in a simulated lattice is shown in white. The exclusion potential around the islands results in vortices moving between the centers of the adjacent wells, which requires overcoming the potential provided by equation 5.8.

Euler's method is once again used, only broken up into x and y components.

$$\dot{x}_i(t) = \frac{1}{\eta}\left(-\frac{\partial V\left(x_i(t), y_i(t)\right)}{\partial x_i} + \epsilon_{xi}(t) + B\sum_{j=1}^{N} \frac{\left(x_i(t) - x_j(t)\right)}{r_{ij}(t)} U_0\left(r_{ij}(t)\right) \right). \quad (5.9)$$

$$\dot{y}_i(t) = \frac{1}{\eta}\left(-\frac{\partial V\left(x_i(t), y_i(t)\right)}{\partial y_i} + \epsilon_{yi}(t) + B\sum_{j=1}^{N} \frac{\left(y_i(t) - y_j(t)\right)}{r_{ij}(t)} U_0\left(r_{ij}(t)\right) \right). \quad (5.10)$$

It is then solved by performing the following operations repeatedly with periodic boundary conditions

$$x_i(t + \Delta t) = x_i(t) + \dot{x}_i(t)\Delta t. \quad (5.11)$$

$$y_i(t + \Delta t) = y_i(t) + \dot{y}_i(t)\Delta t. \quad (5.12)$$

Where r_{ij} is the distance between vortices *i* and *j*. *N* vortices are randomly seeded into 240 wells and then slowly annealed into a low energy configuration. The results when *B/A=6* are shown in Figure 4.6 with the lattice and intermediate flow regimes shown in 4.7.

Chapter 6. Conformal Array: Non-Uniform Pinning Site Density

Vortex motion is detrimental to many applications of superconductivity, as it leads to the dissipation of energy and a finite resistance. Enhanced vortex pinning is desirable in the pursuit of higher critical currents in the presence of a magnetic field. While random pinning sites are often used[70], ordered pinning site arrays offer significantly enhanced pinning at commensurate fillings[71]. For these commensurate filling effects to be of practical use, the field range they occur over must be broadened. One way of achieving this in an SNS array is to vary the size of the triangular island plaquettes as a function of position, with the plaquettes becoming either larger or smaller in the direction of vortex motion. Since the array filling is determined by the plaquette size as well as magnetic field, the filling fraction varies as a function of position. Ideally, this would allow the formation of stripes of strongly pinned crystalline structures that serve as barriers to vortex motion, without tuning to a specific field as would be necessary for strong pinning in a uniform array.

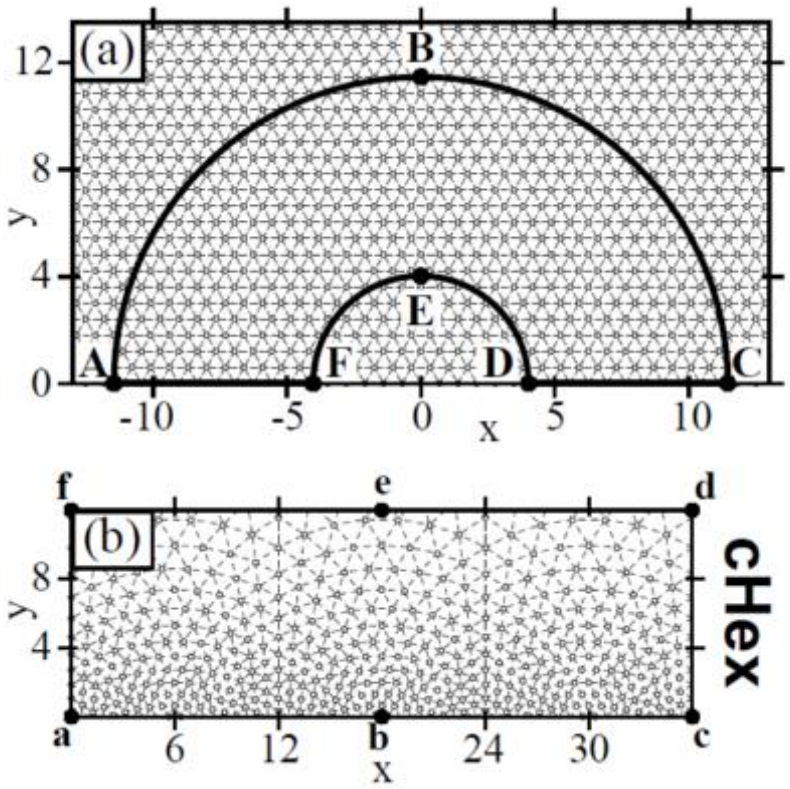

Figure 6.1. Conformal Transformation of Triangular Array The uniform array undergoes a transition mapping a disc (a) onto a square (b). The ratio between the largest and smallest triangle lattice spacings is approximately the length ratio between curve ABC and curve FED. A greater number triangle sites and a smoother change in spacings can be provided by increasing the ratio between the mean disc radius, R_{mean}, and the triangle lattice unit cell, *a*. Taken from[72].

One method, which has previously been used in artificial pinning center arrays[72,73], is to perform a conformal transformation on a triangular array and use this pattern to set the structure of the array. This is done by mapping the half disk *ABCDEF* in Figure 6.1(a) along with the contained island lattice onto the rectangle *abcdef* in Figure 6.1(b), which shows the conformally mapped array. This is attractive because it preserves the triangular structure locally, allowing a crystalline structure to form locally, but changes triangle size over a longer length scale.

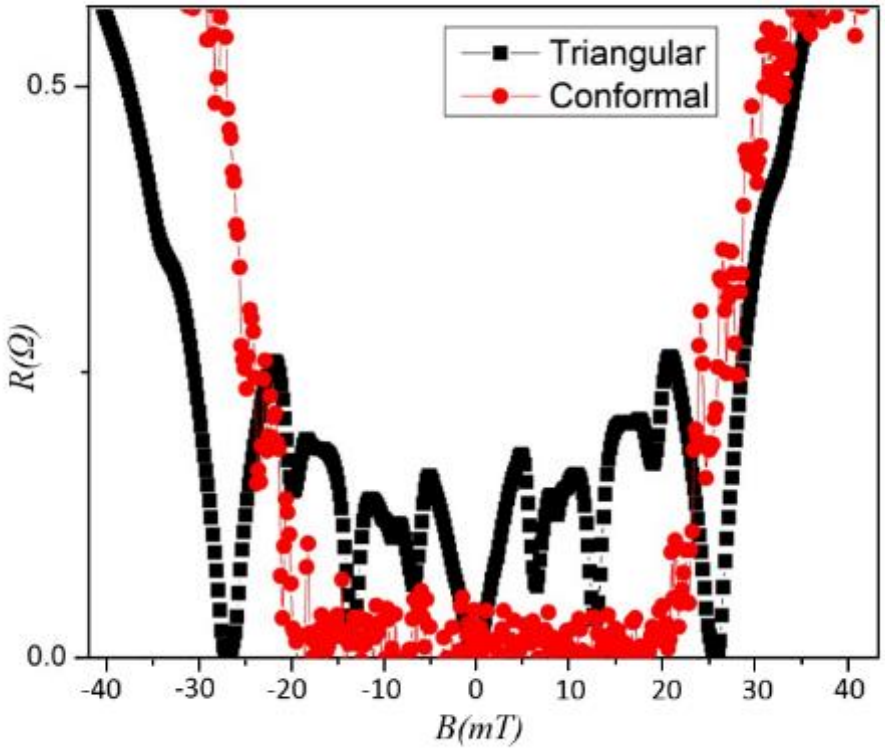

Figure 6.2. Magnetoresistance Measurements The uniform array undergoes magnetoresistance oscillations with the periodicity expected for a 500nm center to center array. The Conformal array remains in a superconducting state until the *B*-field suppresses superconductivity in the array.

We used a conformally mapped triangular array to set island centers and kept a constant edge to edge spacing between islands by varying the diameter, with the intent of providing constant coupling between islands throughout the array. This was accomplished by generating an island array script and entering it into a CAD program, which was then used for electron beam lithography with spacings between 340nm center to center and 1500nm center to center used (240nm edge to edge). This conformally mapped island array was placed on a chip with a 500nm center to center (240nm edge to edge) spaced uniform array for comparison and measured in a He_3 fridge. A comparison between the uniform array and the conformal array can be seen in Figure 6.2. The Triangular array has the expected magnetoresistance oscillations associated with

enhanced pinning at commensurate fillings, with a periodicity of 27mT. The conformal array is zero resistance until the B field suppresses superconductivity across the array.

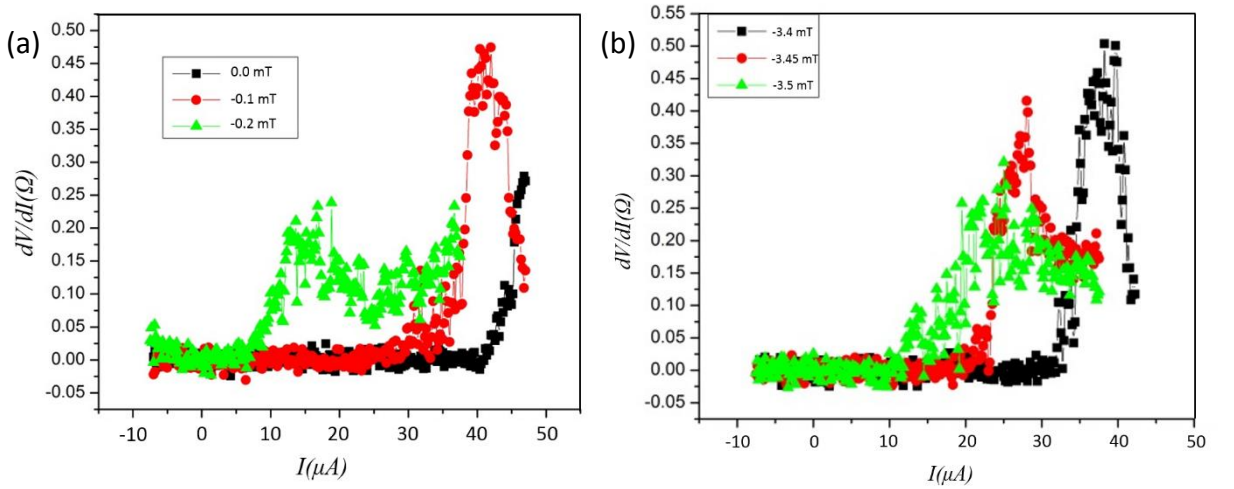

Figure 6.3. *I-V* measurements The current dependence at low B-fields around the Meissner phase (a) and higher fields when enhanced pinning occurs (b). The resistances of the flat dV/dI appear to be independent of field.

I-V measurements were performed in increments of magnetic field as shown in Figure 6.3 (a)(b), with a transition from zero resistance to finite differential resistance. Unlike the uniform array, the constant resistance of the *dV/dI* region is not proportional to the applied *B*-field. This does not necessarily mean that the array has exceeded the critical current, but could be due to the varying vortex density across the array, which could restrict vortex motion in a way that is not sensitive to magnetic field. The broad range of island spacings, however, makes this difficult to categorize and a narrower range might be sensible.

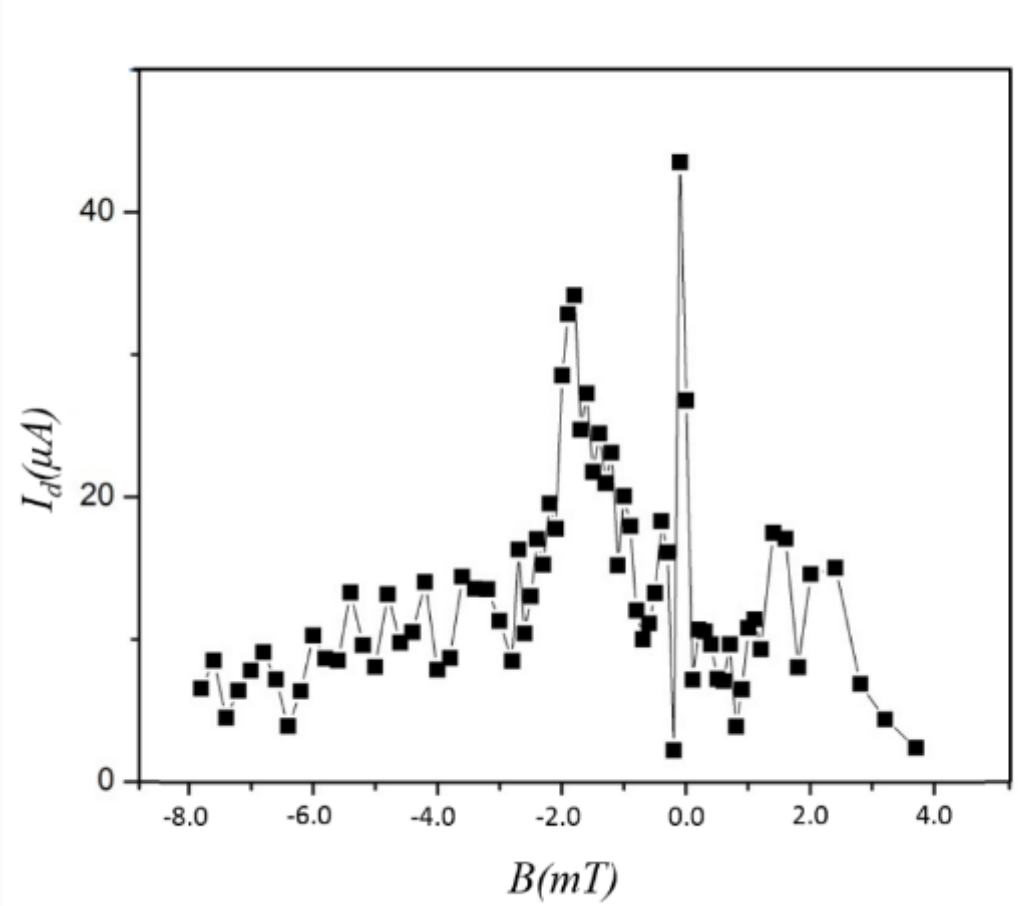

Figure 6.4. De-pinning Current of Conformal Array The conformal array has a central peak associated with a Meissner phase, a weakly pinned dilute pinning regime adjacent to the central peak, and side peaks associated with the *f=1/2* ordered phase entering the largest island triangles.

Plotting the de-pinning current as a function of *B* field shows 3 major peaks as shown in Figure 6.4. The central peak I is indicative of a Meissner regime around *B=0*, where flux is expelled from the array. When field increases, it becomes energetically favorable for vortices to populate the array, accounting for an initial drop in de-pinning current. The de-pinning current peaks to the side correspond the *f=1/2* filling of the furthest spaced island centers. This is followed by a slowly diminishing de-pinning current with *f=1/2* filling present in a closer spaced segment. The reasons for the decrease are difficult to characterize, largely due to the wide range of spacings.

To better characterize this array, the following changes are necessary on the next iteration. Increasing maximum and minimum radius for the conformal transformation would obtain a more gradual shift in density, producing broader crystalline regions. Additionally, a narrower range of center to center spacings should be used. Varying triangle area by less than a factor of 2 (spacing by less than a factor of 1.4 (e.g. 1.3)), would produce broad enhanced pinning regions and a small gap in coverage between f=1/2 and f=1 barrier regimes. This ability to turn the strong pinning on or off would demonstrate that the enhanced pinning effect is present and that it's due to stripes of crystalline vortex structures. Additionally, a large reason for doubt in the sample presented in this section is a wide variation of junction width, which was vastly different in 340nm and 1500nm center to center arrays. This width variation makes island coupling inconsistent and brings the results of this section into question. A small variation in island size would keep junction width variation on a reasonable level. A 500nm-650nm sample could produce data sufficient for a publication.

Chapter 7. Superconductor to Metal Transition in Islands and Island Arrays

Previous work by Serena Eley studying the superconductor to metal transition in Nb island arrays found novel behavior in the Nb island transition[74], with the critical temperature of Nb islands strongly dependent on island spacing. In this chapter, we further study this transition in the arrays by studying the Au thickness dependence of arrays and the diameter dependence of individual islands. We find that, while arrays of 260nm islands become superconducting between 5K and 9K, solitary 260nm Nb islands are typically not observed to superconduct above 1.5 K. This raises questions about how the presence of multiple islands, which should not yet be in a superconducting state, can stabilize superconducting order.

Establishing that this effect is not due to suppression from normal metal in section 7.1, we present single island measurements in 7.2, and perform analysis in 7.3. We find that the onset of superconductivity in our islands is strongly influenced by unusually well ordered regions, called rare regions, and that superconductivity begins in these rare regions and then spreads throughout the islands and then the array. Section 7.2 is based on work that is in the process of being published[75].

7.1 Au thickness Dependence of T_1

As shown in Figure 7.1, Nb island arrays on Au films undergo a two step transition into a superconducting state. During the first step, T_1, the Nb islands become superconducting. During the second step, T_2, the Array undergoes a BKT like transition into a superconducting state, where proximity coupling is strong enough for the islands to achieve global phase coherence of the superconducting order parameter.

T1 in our Nb island arrays exhibits an unexpected dependence on island spacing. Since island diameter (260nm) and island thickness (70nm) are considerably larger than the dirty limit superconducting coherence length of Nb ($\xi_{sc} \sim 27$nm), suppression of Island T_c from Au via inverse proximity effect should not be significant. In order to verify this, we made Au four point patterns of varying thickness and then deposited island arrays using a single Nb evaporation. We then performed *R* vs *T* measurements using a 1K pot measurement system.

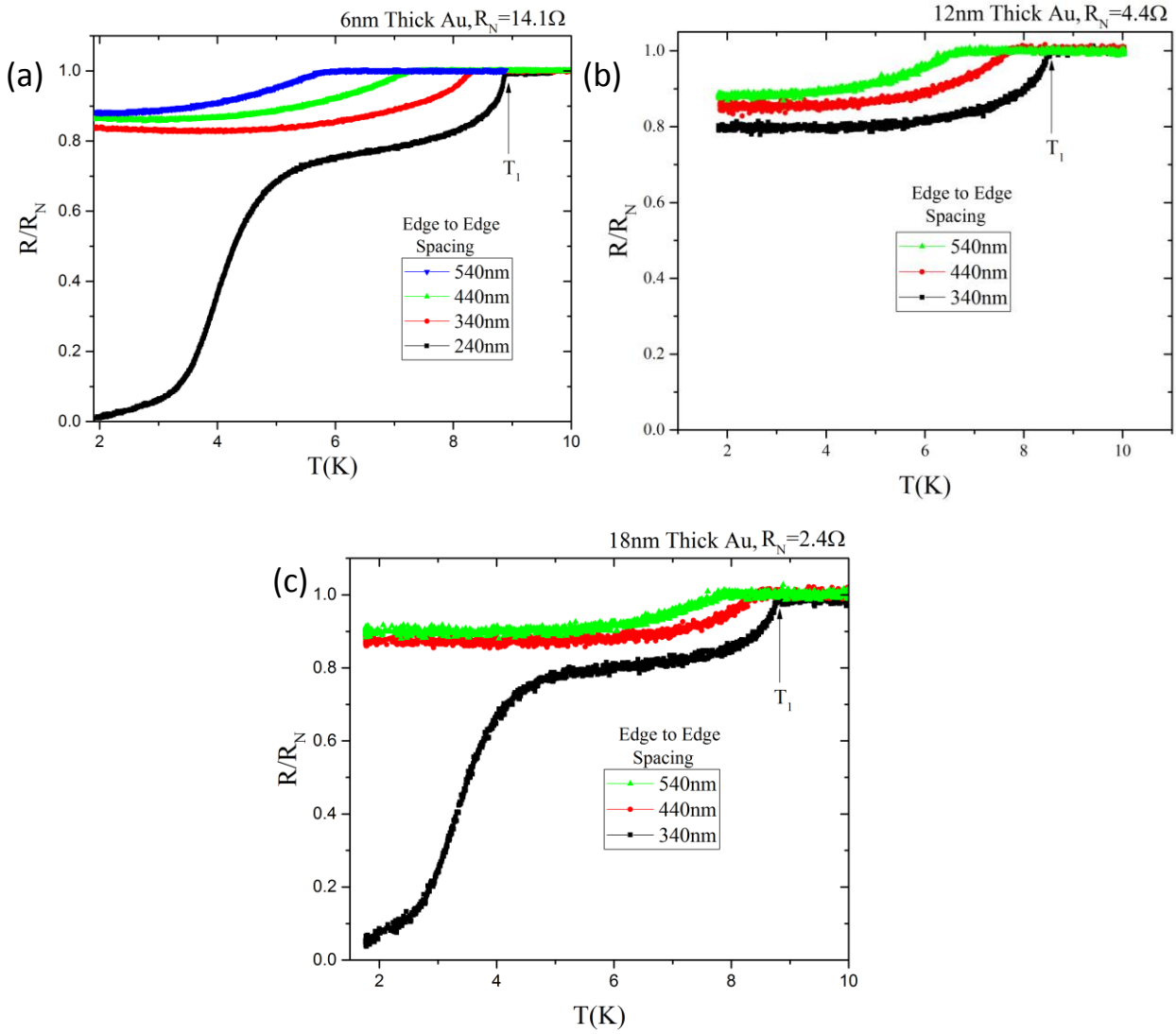

Figure 7.1. *R* vs *T* for Nb island arrays on Au. The islands are 70nm thick and 260nm in diameter. (a) Au thickness of 6nm. (b) Au thickness of 12nm. (c) Au thickness of 18nm.

The raw data from *R* vs *T* sweeps at fixed Au thickness and island spacing intervals can be seen in Figure 7.1 (a)-(c). Greater Au thickness and closer island spacing both result in higher T_1 and higher T_2. This trend can be more easily seen in Figure 7.2(a), which shows T_1 as a function of edge to edge spacing and Au thickness. Here, the arrays with the thinnest films are the most strongly dependent on spacing, while the T_1-spacing slopes of the thickest arrays are the shallowest. This leads to T_1 for the different thicknesses converging as spacing is decreased. This behavior is the opposite of what is expected for inverse proximity effect, which would result in lower temperature T_1 transition.

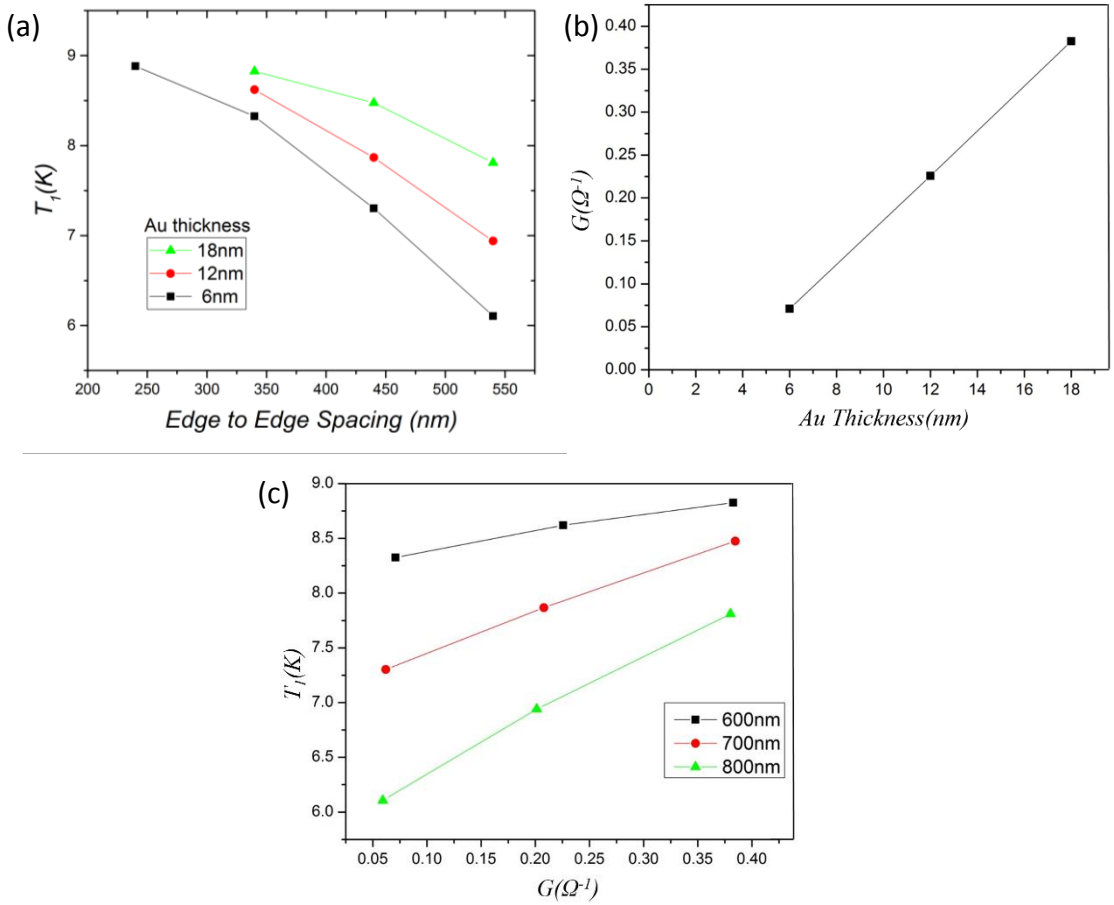

Figure 7.2. T_1 dependence on thickness, spacing, and conductance. (a) T_1 vs edge spacing for different Au thicknesses. (b) Conductance vs thickness. (c) T_1 vs Conductance at different spacings.

To better understand this behavior, we consider the conductance of the film. As shown in Figure 7.2(b), Au film conductance is linearly dependent on thickness, but extrapolates to zero conductance at a nonzero thickness of 3.3nm. This suggests that there is a surface roughness of about 3nm and that the Au film becomes discontinuous and explains why the resistance changes drastically as the value is approached. As shown in Figure 7.2(c), there is a roughly linear relationship between T_1 and conductance. This conductance and spacing dependence imply that the onset of island superconductivity throughout the array is determined by the electrical coupling between islands. While this dependence is expected during the T_2 transition, where the SNS array's phase coherence is destroyed when $k_bT_2 \sim (h/4e)I_c$ and the product I_cR_N is should be invariant for a given spacing and temperature[76], the onset of superconductivity in Nb islands was expected to be independent of this behavior.

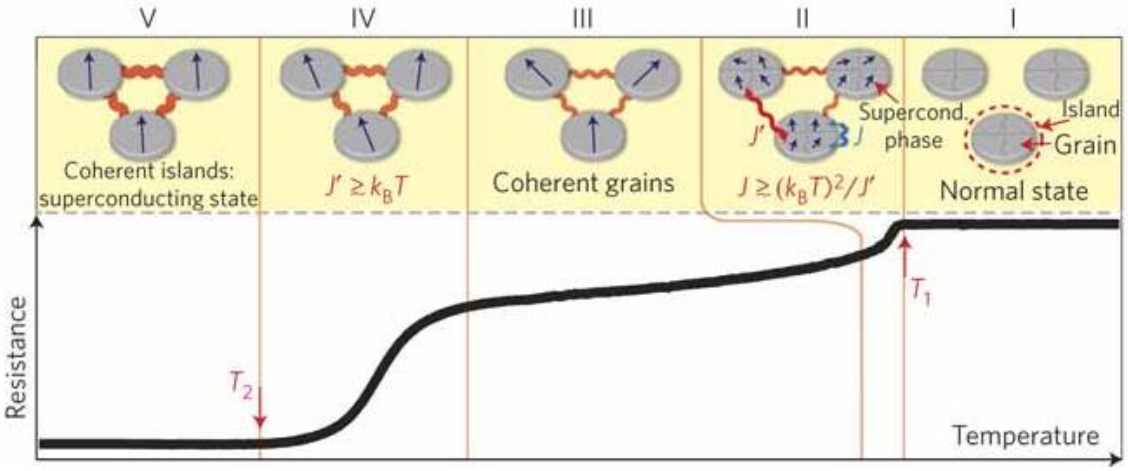

Figure 7.3. Grain Phase model incorpotating island interactions in onset of T_1. (a) The onset of superconductivity in an island is explained as phase coherence being established among all grains in an island, which occurs in region II. According to this model, both the grain interactions, *J*, and the interactions with an external, *J'*, serve to establish grain coherence in islands. Taken from [74]

This coupling dependence was noted in *Eley et al[74]*, where it was explained by giving each grain on an island its own superconducting phase. According to this model, the islands would

enter a zero resistance state when phase coherence was established across an island and the arrays would become superconducting when phase coherence spread across the array. The coupling across islands in this model was important because interactions between islands aids in stabilizing the grain phase, facilitating the onset of phase coherence in the islands as shown in Figure 7.3. However, a major issue with this model is that islands should interact weakly because they lack grain coherence. This could be solved by assuming that an unusually well-ordered island acquires grain phase coherence at higher temperatures than the others, allowing the island to interact more strongly with other islands and allow grain phase coherence to spread to other islands in a percolative fashion. This type of strongly inhomogeneous *XY* model is very similar to the rare regions ising models discussed in Section 1.2. However, this rare regions mechanism does not necessarily only apply to the phase of the superconducting order parameter. It could also apply to the amplitude and the onset of superconducting order itself.

7.2 Diameter Dependence of a Single Nb island T_c

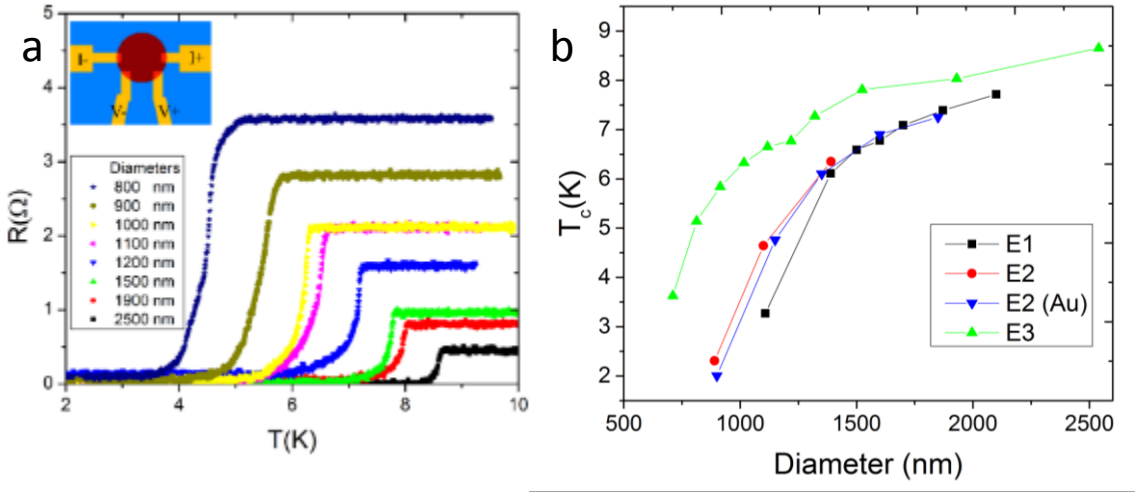

Figure 7.4. Superconducting transition for different island sizes (a) Resistance vs Temperature for various island diameters. Inset: False color optical image of island (orange) and leads (yellow). (b) T_c vs Diameter for different sets of island samples. E1, E2, and E3 denote different Nb evaporations. The blue triangles and red circles were made during the same evaporation, but the blue triangles have an underlying layer of Au, which did not significantly alter T_c.

To study the onset of superconductivity in the system, we measured the behavior of individual Nb islands deposited directly onto SiO_2 and contacted in a 4 point configuration using 10nm thick Au leads. These were then measured in a ^{4}He cryostat, sweeping temperature. Figure 7.4(a) shows a typical *R* vs *T* curves for a range of islands, with the island and the four point contact shown in the inset. The island T_c dependence on island diameter can also be seen in Figure 7.4(b), with several different Nb evaporations shown. The Nb island T_c is strongly dependent on diameter up to lengths of *1.5μm*, a much longer length scale than anticipated. Additionally, we found that 260nm Nb islands (which became superconducting at 9K when closely spaced in an array) did not superconduct above 1.5K.

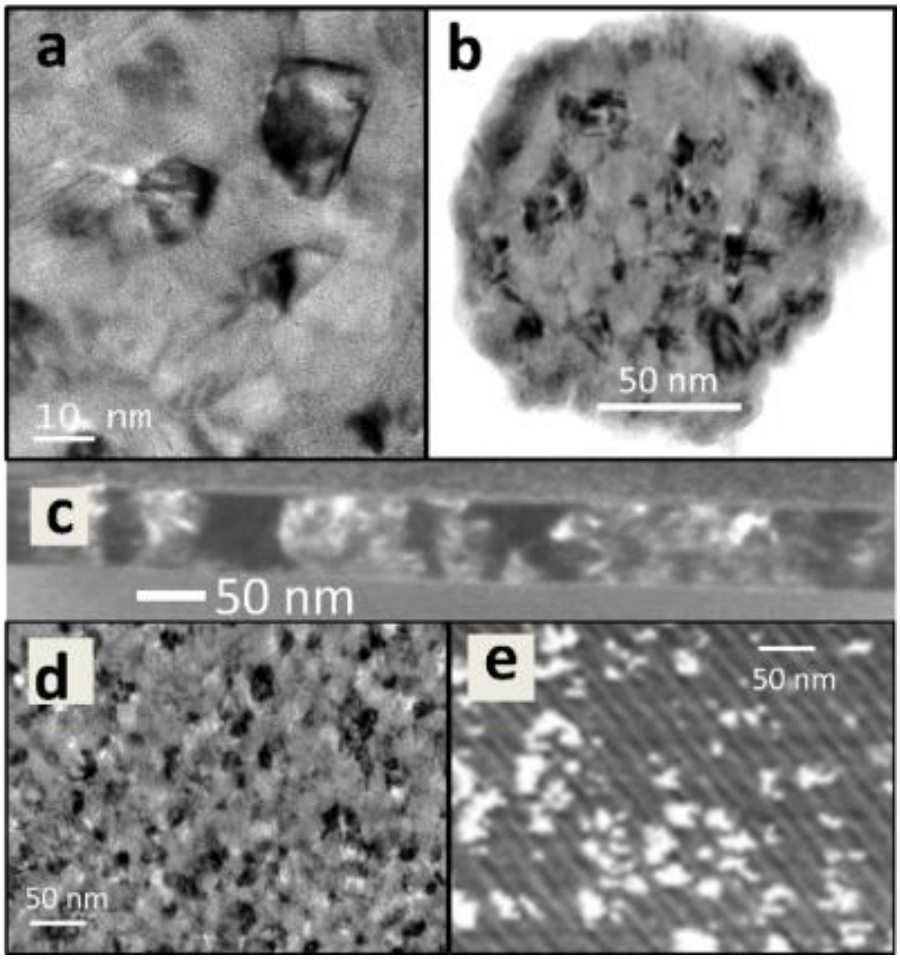

Figure 7.5. TEM and Conductive AFM. (a) Zoomed in TEM image showing crystalline Nb grains in black and amorphous-like Nb in grey. (b) TEM of a 130 nm diameter Nb island. TEM images in (a) and (b) were performed on 30 nm thick Nb. (c) Side view TEM (dark field) performed on 7 0nm thick Nb showing columnar grains. (d) TEM performed on a 2.5 μm diameter Nb island, which can be compared to (e) conductive AFM performed on 70nm thick Nb sheet. Highly conductive grains are in white (20 pA) and are separated by less conductive material shown in dark (15 pA).

Nb forms nanoscale grains when either sputtered or evaporated, with structure and grain size dependent on deposition parameters[77]. To examine if this is the cause of the diameter dependence of T_c, we perform Transmission Electron Microscopy (TEM) on islands by depositing Nb on TEM windows for a vertical image and taking an island slice for a horizontal image [78]. Figure 7.5 (a)-(d) shows typical TEM images of our Nb, where black crystals (the "grains") are surrounded by gray, amorphous-like material. Conductive Atomic Force Microscopy (CAFM)

shown in Figure 7.5 supports this, as highly conductive grains (shown in white) are observed embedded in a poorly conducting material.

Previous studies have also investigated T_c suppression in crystalline Nb grains surround by amorphous Nb having strongly suppressed superconductivity [*79*,80]. Perhaps the closest study, S. Bose et al[77], studied the T_c of magnetron sputtered Nb films as a function of average grain size, which could be controlled by altering the sputtering pressure. Bose et al. found that the Tc of Nb dropped dramatically as mean grain diameter decreased below 30nm and attributed this to suppression of superconductivity due to discretization of energy levels. In this picture, superconductivity persists even in islands that are much smaller than ξ_{sc} and superconductivity is only destroyed once the islands are sufficiently small that the discrete energy spacing of the system is larger than the superconducting gap. This condition is given by $\delta E > \Delta$ where

$$\delta E \sim \frac{2\pi^2\hbar^2}{mk_F V}, \quad (7.1)$$

is the dicrete energy level spacing where k_F is the Fermi wave vector and V is the grain volume. This criterion is valid when discussing tunneling measurements on isolated grains[81,82], but it predicts that only Nb grains smaller than *4nm*. This is completely inconsistent with the length scales measured by Bose et al, which are more consistent with the ξ_{sc} of the grains. This means that T_c in superconducting grains embedded in metal is suppressed due to inverse proximity effect, rather than discrete energy level spacing.

7.3 Onset of Island Superconductivity Via Extremal Grains

Since our islands show T_c dependence on length scales orders of magnitude larger than grain size and grain distribution remains constant as a function of diameter, the onset of

superconductivity could be determined by an extremal grains model where unusually large grains determine the onset of superconductivity. In contrast to a simple average, this would result in larger islands having higher T_c than smaller islands because they have more grains and, therefore, a higher probability of having an anomalously large, high-T_c grain. The quantitative model requires two inputs. The first is the probability distribution of grain sizes, denoted $P(L)$ where L is the diameter of a particular grain; this distribution is determined experimentally as $P(L)=\beta\ e^{(-\beta L)}$ with β=0.424nm^{-1} (see Figure 3a). The second input is the transition temperature, $T_c(L)$, which is given by[83]

$$T_c \sim T_c^0 \sqrt{L - \xi_{sc}}\ , \quad (7.2)$$

where T_c^0 is the bulk transition temperature and ξ_{SC} is the superconducting coherence length of Nb. Since this is the transition temperature of a grain embedded in a metallic matrix, formed by amorphous Nb, superconductivity occurs when the pairing energy scale Δ is greater than the Thouless energy $E_{Th} \sim \hbar D/L^2$, where D is the diffusion constant[84]. In other words, the time an electron dwells on a grain before diffusing out, $t_{Th} = \hbar/E_{Th}$, must be longer than the time is takes to form superconducting correlations, $t_\Delta = \hbar/\Delta$. Taking the standard dirty-limit $\Delta \approx \hbar D/\xi_{SC}^2$ this criterion implies that T_c is suppressed when $L \sim \xi_{SC}$ [as in Eq. (7.2)]. This mechanism is different from those found in superconducting grains embedded in insulators, where electrons do not diffuse out of the grain and T_c is only suppressed when Δ is on the order of the single-particle level spacing of the grain.

We use and object finder to obtain the grain distribtution and density from the TEM images. The Nb films have an exponential distribution of grain diameters, a mean grain radius 2.3 nm and

a small number of large grains having radii over 20 nm (Figure 7.6(a)). The approximate grain density extracted from the fit in Figure 3a is 43 grains per 100nm^2.

We can generate a set of N grains a probability distribution, P(L), that was measured from the TEM images. A typical island of diameter d has $N \sim \rho\pi d^2/4$ grains of varying sizes, where ρ is the experimentally determined grain density. The largest grain radius, L_{max}, can be extracted from the simulation, as shown in Figure 3(b). It is clear from this Figure that the probability of an island having a grain larger than the coherence length (~ 30 nm) drops dramatically below ~ 1 μm. The island T_c can then be obtained from Eq. (1) using $L=L_{max}$ and ξ_{SC} = 23 nm. The result of this simulation is shown in Figure 3(c) and fits very well to evaporations E1 and E2, which were performed using similar parameters to the TEM samples. Additionally, evaporations performed using different source conditions (E3-E6) can be horizontally scaled onto the simulation, indicating a similar trend. This provides excellent correspondence with experiment and requires no free parameters in the length scales, as they were experimentally obtained.

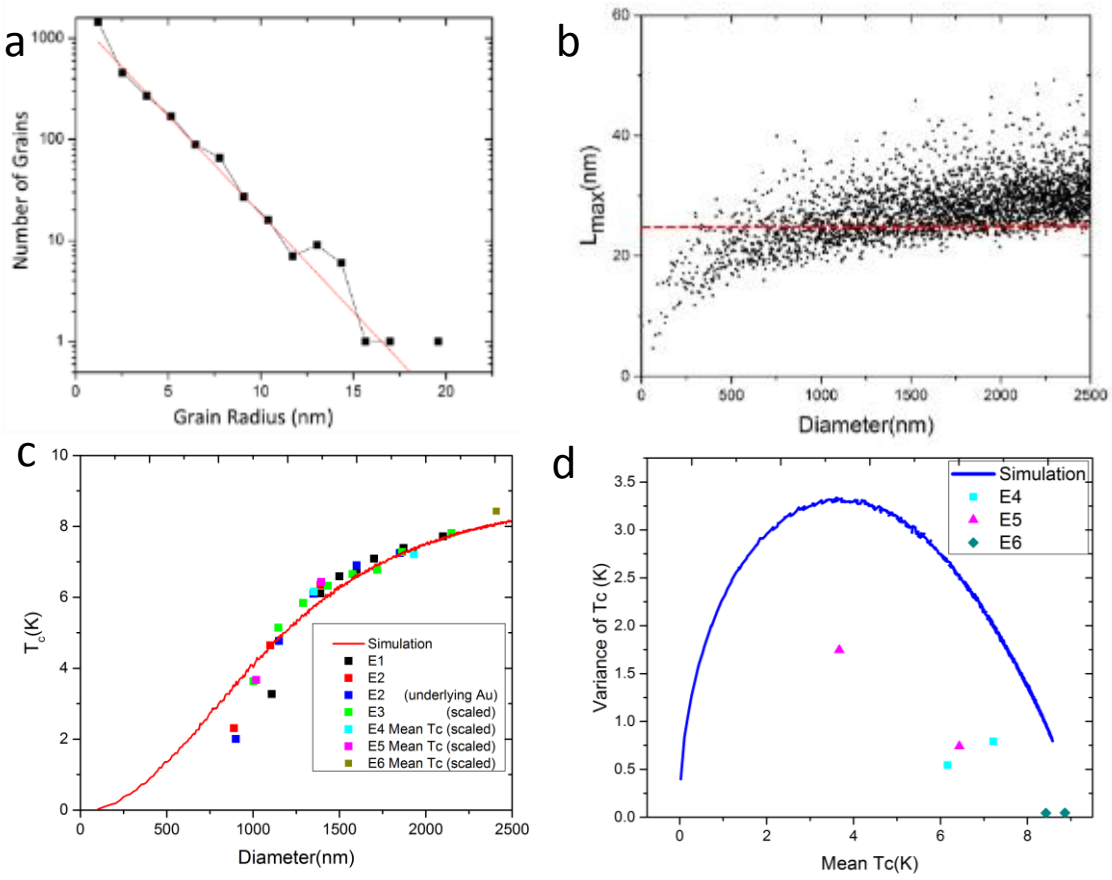

Figure 7.6. Extremal grain model (a) Grain distribution extracted from Fig.1 (d) using an object finding program. The fit shows an exponential distribution. (b) Simulated maximum grain sizes as a function of island diameter using grain distribution and density extracted from (a). The red dashed line corresponds to ξ_{SC} used in (c). (c) The simulated grain sizes are applied to EQ. 1 to obtain an estimate of T_c. Mean simulated T_c (red curve) is shown alongside data from evaporations 1 and 2 (E1 and E2), which it matches closely. Evaporations with different purities can be scaled horizontally onto the curve (E3-E6). (d) Simulated T_c variance vs mean T_c plotted against measurements. Each data point represents a value extracted from 5-10 islands of the same diameter.

The extremal-grain model predicts not only the size-dependence of the typical transition temperature, but also a variance in T_c among islands of the same diameter. While the probability distribution of L_{max} for islands of fixed diameter is predicted to follow a Gumbel distribution[85,86], which is not sensitive to d, fluctuations of T_c are sensitive to d, due to the varying slope of Eq. (1). Large fluctuations in T_c occur when the mean value of L_{max} is on the order of ξ_{SC}, while $L_{max} > \xi_{SC}$ leads to minimal fluctuations in T_c, as most islands have at least one grain that goes superconducting near the bulk transition temperature. We experimentally observe both large T_c

fluctuations for islands of the same diameter, and a trend of increasing fluctuations with decreased diameter, as shown in Figure 3(d). The simulation of expected fluctuations is shown on the same plot, and show similar trends for simulation and theory.

While the extremal grain model agrees with experiment, it is important to rule out alternative explanations, particularly because the island normal resistance, R_N, also scales with T_c (Figure 2a). We first consider the role of shunting resistance and normal metal suppression from the contacts by measuring Nb islands having underlying Au films, which provide a high conductance shunt across the island and greater normal metal suppression. As can be seen in the blue curve of Figure 2b, the T_cs of islands with underlying Au were similar to those of islands without underlying Au, indicating that neither suppression from normal metal contacts nor shunting resistance significantly altered T_c. Another concern is that the structure of the islands might depend on diameter, changing both T_c and R_N. This is inconsistent with both TEM observations, which demonstrate that grain size distribution does not vary significantly with island diameter (see Supplement), and with measurements performed on small diameter island arrays coupled with underlying Au[74], which suggest that T_c is determined by the total volume of coupled Nb. The dependence of island resistance on diameter can be best explained by transport through a highly granular material, where most of the current passes through the most conducting paths. Since fewer of these highly conductive paths are available for small diameter islands, both the mean value and the variation in R_N is greater for smaller diameter islands. This trend is discussed and modeled in the Supplement. While this may seem to imply that the application of a percolative model of superconductivity is relevant to our system, the islands discussed in this manuscript are orders of magnitude more conductive than the films previously studied with the percolative model and exhibit a completely different finite size trend for T_c [see appendix B].

Our results suggest a physical picture of the local nature of the superconducting state near the superconductor-metal transition: this state is inhomogeneous and is dominated by rare regions, as suggested in Refs. (83,87). By exploring mesoscopic systems, we have directly quantified the influence of rare regions on superconducting transport. We have found, remarkably, that even when grains are coupled strongly enough that the normal-state resistance is small, the superconducting transition can be captured via a model of effectively decoupled "grains." In this sense, our mesoscopic superconducting islands behave like many other strongly random quantum systems, such as high-temperature superconductors[88,89].

Chapter 8. Sn Island Arrays on Graphene

In this section, we present work developing superconducting island arrays on graphene. Work in other groups has demonstrated a superconducting state[90] and a direct superconductor to insulator transition on granular superconductors deposited directly on graphene[91]. Weak magnetoresistance oscillations in graphene[92] and a superconductor to insulator transition without a scaling analysis[93] have also been demonstrated for ordered superconducting islands on graphene. In this section, we demonstrate a superconducting state and associated magnetoresistance oscillations in Sn island arrays on graphene. We then demonstrate a transition from an insulating state to one with a very weak supercurrent in a Sn array on graphene with underlying hexa-Boron Nitride (h-BN), along with magnetoresistance oscillations consistent with mesoscopic interference.

Future technical goals for this project are to observe SIT scaling consistent with a quantum phase transition in an Sn island array. Once this is accomplished, the arrays could be designed to have stable rare regions to smear the transition or to have a rare regions of critical size to study a Griffiths singularity, both of which are discussed in section 1.2.

8.1 Sample Fabrication

A schematic of a gate tunable graphene SNS array is shown in Figure 8.1. Graphene is initially transferred onto a 300nm SiO_2 substrate, etched into a 4 point pattern using reactive ion etching (RIE), and contacted using Ti/Au normal leads. An array of superconducting islands is then added in the form of 100nm diameter Sn islands with 300nm center to center spacing. To supply a back gate, an additional electrical contact is made to the Si below the SiO2 substrate and

a voltage is applied to it. The details of the fabrication process, as well as design considerations and process development issues, is discussed below.

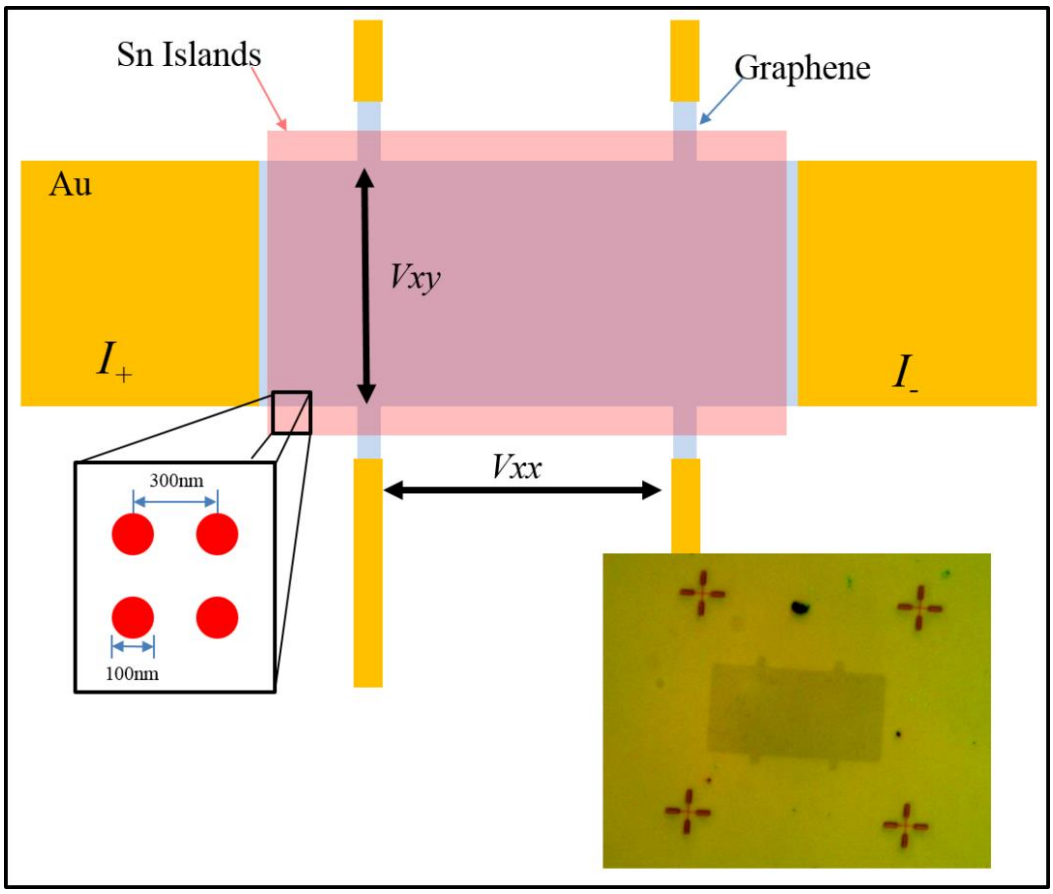

Figure 8.1. Layout of a hall bar Graphene SNS Array. A graphene sheet (shown in blue) is contacted with Au pads in a hall bar configuration. An array of SN islands (shown as a transparent pink rectangle) is then placed on top of the graphene array. Measurements are performed by passing current between the leads marked I_+ and I_-. Standard four point measurements are performed by reading out V_{xx}. Hall measurements are performed by reading out V_{xy}. Inset shows a hall bar patterned piece of graphene surrounded by alignment marks prior to being contacted with Au leads.

A 300nm SiO_2 substrate is standard in graphene samples, allowing single and double layer graphene to be visible optically via interference[94] from reflected light. Additionally, the 300nm SiO_2 layer is thin enough to allow electrical control over carrier density in graphene by applying a voltage to the underlying Si and using the SiO_2 as the dielectric of a capacitor, with graphene on one side and Si on the other. Wedge bonding, which is necessary to connect the sample to the chip

carrier, to a 300nm SiO_2 substrate requires careful settings to avoid punching through. These settings can be optimized using a sacrificial SiO_2 chip prior to making attempts on a real sample.

There are two types of graphene transfer methods that are available to us: exfoliated graphene and chemical vapor deposition (CVD) grown graphene. Exfoliated graphene involves separating layers of graphite using tape. Once sufficiently thin flakes are obtained, the carbon is transferred to the wafer by pressing the tape onto the 300nm SiO2 substrate, rubbing the tape with a thumb, and peeling away the tape. The chip is then searched and mapped using a microscope, identifying large single layer pieces. This has the advantage of producing higher quality graphene than CVD grown graphene, but did not produce enough large graphene pieces for this project. Instead, we switched to CVD grown graphene, where graphene is grown on a copper substrate. The copper is then dissolved and the CVD graphene is transferred onto the SiO2, covering most of the chip. A lithography process then defines the graphene into a hall bar configuration and an RIE process (using mostly O2) removes the excess graphene.

Two lithography steps are then used to contact the graphene with normal leads and then place a superconducting island array on top. The first process involves putting a layer of PMMA (950 A4, 4000 rpm) on the substrate, placing alignment marks using e-beam lithography in the approximate location of the graphene, developing the marks, and mapping the location of the graphene with respect to the marks optically. After aligning to the marks (which are visible optically and via SEM once developed), the contacts are drawn via e-beam lithography and developed. After a brief mill, the a sticking layer of 1nm Ti is placed before depositing Au and performing a liftoff process to remove excess material. The Chip is then coated with PMMA again (3 layers of 495 A2 and 1 top layer of 950 A2) and the islands are defined by e-beam lithography.

30 nm of Sn are deposited and excess materials are once again removed in acetone via a liftoff process.

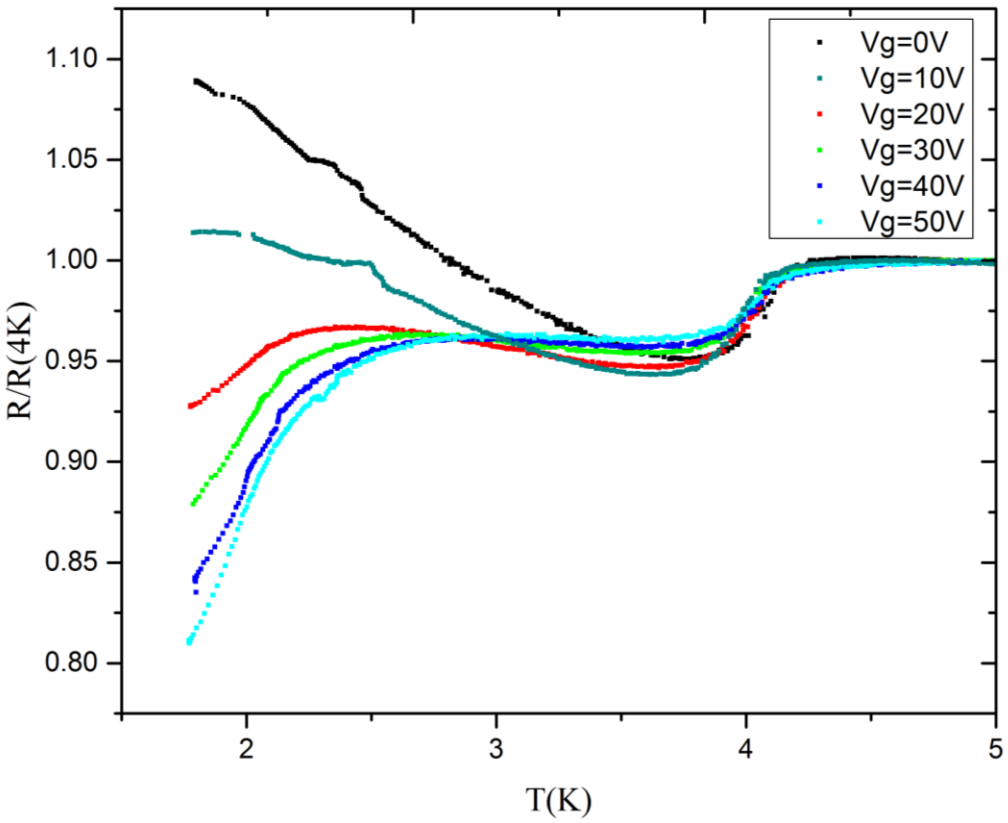

Figure 8.2. Onset of Superconductivity in Sn island array on graphene. *R* vs *T* measurements in 1K system. Sn islands become superconducting at around 4 K. As temperature is decreased, *R* increases near Dirac point and decreases at values away from the Dirac point. This demonstrate coupling between Sn islands.

Sn is chosen because it wets to graphene, making a good interface and allowing islands to interact via proximity effect, with the onset of superconductivity in island arrays shown in Figure 8.2. Sn is deposited at room temperature in a thermal evaporator. Limiting factors include low critical magnetic field and a tendency to form puddles. Attempts to form a uniform film by cooling the substrate to 77K during evaporation failed to get coupling between islands. Prior to using Sn, we attempted to use evaporated Nb and Nb with a Ti sticking layer. While these have been used for superconducting contacts on graphene[95] and have a high critical field (4T), we have been

unsuccessful in getting islands of this type to interface with graphene and did not observe a superconducting transition. Sn is deposited at room temperature in a thermal evaporation system.

8.2 Sample Measurement

Graphene samples were measured in an Oxford Triton dilution refrigerator using the 4 point measurement setup described in chapter 2 and hall measurements were performed as shown in Figure 8.1. Differential resistance measurements can be performed adding a 17Hz 40nA AC signal to a DC signal using a sum box and varying the DC current, carrier density in the graphene can be controlled by applying a voltage to the underlying silicon, and magnetic field can be applied using a vector magnet.

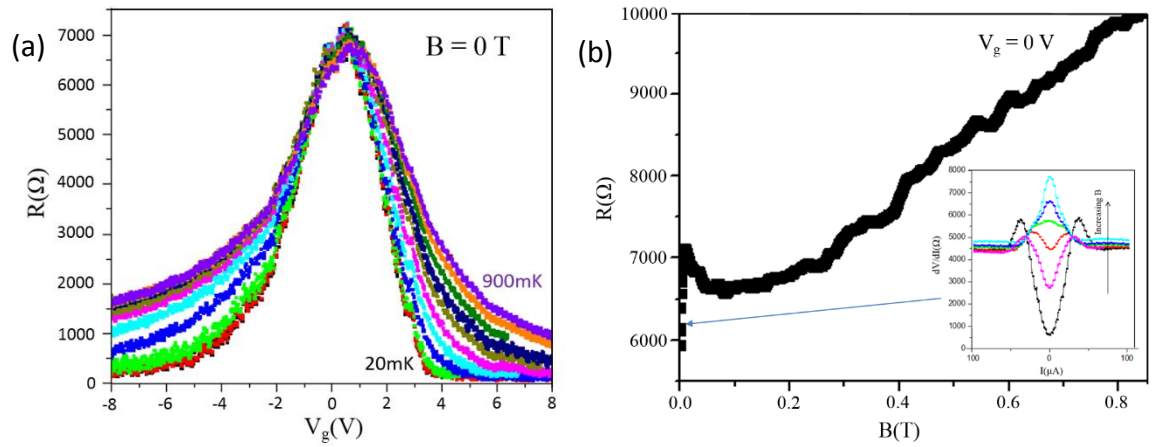

Figure 8.3. Resistance measurements of Graphene array. (a) R vs V_g at different temperature when B = 0 T. Resistance increases as temperature increases and there is no crossover to insulating transition. (b) A dip associated with superconductivity occurs around $B = 0\ T$, followed by a peak at B = 0.007T. The inset shows dV/dI as a function of current as B is shifted from $B = 0T$ to $B = 0.007T$ at V_g=0, transitioning from a superconducting to insulating state.

Preliminary R vs V_g sweeps were performed at different temperatures at B=0, as shown in Figure 8.3(a). While the array could be gated into a superconducting state, the resistance remained too low to do achieve a crossover into insulating behavior even near Dirac point, as resistance continues to increase with temperature. The B dependence or R is shown in Figure 8.3(b) at V_g=0,

showing the onset of array superconductivity at low fields, a spike in resistance, and then normal state behavior at higher fields. As shown in Figure 8.4 (a) and Figure 8.4(b), a weak crossover can be achieved by shifting *B* field to the value of the magnetoresistance peak in Figure 3(b), but it is not strong enough to do a scaling analysis. In order to get a more resistive dirac point and study the superconductor-insulator transition, damaging the graphene or using a hexa-boron nitride (H-BN) substrate will be necessary.

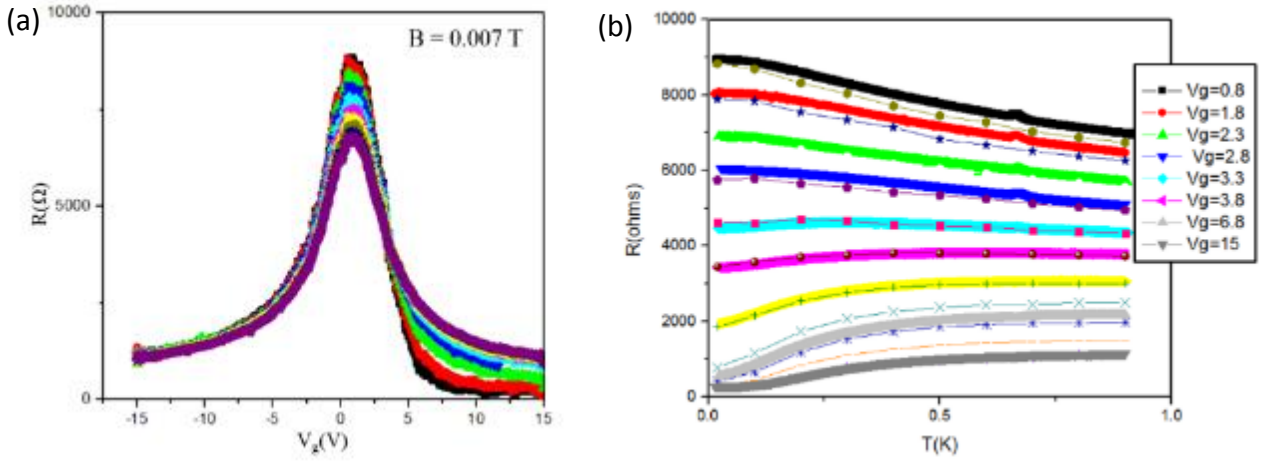

Figure 8.4. Layout of a hall bar Graphene SNS Array. (a) R vs V_g at different temperature when B = 0.007 T. Insulating behavior is visible near Dirac point and superconducting behavior is visible at large V_g. A crossover is visible at V_g=*3.5 V*. (b) *R* vs *T* at B=0.007T at set V_g shows a crossover from superconducting to insulating regimes.

Setting the gate away from the Dirac point, we observed magnetoresistance oscillations in *R* vs *B* sweeps as shown in Figure 8.5 at V_g=25. While this is suggestive of superconducting vortex effects, differential resistance measurements shown in Figure 8.6 (a-b) lack important signatures of vortex motion such as a flux flow regime with resistance linearly increasing with *B* field. Combined with much less pronounced de-pinning current peaks at commensurate fillings and the rapid suppression of superconductivity with increasing *B* field, this makes the magneto resistance

oscillations difficult to characterize. Indeed, similar studies have been able to extract only limited information in a similar regime [92].

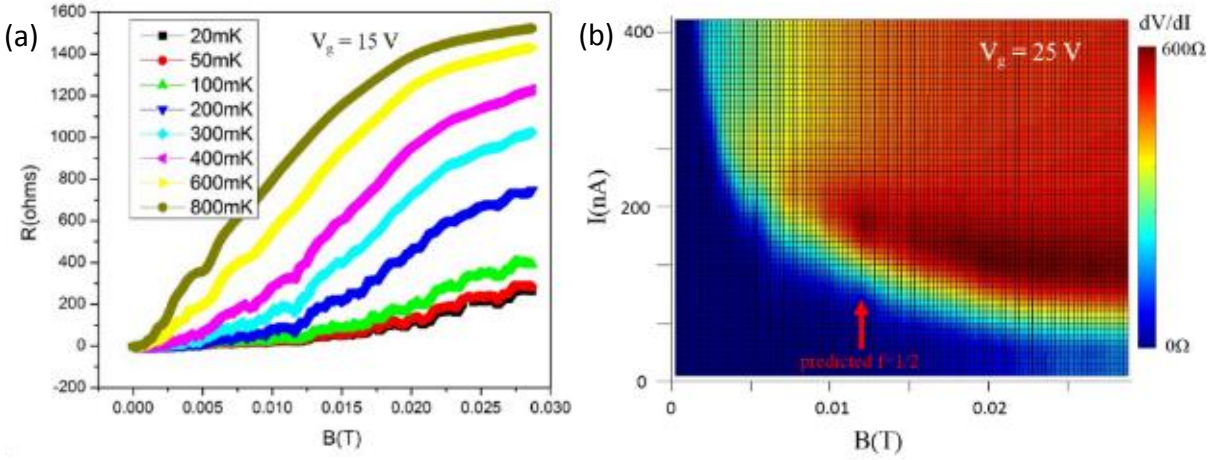

Figure 8.5. Magnetoresistance Oscillations and IV analysis. (a) Magnetoresistance measurements are shown at different temperatures for V_g=15V. (b) A 2D plot of dV/dI vs I and B. A small increase in de-pinning current is visible when *f~1/2*.

Hall measurements were performed by sweeping magnetic field at different values of V_g. Due to the resistance of graphene being much larger than the hall resistance at the fields in question, a small misalignment in the hall leads or a small inhomogeneity can lead to a contributing signal that is symmetric around B=0 (a hall signal should be symmetric as a function of B around *B=0.*). Removing the asymmetric component by subtracting R_{xy}(-B) and R_{xy}(-B), we plot the hall resistance in Figure 8.6 (a). The slope of R_{xy} vs B as a function of V_g is shown in Figure 8.6(b), with a crossover from hole to electron carriers at V_g=1.5V. The extracted carrier density is shown in the inset. Due to inhomogeneities (e.g. due to charge inhomogeneities endemic to SiO_2), there is a coexistence of hole carrier regions and electron carrier regions near the dirac point. The can be seen in the gradual crossover from negative to positive in Figure 8.6(b) or the divergence near *n=0* in Figure 8.6(b) inset.

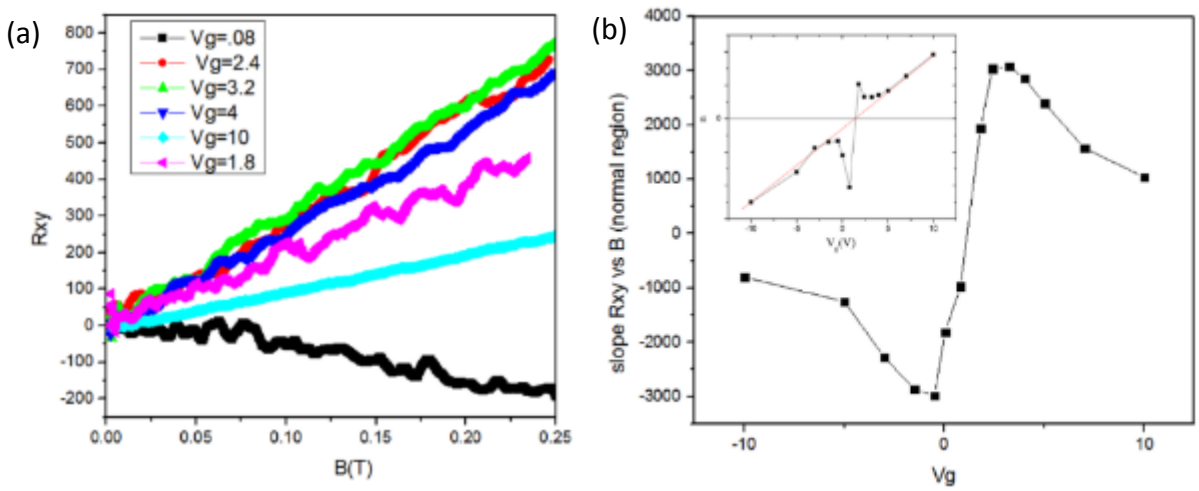

Figure 8.6. Hall bar measurements on Graphene SNS Array. (a) R_{xy} with symmetric component removed for various V_g. (b) The slope of R_{xy} in (a) as a function of V_g. A crossover from hole to electron carriers occurs at V_g=1.5V. Inset shows the extracted carrier density. Divergence near n=0 is due to coexistence of regions of holes and electrons near the Dirac point due to inhomogeneities.

8.3 h-BN Graphene

While it is tempting to view our system as a model 2 degree electron gas (2DEG) coupled to superconducting islands, the actual mobility of graphene placed on SiO_2 is significantly worse than that of the GaAs typically used in 2DEG studies. Surface roughness, charge inhomogeneities, and impurities all contribute to adding disorder into graphene on SiO2, resulting in diffusive transport[96] and limiting the minimum carrier density near the Dirac point[97]. Due to the limitations posed by an SiO_2 substrate, many of the early studies of ballistic transport in graphene were performed on suspended graphene[98]. More recently, high mobility has been obtained by using hexaboron nitride(h-BN) as a substrate or by sandwiching graphene between h-BN layers. These samples approach the quality of traditional 2DEGs, with behaviors like the fractional hall effect being demonstrated in both suspended[99] and h-BN[100]. Whereas traditional semiconductor 2DEGs are extremely difficult to couple to superconductors, superconducting contacts have been demonstrated on h-BN sandwiched graphene using MoGe[101,102]. This

provides a new area of physics that has only been recently explored, with interesting competition between hall and superconducting states that could lead to an experimental realization of Majorana fermions[103] and have applications in quantum information. The immediate technical goals in our use of h-BN, however, are much more conservative and are primarily concerned with obtaining a lower carrier density near the Dirac point. This would result in a broader range of accessible resistances.

While cantilever processes similar to those used in the h-BN sandwiched graphene experiment are being developed in our group, obtaining h-BN graphene comparable to those used in the hall effect studies is a difficult technical problem. A simpler process involving directly exfoliated h-BN on SiO_2 followed by a liquid transfer of CVD grown graphene on top, while still a relatively dirty 2D material, could provide an improvement over graphene on SiO_2. A key problem with our system is that charge inhomogeneities in the SiO_2 prevents the graphene from being gated uniformly towards the Dirac point, creating puddles with either electrons or holes as carriers. A more stable dielectric could solve this and provide a higher resistance near the Dirac point, allowing the sample to be gate tuned to the superconducting transition.

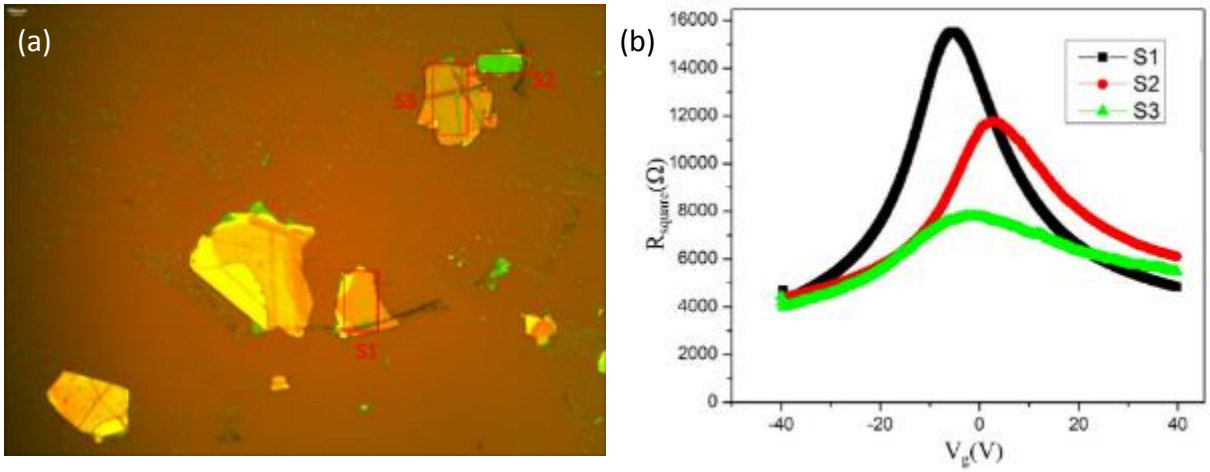

Figure 8.7. h-BN Graphene Room Temperature Measurements. (a) Exfoliated h-BN with graphene transferred on top. Graphene squares (S1-3) marked in red are then defined by lithography and RIE before being contacted.(b) *R* vs V_g sweeps are performed on S1-3. S3, the thickest and most disordered square, is low resistance at the Dirac point and is the flattest curve. S1 and S2 are on flatter and thinner pieces of graphene, resulting sharper and more resistive Dirac peaks. This is due to less disorder and greater capacitance.

We performed a direct transfer of h-BN onto SiO2 using scotch tape exfoliation. A sheet of CVD grown graphene was then transferred on top and the chip was annealed at 200C in hydrogen and argon. 4 point patterns on top of h-BN were defined with e-beam lithography and excess graphene was cut away using reactive ion etching. A preliminary sample of graphene on h-BN is shown in Figure 8.7 with room temperature measurements performed shown in the inset. The image is dirty looking, because the CVD graphene growth process had problems at the time and was no longer producing continuous films. It is difficult to tell if the more resistive graphene, as seen in the inset, was due to the use of an h-BN substrate or the more disordered graphene sheet. This increase in resistance, however, was desirable for achieving a transition to an insulating state. Another chip was contacted with normal leads and Sn islands as discussed at the start of this chapter.

8.4 h-BN graphene Sn Island Array Measurements

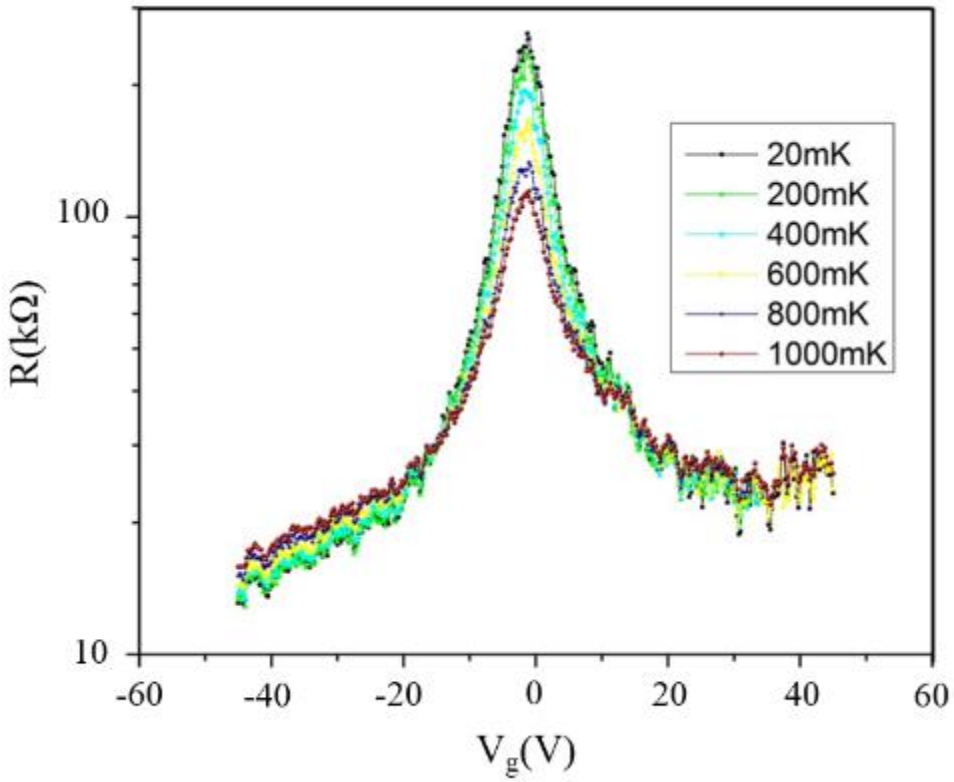

Figure 8.8. R vs Vg of h-BN Graphene covered in superconducting islands. The Dirac peak is observed around V_g=0. Here resistance increasing as temperature is decreased, indicative of insulating behavior, and the resistance is much higher than the sample directly on SiO_2. A crossover appears at V_g=-15, with values below this decreasing in resistance as temperature drops.

h-BN graphene was measured in a Triton dilution refrigerator. Figure 8.8 shows R vs V_g at various temperatures. The array is in the insulating regime near the Dirac point, with resistance increasing as temperature decreases. A crossover towards a superconducting state can be seen at V_g=*-15V* and the resistance decreases with decreasing temperature beneath this vale. Figure 8.9 Shows resistance vs temperature for a range of V_g. Here, the array resistance increases dramatically as temperature is decreased near the Dirac point and falls slightly as temperature is decreased away from the Dirac point, showing only a weak supercurrent. Thus, the h-BN graphene island array is much more strongly in the insulating regime than the Graphene island array directly on SiO_2, but does not have the same access to superconducting behavior.

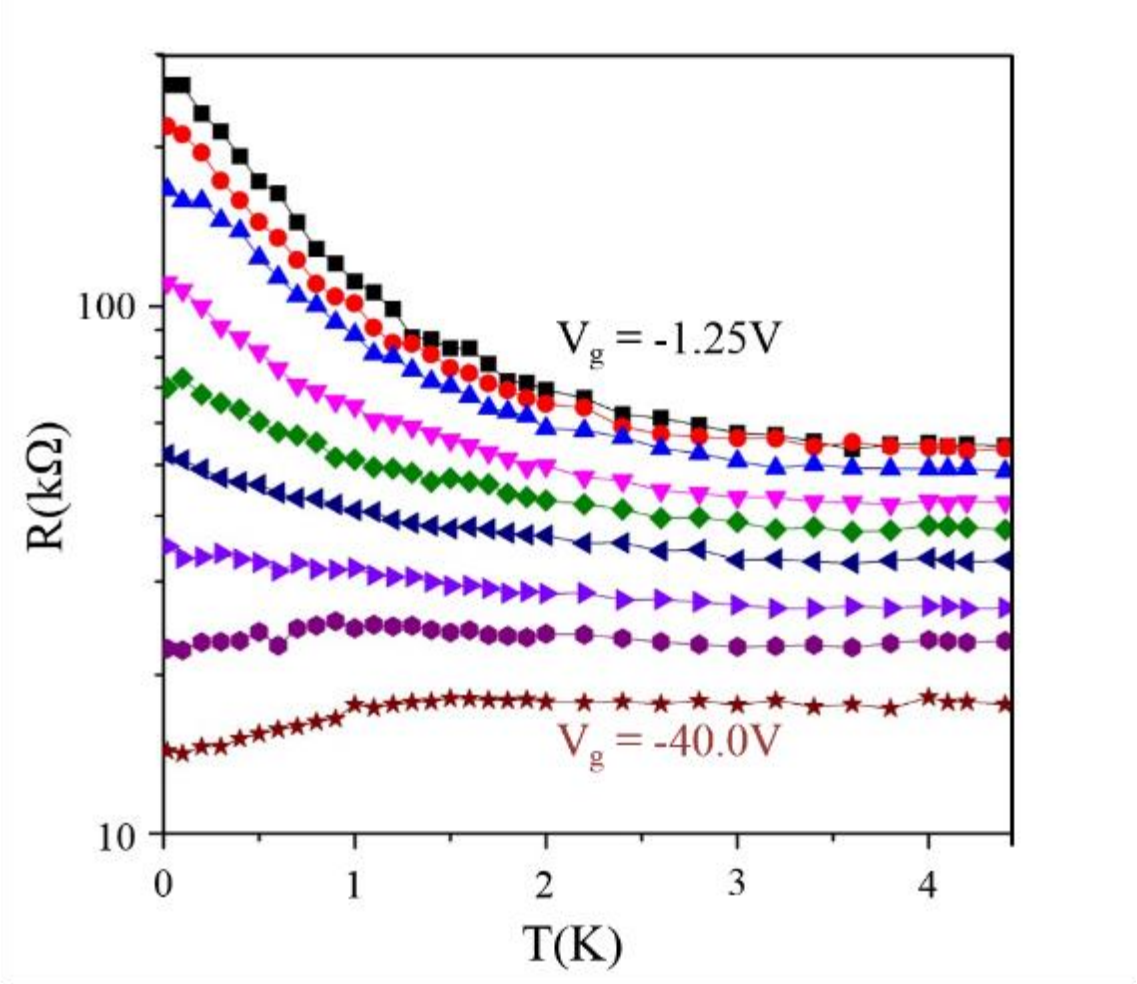

Figure 8.9. R vs T of h-BN Graphene covered in superconducting islands. The array shows a transition from insulating behavior near the Dirac point towards weak superconductivity at V_g*=-40V*. While the system never reaches an *R= 0 Ω*, the presence of a supercurrent is visible as a decrease in resistance as temperature decreases. Also, the onset of superconductivity in the Sn islands is visible at V_g*=-40V* as a jump in resistance at *4K*.

The array can be studied by performing current biased differential resistance measurements at different gate voltages, shown in Figure 8.10. At V_g near the dirac point, there is a sharp peak in d*V*/d*I* around *I*=0 before d*V*/d*I* flattens out as a function of current. At V_g=-40V, there is a broader dip in d*V*/d*I* around *I*=0 that is likely associated with the presence of a supercurrent, which is suppressed as I is increased. At intermediate values of V_g, the sharp central peak and the broader dip are both visible. This coexistence is not consistent with a transition from a superconductor to a bose-insulator and, combined with the weakness of superconductivity in the sample and the large

amount of inhomogeneous disorder in the sample, could mean that the two are unrelated phenomena. For example, the central d*V*/d*I* peak could be a purely normal state effect, which could be tested by applying a magnetic field greater than H_c of Sn.

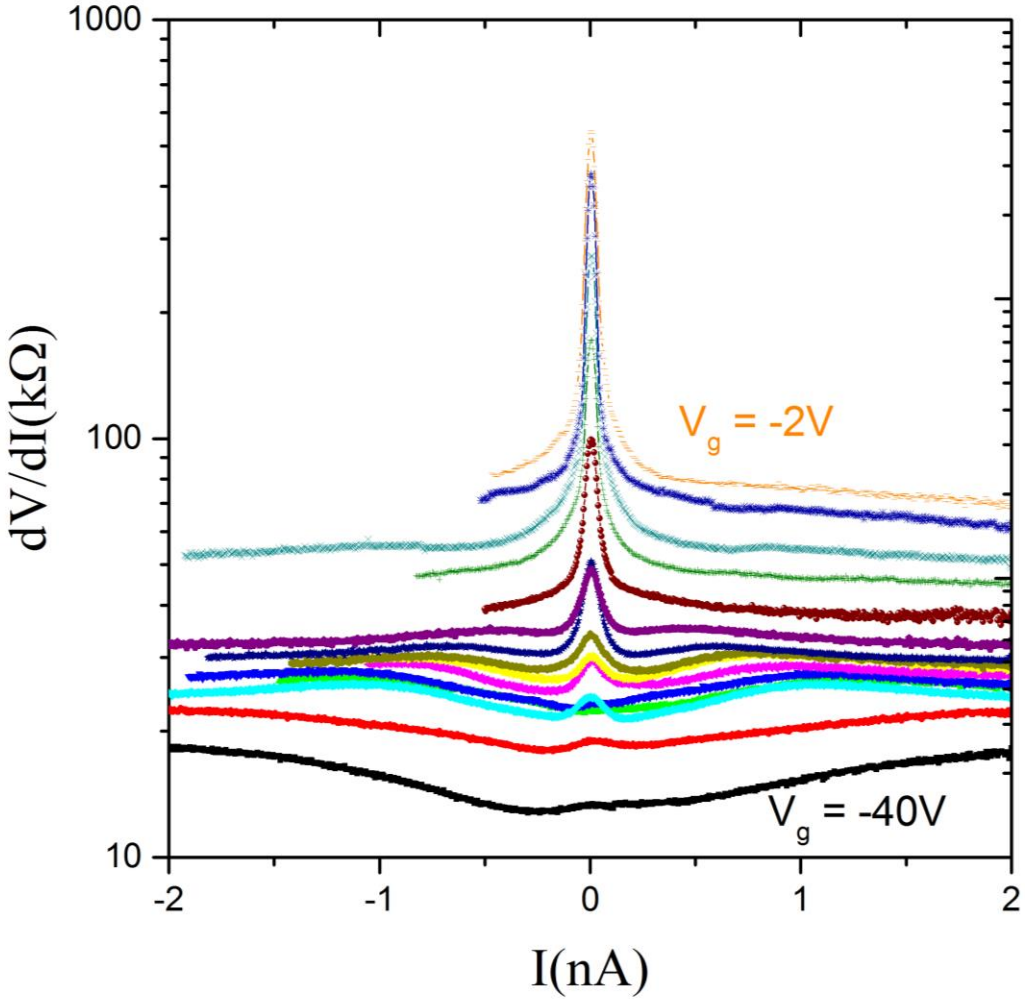

Figure 8.10. Differential resistance measurements. Differential resistance measurements show a sharp d*V*/d*I* peak at *I*=0 near the Dirac point and a much broader dip in d*V*/d*I* at *I*=0 away from the Dirac point. The peak and the dip are visible together at intermediate values of V_g.

To study the insulating behavior, we perform a voltage biased differential conductance measurement, applying a DC voltage bias summed with an AC measurement voltage and reading out the AC current response. This type of measurement can resolve features like gaps in density

of states, which could not be resolved in current biased measurements (which would only appear as a sharp dV/dI peak, much like the one in Figure 8.10). As shown in Figure 8.11, we observe a gap around V=0, within which conduction approaches 0. The width of this gap is extracted and plotted as a function of V_g in the inset, with the maximum value at the Dirac point and decreasing linearly as V_g is shifted away from the Dirac point. This is not a coulomb blockade diamond, as it doesn't repeat itself periodically, but can be explained by the formation of a bandgap in graphene. While pristine graphene should be gapless, strain and superlattice effects have been demonstrated to result in a gap. Due to disorder in the graphene, the underlayer of h-BN, and the periodic array of islands on top, there are too many variables to say exactly what is happening.

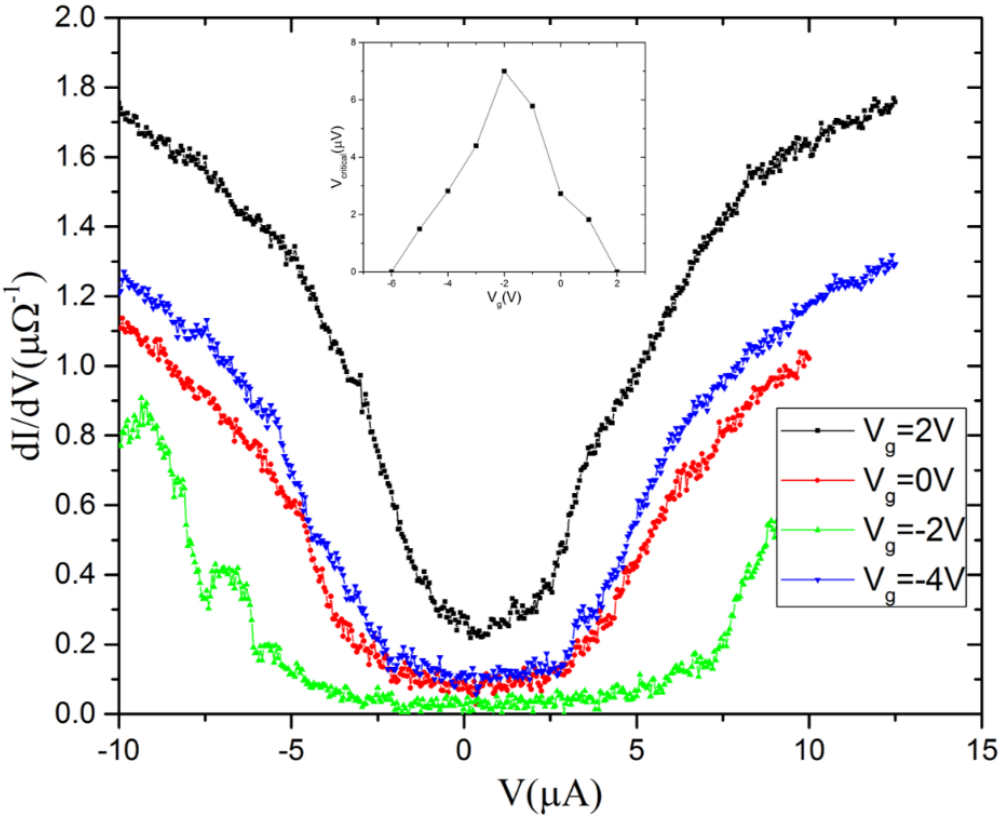

Figure 8.11. Differential conduction measurements. Differential resistance measurements show a gap where conduction approaches 0. The width of this gap is shown in the inset and is greatest near the Dirac point, linearly decreasing with gate voltage as it is shifted from this value.

To further characterize array behavior, we performed *R* vs *B* measurements at the Dirac point, shown in Figure 8.12. Since the fields in question are much larger than the critical field of Sn, the oscillations are not related to superconductivity. One possible explanation is that the oscillations are due to interference effects from the periodic Sn islands. If the islands create a boundary between the graphene underneath the island and the outlying graphene, the flux through the island will determine how the different paths interfere, similar to the Aharanov-Bohm effect. These mesoscopic interference effects around the islands should have a periodicity of 0.130 T and the relevant quantum of flux values are marked by blue dashed lines, corresponding to peaks in resistance.

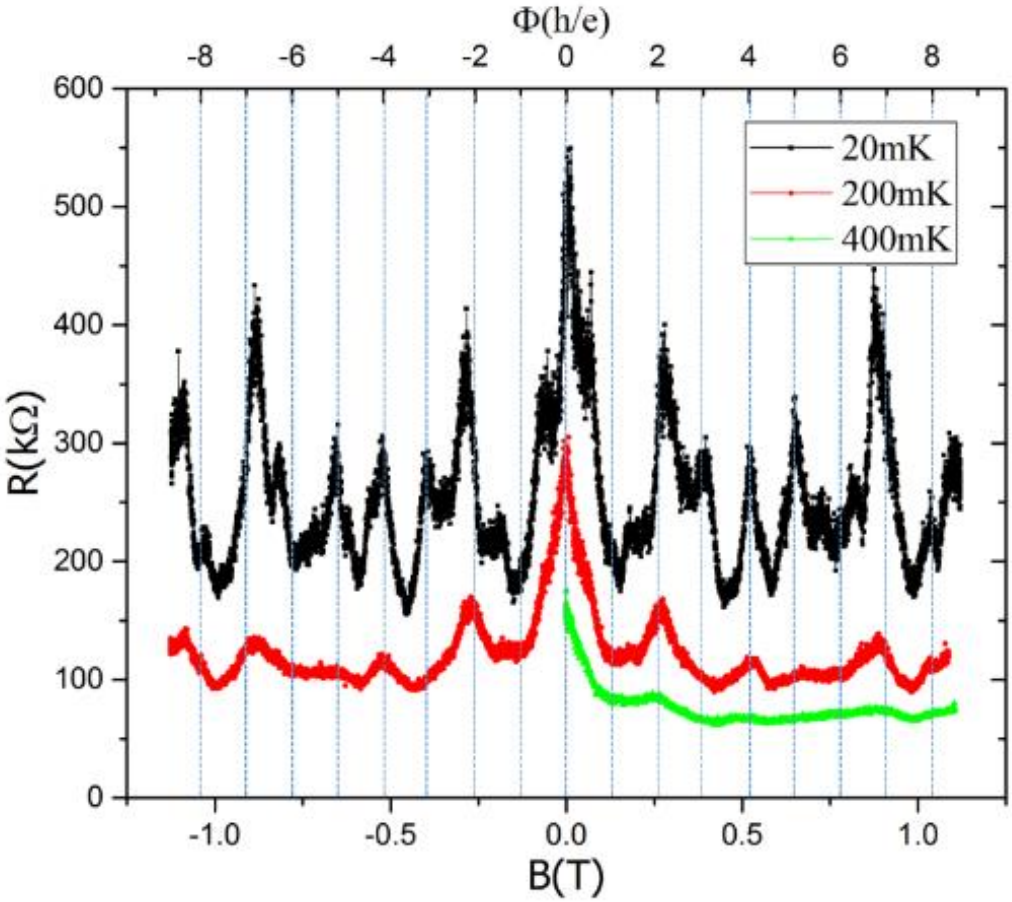

Figure 8.12. Magnetoresistance oscillations. *R* vs *B* measurements at the Dirac point show resistance peaks that are repeatable at different temperatures. The top scale shows the flux going through an Sn island as a function of the normal quantum of flux (*h/e*).

Interpreting the results from the initial h-BN sample is difficult due to uncertainty in the quality of graphene and the transfer onto h-BN. While some of the behavior, such as the magnetoresistance, can be explained, the array is too disordered to get a clear signature. In order to characterize the array behavior, future work will require higher quality graphene and a more controlled transfer onto h-BN. This work will be performed by other graduate students in the future.

Chapter 9. Conclusion

In this thesis, we have presented work on superconducting vortex dynamics, the superconductor-metal transition, and the superconductor to insulator transition. We studied anomalous vortex dynamics in Chapter 3 and have performed a detailed study of collective vortex motion in Chapters 4-5. We have also presented evidence for the rare region onset of superconductivity in Nb islands and island arrays in chapter 7 as well as the development of Sn on Graphene arrays for studying the superconductor to insulator transition in chapter 8.

Future work on this project will be performed by Vincent Humbert and Rita Garrido-Menacho. Possible vortex projects include conformal arrays like the one studied in chapter 6, which could be easily implemented in a narrower range of spacings, or with the addition of point disorder in the lattice. Additional work with the superconductor to insulator transition will involve the further development of superconducting island arrays on graphene using an h-BN substrate, with higher field superconductors such as MoGe and NbTiN available for testing in the Quantum cluster evaporator. Additionally, our group has experience working with topological insulators, making a superconducting island array on one a possibility.

Appendix A: Numerically Solving Stochastic Differential Equations

Euler's method provides a convenient way to get approximate numerical solutions to stochastic differential equations (SDE) and is used for almost all dynamic vortex simulations in this thesis. Euler's method is analogous to deduced (or "dead") reckoning navigation, where a ship's position is plotted based on starting position and velocity rather than relative position to identifiable landmarks. In Euler's method, there is a known starting point and subsequent points are calculated based on some heading every timestep, Δt. Provided that Δt is sufficiently small, this method provides an accurate solution. The example of overdamped and underdamped molecular vortex models is shown below.

The underdamped molecular vortex model's analogous heading term is $\ddot{x}_i(t)$. The repeated calculations are as follows (if integral is confusing, replace the integral with simplest case, $\eta\dot{x}_i(\tau)$):

1. $$\ddot{x}_i(t) = \frac{1}{m}\left(-\frac{\partial V(x_i(t))}{\partial x_i} - \int_0^t \chi(t-\tau)\dot{x}_i(\tau)d\tau + \epsilon_i(t) + \sum_{j=1}^{N} U\left(\frac{x_i(t)-x_j(t)}{L_{int}}\right)\right).$$

2. $$\dot{x}_i(t+\Delta t) = \dot{x}_i(t) + \ddot{x}_i(t)\Delta t.$$

3. $$x_i(t+\Delta t) = x_i(t) + \dot{x}_i(t)\Delta t.$$

The solution is performed repeatedly. Initial conditions for $x_i(t)$ and $\dot{x}_i(t)$ are important. We typically assume that the lattice is starting from a pinned position, with vortices arranged in a low energy configuration. $x_i(t_0)$ is found by annealing the lattice starting from high temperature to low

temperature, which is accomplished by obtaining $\epsilon_i(t)$ using a random number generator with an exponential distribution of the form $\exp\left(-\frac{|\epsilon_i(t)|}{kT}\right)$, where *Y* is the output and *T* is temperature. In the above section, which is single vortex physics, this is just a vortex resting at the bottom of a potential well. $\dot{x}_i(t_0) = 0$ to approximate a pinned system. If initial velocity is nonzero, this might yield a different solution (*I-V* of underdamped is hysteretic).

A.1 Overdamped Instantaneous Dilute Limit (non-interacting):

1. $\dot{x}_i(t) = \frac{1}{\eta}\left(-\frac{\partial V(x_i(t))}{\partial x_i} + \epsilon_i(t)\right).$

2. $x_i(t+\Delta t) = x_i(t) + \dot{x}_i(t)\Delta t.$

Changing the dissipation term, η, effectively changes the time step, Δt (it is so dominant, it does not change the solution). Initial condition $x_i(t)$ also does not affect form of solution. Yields *I-V* behavior described by EQ 2.

A.2 Overdamped History Dependent (Exponential Decay) Dilute limit.

1. $\dot{x}_i(t) = \frac{1}{\eta_1}\left(-\frac{\partial V(x_i(t))}{\partial x_i} - \frac{\eta_2}{\tau_\beta}\int_0^{t-\Delta t} e^{-t/\tau_\beta}\,\dot{x}_i(\tau)\,d\tau + \epsilon_i(t)\right).$

2. $x_i(t+\Delta t) = x_i(t) + \dot{x}_i(t)\Delta t.$

Once again, η_1 is just a way of adjusting Δt. As discussed previously, the relevant parameter is τ_β compared to the time taken for a vortex to cross an array.

Appendix B: Percolative Network Simulations

B.1 Random Resistor Network Simulations

The diameter dependence of the resistance can be largely explained by transport dominated by percolative paths in an inhomogeneous film. Percolative behavior has been previously of interest in the study of doped semiconductors[104,105] and has been studied using random square resistor networks[106]. Tuning the probability of a connection between adjacent nodes existing, p, and a connection not existing, $1-p$, the random network studies observe a phase transition at a critical probability, p_c, from finite sized clusters exist for $p<p_c$ to an infinite cluster of linked nodes throughout the network for $p > p_c$. The relevant length scale involved is the correlation length, $\xi \propto |p-pc|^{-\alpha}$, where α is a scaling constant. This corresponds to the radius of the largest percolative clusters for $p < p_c$ and the radius of the largest holes in the infinite percolative cluster in $p > p_c$.

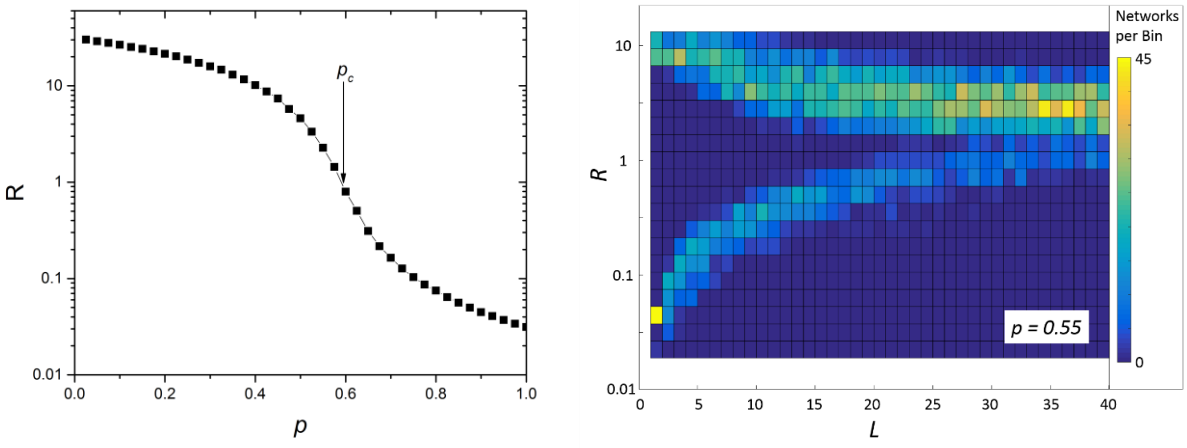

Figure B.1. Resistor Network Simulations (a) The resistance of a random resistor model with a probability, p, of there being a low resistance connection rather that a high resistance connection. (b) A histogram of resistance as a function of a square array's width, L. The islands split into two groupings with increasing L, one with lower resistance that's spanned by a low resistance network and another that's split by a hole in the network. The two groupings are equal in number near pc, but the higher resistance grouping is dominant for $p>p_c$ and the lower resistance grouping dominates $p<p_c$.

Our system corresponds more closely to the case of a good conductor in a poor conductor, which can be studied by giving the open links a large but finite resistance[107]. The resistance of this can be seen in Figure B.1 (a), with a crossover of $p_c \sim 0.6$. Sample resistance is dominated by weak links between network clusters for $p < p_c$ and conductance through a single network cluster for $p > p_c$. The finite size behavior of this model results in either a network cluster spanning the array or a hole in a network cluster dividing the array. This leads to array resistance distribution splitting as the array width, L, decreases. This splitting is shown on a logarithmic scale in Figure B.1(b) at $p=0.55$. Due to proximity with p_c, the upper and lower curves are approximately equal in magnitude, but the lower curve is suppressed for $p<p_c$ and the upper curve is suppressed for $p>p_c$. Since we observe increasing resistance with decreasing island diameters, our data corresponds to the $p<p_c$ case involving weakly linked networks clusters.

The relevant length scale of this system is the spacing of key current paths, which corresponds to the size of a low resistance network cluster, ξ. These clusters do not necessarily correspond to a single grain, which would yield finite size effects on the scale of tens of nanometers. Instead, the networks could correspond to clusters of Islands, as inhomogeneities in grain density exist on the scale of hundreds of on nanometers and may explain the large increase in resistance below 700nm.

B.2 Percolative Network Model of Tc

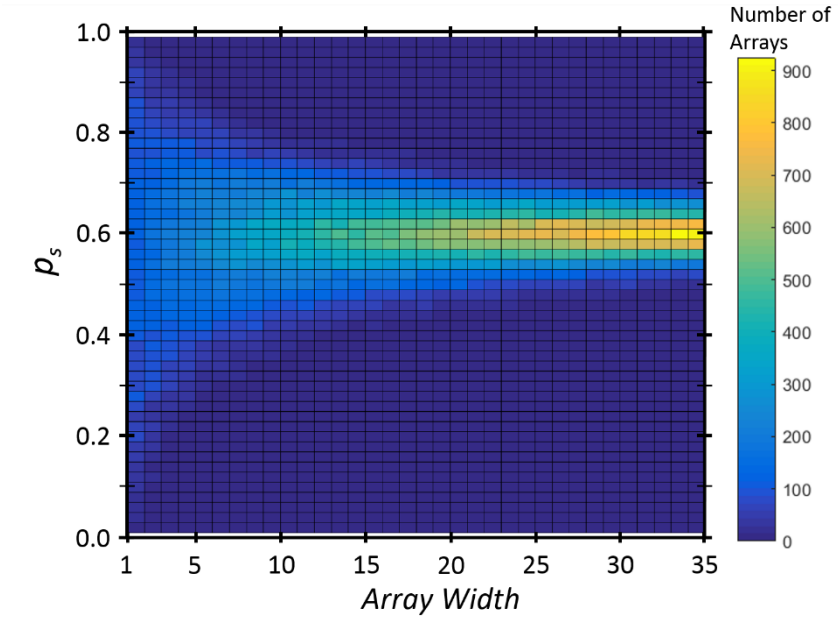

Figure B.2. Percolative Superconducting Network Model Simulation The distribution of p_s for random square arrays as a function of width. For large arrays, $p_s \sim p_c$. Decreasing array width broadens the distribution.

Granular superconducting films have been previously modeled as percolative networks, where a linked network spanning the film results in superconductivity. In this model, adjacent grains are weakly coupled and interact via the Josephson effect, with links is broken when $kT >> E_J$ (k is the Boltzmann constant, T is the temperature, and E_J is the Josephson energy)[108]. If the junction strength is assumed to be random, then the probability, p, of links being connected is a function of T. Figure B.2 shows the distribution of p_s, the smallest value of p that will result in a linked network spanning an array, for different square array sizes. For large arrays, $p_s \sim p_c$, where the network size approaches infinity. For small arrays, there is a broad distribution of p_s. This occurs because an array of size comparable to the characteristic network length could be spanned by a network for $p<p_c$ or split by a hole in the network for $p>p_c$. Thus, this model predicts that a constrained system of grains, like the Nb islands, should have a distribution of T_c that includes values that are lower and higher than the large granular film T_c. This Tc distribution is expected to

broaden as island size decreases, with increasing numbers of islands having T_c approaching $9K$ or $0K$. This is inconsistent with the T_c trend presented in this paper, which only finds a trend towards lower Tc as island size is decreased.

References

[1] S. R. Foltyn et al. *Nat. Mater*. **6**, 631 (2007).

[2] T. Klein, I. Joumard, S. Blachard, J. Marcus, R. Cubitt, T. Giamarchi, P. Le Dousal, *Nature* **413**,404 (2001).

[3] K.Harada, O. Kamimura, H. Kasai, T. Matsuda, A. Tonomura, V. V.Moshchalkov, *Science* **274**, 1167(1996).

[4] T. A. Kontorova, Y. Frenkel, *Zh. Eksp. Teor. Fiz.* **8**, 89, (1938).

[5] S. N. Coppersmith, D. S. Fisher, *Phys. Rev. B* **28**, 2566 (1983).

[6] K. Shinjo and M. Hirano, *Surf. Sci.* **283**, 473 (1993).

[7] E. Abrahams, P. W. Anderson, D. C. Licciardello, T. V. Ramakrishnan, *Phys. Rev. Lett.* **42**, 673 (1979).

[8] M. P. A. Fisher, *Phys. Rev. Lett.* **65** 923 (1990).

[9] H. M. Jaeger, D. B. Haviland, B. G. Orr, A. M. Goldman, *Phys. Rev. B* **40**, 182(1989).

[10] J. N. Rjabinin, L. W. Shubnikov, *Nature* **135**, 581 (1935).

[11] V. L. Ginzburg, L. D. Landau, *JETP* **20**, 1064 (1950).

[12] A. A. Abrikosov, *Sov. Phys. JETP* **5**, 1174 (1957).

[13] W. H. Kleiner, L. M. Roth, and S. H. Autler, *Phys. Rev.* **133**, A1226 (1964).

[14] H. F. Hess, R. B. Robinson, R. C. Dynes, J. M. Valles J. V. Waszczak, *Phys. Rev. Lett*. **62**, 214 (1989).

[15] R. Wordenweber, P. H. Kes, C. C. Tsuei, *Phys. Rev. B* **33**,3172 (1986).

[16] S. Bhattacharya, M. J. Higgins, *Phys. Rev. Lett.* **70**, 2617 (1993).

[17] E. Zeldov, D. Majer, M. Koncykowski, V. B. Geshkenbein, V. M. Vinokur, H. Shtrikman, *Nature* **375**, 373 (1995).

[18] Y. Paltiel, E. Zeldov, Y. N. Myasoedov H. Shtrikman, S. Battacharya, M. J. Higgins, Z. L. Xiao, E. Y. Andrei, P. L. Gammel, and D. J. Bishop, *Nature* **403,** 398 (2000).

[19] Y. Fasano, M. Menghini, F. de la cruz, Y. Paltiel, Y. Myasoedov, E. Zeldov, M. J. Higgins, S. Bhattacharya, *Phys. Rev. B* **66**, 020512(R)(2002).

[20] F. Bedard, H. Meissner, *Phys. Rev.* **101**, 26 (1956).

[21] H. Meissner, *Phys. Rev.* **109**, 686 (1958).

[22] H. Meissner, *Phys. Rev.* **117**, 672 (1960).

[23] P. G. de Gennes, *Rev. Mod. Phys*. **36**, 225 (1964).

[24] M. S. Rzchowski, S. P. Benz, M. Tinkham, and C. J. Lobb, *Phys. Rev. B* **42**, 2041. (1990).

[25] S. P. Benz, M. S. Rzchowski, M. Tinkham, C. J. Lob, *Phys. Rev. B* **42**,6165 (1990).

[26] C. D. Chen, P. Delsing, D. B. Haviland, Y. Harada, and T. Claeson, *Phys. Rev. B* **54**, 9449 (1996).

[27] N. Poccia, T. I. Baturina, F. Coneri, C. G. Molenaar, X. R. Wang, G. Bianconi, A. Brinkman, H. Hilgenkamp, A. A. Golubov, and V. M. Vinokur, *Science* **349**, 1202 (2015).

[28] O. M. Braun, Y. S. Kivshar, *Phys. Rep*. **306**, 1 (1998).

[29] O.M. Braun, A. R. Bishop, J. Roder, *Phys. Rev. Lett.* **79**, 3692 (1997).

[30] S. Avci et al. *Appl. Phys. Lett.* **97**, 042511 (2010).

[31] Gutierrez et al., *Phys. Rev. B* **80**, 140514 (R) (2009).

[32] C. Reichardt, C. J. Olson, F. Nori, *Phys Rev. B* **58**, 6534 (1998).

[33] D. McDermot, J. Amelang, C. J. Olson Reichardt, and C. Reichardt, *Phys Rev E*. **88**, 062301 (2013).

[34] T. Bohlein, J. Michael, C. Bechinger, *Nat. Mater*. **11**, 126 (2012).

[35] T. Bohlein, Clemens Bechinger, *Phys. Rev. Lett.* **109**, 058301(2012).

[36] D. B. Haviland, Y. Liu, A. M. Goldman, *Phys. Rev. Lett.* **62**, 2180 (1989).

[37] A. Yazdani et al. *Phys. Rev. Lett.* **74**, 3037 (1995).

[38] M. A. Paalanen, A. F. Hebard, R. R. Ruel, *Phys. Rev. Lett.* **69**, 1604 (1992).

[39] V. F. Gantmakher, M. V. Golubkov, V. T. Dolgopolov, A. Shashkin, G.E. Tsydynzhapov, *JETP* **11**, 473 (2000).

[40] H. M. Jaeger, D. B. Haviland, B. G. Orr, A. M. Goldman, *Phys. Rev. B.* **40**, 182 (1989).

[41] A.B. Harris, *J. Phys. C* **7**, 1671 (1974).

[42] R. B. Griffiths, *Phys. Rev. Lett*. **23**,17 (1969).

[43] J. A. Hoyos, T. Vojta, *Phys. Rev. Lett.* **100**, 240601(2008).

[44] B. M. McCoy, T. T. Wu, *Phys. Rev.* **176**, 631 (1968).

[45] C. Pich, A. P. Young, H. Rieger, and N. Kawashima, *Phys. Rev. Lett.* **81**, 5916 (1998).

[46] D. S. Fisher, *Phys. Rev. B* **51**, 6411 (1995).

[47] Y. Xing et al. *Science* **350**, 542 (2015).

[48] C. P. Scheller et al. *App. Phys. Lett.* **104**, 211106 (2014)

[49] M. Durkin, I. Mondragon-Shem, S. Eley, T. L. Hughes, N. Mason, *Phys. Rev. B* **94**,024510 (2016).

[50] W. Yu, K. H. Lee, and D. Stroud. *Phys. Rev. B* **47**, 5906 (1993).

[51] V. I. Marconi and D. Domìnguez, *Phys. Rev. B* **63**, 174509 (2001).

[52] C. J. Olson, C. Reichhardt, and F. Nori, *Phys. Rev. Lett.* **81**, 3757 (1998).

[53] T. Giamarchi and P. Le Doussal, *Phys. Rev. Lett.* **76**, 3408 (1996).

[54] C. J. Lobb, D W. Abraham, M. Tinkham, *Phys. Rev. B* **27**,150 (1983).

[55] V. Ambegoakar and B. I. Halperin, *Phys. Rev. Lett.* **22**, 1364 (1969).

[56] T. S. Tighe, A. T. Johnson, M. Tinkham, *Phys. Rev. B* **44**, 10286 (1991).

[57] H. S. J. van der Zant, F. C. Fritschy, T. P. Orlando, J. E. Mooij *Phys. Rev. Lett.* **66**, 2531 (1991).

[58] J. Bardeen, M. J. Stephen, *Phys. Rev.* **140**, A1197 (1965).

[59] Y. Paltiel, Y. Myasoedov, E. Zeldov, G. Jung, M. L. Rappaport, D. E. Feldman, M. J. Higgins, and S. Bhattacharya, *Phys. Rev. B* 66, 060503 (2002).

[60] M. C. Marchetti, A. A. Middleton, and T. Prellberg, *Phys. Rev. Lett.* **85**, 1104 (2000).

[61] A. Altland and B. Simons, *Condensed Matter Field Theory.* (Cambridge University Press, Cambridge. 2010).

[62] G. Blatter, M. V. Feigel'man, V. B. Geshkenbein, A. I. Larkin, and V. M. Vinokur. *Rev. Mod. Phys.* **66**, 1125 (1994).

[63] V. B. Geshkenbein, L. B. Ioffe, and A. J. Millis, *Phys. Rev. Lett.* **80**, 5778 (1998).

[64] S. Lemerle, J. Ferré, C. Chappert, V. Mathet, T. Giamarchi, and P. Le Doussal, *Phys. Rev. Lett.* **80**, 849 (1998).

[65] G. F. Mancini, T. Latychevskaia, F. Pennachio, J. Reguera, F. Stellacci, F. Carbone, *Nano Lett.* **16**, 2705 (2016).

[66] T. Klein, I. Joumard, S. Blachard, J. Marcus, R. Cubitt, T. Giamarchi, P. Le Dousal, *Nature*, **413**,494 (2001)

[67] W. H. Kleiner, L. M. Roth, and S. H. Autler, *Phys Rev.* **133**, A1226 (1964).

[68] M. Marziali Bermúdez, M. R. Eskildsen, M. Bartkowiak, G. Nagy, V. Bekeris, and G. Pasquini, *Phys. Rev. Lett.* **115**, 067001 (2015).

[69] I.K. Dimitrov, N. D. Daniilids, C. Elbaum, J. W. Lynn, X. S. Ling, *Phys. Rev. Lett.* **99**, 047001 (2007).

[70] Y.J. Rosen, A. Sharoni, I. K. Schuller, *Phys. Rev. B* **82**, 014509 (2010).

[71] S. Goldberg et al. *Phys. Rev. B* **79**, 064523 (2009).

[72] D. Ray, C. Reichardt, C. J. Reichardt, *Phys. Rev.* B **90**, 094502 (2014).

[73] S. Guénon, Y. J. Rosen, A. C. Basaran, I. K. Schuller, *Appl. Phys. Lett.* **102**, 252602(2013).

[74] S. Eley, S. Gopalakrishnan, P. M. Goldbart and N. Mason, *Nat. Phys.* **8**, 59 (2012).

[75] M. Durkin, S. Gopalakrishnan, R. Garrido-Menacho, J.-M. Zuo, N. Mason, (2016) "Rare Region onset of superconductivity in granular systems", arXiv:1607.06842

[76] V. Ambegoakar, A. Baratoff, *Phys. Rev. Lett*. **10**, 486 (1963).

[77] S. Bose, P. Raychaudhuri, R. Banerjee, P. Vasa, P. Ayyub, *Phys. Rev. Lett.* **95**, 147003 (2005).

[78] The TEM images were taken by Ji-Hwan Kwon of Prof. Zuo's group.

[79] N. Mason, A. Kapitulnik, *Phys. Rev. Lett.* **82,** 5341 (1999).

[80] S. Bose, R. Banerjee, A. Genc, P. Rachaudhuri, H. L. Fraser, P. Ayyub,. *J. Phys: Cond. Mat.* 18, 4553 (2006).

[81] R.C. Ralph, C. T. Black, M. Tinkham, *Phys. Rev*. **74**, 3241 (1995).

[82] W.H. Li, C. C. Yang, F. C. Tsao, K. C. Lee, *Phys. Rev. B* **68**, 184507(2003).

[83] B. Spivak, P. Oreto, S. A. Kivelson, *Phys. Rev. B* **77**, 214523 (2008).

[84] P. Dubos, H. Courtois, B. Pannetier, F. K. Wilhelm, A. D. Zaikin, G. Schön, *Phys. Rev. B* **63**, 064502 (2000).

[85] G. Lindgren, H. Rootzén, *Scand. J. Statist.* **14**, 241-279 (1987).

[86] The Extreme Value Distribution, http://www.math.uah.edu/stat/special/ExtremeValue.html, accessed on 5/12/2016.

[87] D. Kowal, Z. Ovadyahu, *Sol. St. Comm.* **90**, 783-786 (1994).

[88] A. N. Pasupathy, A. Pushp, K. K. Gomes, C. V. Parker, J. Wen, Z. Xu, G. Gu, S. Ono, Y. Ando, and A. Yazdani, *Science* **320**, 196-201 (2008).

[89] K. K. Gomes, A. N. Pasupathy, A. Pushp, S. Ono, Y. Ando, A. Yazdani, *Nature* **447**, 569-572 (2007).

[90] B. M. Kessler, C. O. Girit, A. Zettl, V. Bouchiat, *Phys. Rev. Lett.* **104**, 047001 (2010).

[91] A. Allain, Z. Han, V. Bouchiat, *Nat. Mat*, **11**, 590 (2012).

[92] C. J. Richardson et al. *Phys. Rev. B* **91**, 245418 (2015).

[93] Z. Han et al. *Nat. Phys*. **10**, 380 (2014).

[94] K. S. Novoselov et al. *Proc. Natl Acad. Sci. USA* **102**, 19451 (2005).

[95] P. Rickhaus, M. Weiss, L. Marot, C. Schönenberger. *Nano Lett.* **12**, 1942 (2012).

[96] J. Martin et al. *Nat. Phys.* **4**, 144 (2007).

[97] S. Cho, M. S. Fuhrer, *Phys. Rev. B* **77**, 081402(R) (2008).

[98] X. Du, I. Skachko, A. Barker, E. Y. Andrei, *Nat. Nano* **3**, 491(2008).

[99] K. I. Bolotin, F. Ghahari, M. D. Shulman, H. L. Stormer, P. Kim, *Nature* **462**, 196 (2009).

[100] C. R. Dean et al. Nat. Phys. **7**, 693 (2011).

[101] V. E. Calado, *Nat. Nano* **10**, 761 (2015).

[102] F. Amet et al. Science **352**, 966, (2016).

[103] N. H. Lidner, E. Berg, G. Refael, A. Stern, *Phys. Rev. X* **2**, 041002 (2012).

[104] A.Miller and E. Abrahams,. *Phys. Rev. Lett.* **120**, 745 (1960).

[105] V. Ambegaokar, B. I. Halperin, and J. S. Langer, *Phys. Rev. B* **4**, 2612 (1971).

[106] D. Stauffer, *Phys. Rep.* **54C**, 1, (1979).

[107] Bernasconi, *Phys. Rev. B* **18**, 2185 (1978).

[108] O. Entin-Wohlman, A. Kapitulnik, Y. Shapira, *Phys. Rev. B* **24**, 6464 (1981).